



UNIVERSITY OF GENOA

DEPARTMENT OF ELECTRICAL, ELECTRONIC AND
TELECOMMUNICATION ENGINEERING AND NAVAL ARCHITECTURE
(DITEN)

PH.D. IN SCIENCE AND TECHNOLOGY FOR ELECTRONIC AND
TELECOMMUNICATION ENGINEERING

**Electromagnetic modeling and simulations
of interest for low-level laser therapies or
for problems involving moving objects**

Ph.D. Thesis

Mario Rene Clemente Vargas

November 2022

TUTOR: Prof. Mirco Raffetto

Coordinator of the Ph.D. Course: Prof. Maurizio Valle

Abstract

This work presents results on the computed electromagnetic field within isolated mitochondria when exposed to near-infrared illuminations concerning photobiomodulation experiments. The accuracy of the electromagnetic models implemented for dosimetry is important. The mechanism of interaction of light with these organelles is still unclear, so it is important to improve our knowledge with reliable simulations and experiments. To obtain such results, we present several models. Although they refer to a well-defined experimental setup, the different models must consider the different possible arrangements of the mitochondria and the differences in their dimensions and constitutive parameters. Different wavelengths and polarizations are considered too. The effects of all the parameters on the electromagnetic field inside the mitochondria and the internal morphology are studied.

Computational techniques are also exploited to find reliable approximations of the solutions of problems involving moving objects. The effect of the motion of objects on the electromagnetic field is studied as well; for this type of problem, it is necessary to understand that the constitutive relations are modified because the movement makes any material to appear as a bianisotropic medium. In particular, the rotation movement of symmetrical bodies is studied, the electromagnetic field is calculated and an inversion algorithm for the estimate of the rotation speed is proposed.

Acknowledgments

I would like to express my sincere gratitude to my advisor Prof. Mirco Raffetto for the continuous support of my Ph.D. study and research activities. His guidance helped me in developing the necessary skills for conducting the research. His patience, enthusiasm, warmth and immense knowledge will always inspire me to improve my professional skills.

Besides my advisor, I would like to thank all the members of Applied Electromagnetics Laboratory. I thank Prof. Matteo Pastorino, Prof. Andrea Randazzo, Prof. Bruno Bianco and Prof. Gian Luigi Gragnani for their support. I express my sincere gratitude to the other researchers in the laboratory, Alessandro Fedeli, Emanuele Tavanti, Praveen Kalarickel Ramakrishnan, Chiara Dachena e Valentina Schenone, who were always helpful and friendly.

I would like to thank to Dr. Silvia Ravera and Dr. Andrea Amaroli. Their scientific experience was crucial to carry out experiments of Photobiomodulations in their laboratory.

I thank my family, my mother Vicentina Yrene Vargas, my father Mario Clemente, my stepfather Giorgio Milanesi and my sister Gladys. I would like to thank my brothers Rolando and Roger who died, and always have them present in my heart. I would thank to all members of the Bennicelli family who supported me in difficult times and in particular Mr. Augusto, Mr. Filippo, Mr. Andrea, Mr. Alessandro, Mrs. Franca and Mrs. Florencia.

INDEX

Chapter 1 Introduction.....	6
Chapter 2 State of the art for Low-Level Laser Therapy.....	8
2.1 Evolution of Low-Level Laser Therapy.....	8
2.2 Electromagnetic models for solving light scattering in biological cells.....	15
2.3 Mechanism of interaction between light and biological organelles.....	17
2.4 Influence of irradiation parameters and biological organelles involved in Low-Level Laser Therapy experiments.....	18
Chapter 3 Study and implementation of new electromagnetic scattering algorithms applied to Low-Level Laser Therapy.....	21
3.1 Algorithm implementation for the first simplified experimental model.....	23
3.2 Implementation of the electromagnetic model using finite element method with homogeneous mitochondria model.....	33
3.3 Stability of the three-dimensional electromagnetic model.....	38
3.4 Study of polarization for three-dimensional electromagnetic model.....	43
Chapter 4 Electromagnetic implementation and simulation of complex and more realistic structures in the context of Low-Level Laser Therapy.....	51
4.1 Implementation of complex electromagnetic model involving mitochondria models.....	51
4.1.1 Lamellar mitochondria model.....	52
4.1.2 Tubular mitochondria model.....	53
4.1.3 Simplified lamellar mitochondria model.....	54
4.2 Numerical results of energy density, power density, polarization and scattering electric field.....	56
Chapter 5 Experimental measurement: Study in vitro.....	70
5.1 Material and methods.....	70

5.2 Evaluation of Mitochondrial ATP Synthesis.....	76
Chapter 6 Electromagnetic simulations of problems involving moving objects.....	78
6.1 State-of-the-art related to electromagnetic scattering for moving object.....	79
6.2 Inversion procedure for rotating media.....	80
6.3 Numerical results.....	82
6.3.1 Comparison of the two-step procedure with the general algorithm...	84
6.3.2 Efficiency of two-step procedure.....	87
6.3.3 Reconstruction of velocity of rotation.....	90
6.3.4. Effect of dielectric media.....	92
6.3.5 Recovery of rotating speed for torus model.....	92
Conclusions.....	99
References.....	102

Chapter 1 Introduction

Low-Level Laser Therapy (LLLT), also known as Photobiomodulation Therapy (PBMT), is becoming an increasingly mainstream wound repair modality, especially in clinical rehabilitation and veterinarian medicine. There is a large number of references, reporting the effects of PBMT. This type of treatment consists in irradiating the biological target of interest in a specific “therapeutic windows band,” which is in the red or near-infrared (NIR) band between 600-1100 nm with a power of 1 – 1000 mW [5], [6]. These therapeutic procedures are non-invasive, even though light can go through tissues to reach the biological target. The experiments showed that the most important reaction occurred within the mitochondria; this was verified when the experiments involved mitochondria in vitro.

Chapter 2 presents the state of the art for Low-Level Laser Therapy (LLLT) in the last years. Many scientists and engineers have studied this non-invasive therapeutic procedure, and the mechanism of interaction between light and biological organelles still needs to be clarified. Many experiments were performed under unclear conditions, and more information is needed to replicate them. LLLT presents positive results for several experiments for "in vitro" and "in vivo" systems, however, for other experiments present null or negative results are obtained.

In Chapter 3 methods are proposed to evaluate the electromagnetic field that stimulates the mitochondria for in vitro photobiomodulation experiments. In this first approach, the one-dimensional model is proposed, in which the problem can be simplified and approximate to multilayer structure and the mitochondria sample represents a homogeneous layer. For this problem it is possible to calculate the electromagnetic field by solving a multiplanar structure. The following approach proposes to implement a three-dimensional model in a limited domain of interest, where mitochondria are considered ellipsoidal with homogeneous media. The effect of polarization is analyzed; the energy density and power density of mitochondria are calculated for the different cases. Both the total electric field and the scattering field are presented.

The internal structure of the mitochondria presents a morphology consisting of an outer membrane that encloses an inner membrane which presents a complex pattern of invaginations called cristae. Chapter 4 presents the study of the internal structure of mitochondria, which have a lamellar or tubular shape. The three-dimensional models of inhomogeneous mitochondria are proposed, they are classified as lamellar, tubular, and simplified lamellar model. The energy density and power density for these inhomogeneous models are calculated. The effect of polarization is studied, and the scattering field is calculated for the different models proposed.

Chapter 5 present a measurement campaign, which is carried out using the proposed experimental setup, employing a laser at 810 nm and an incubation chamber made of glass with the dimensions proposed in this work. The solution containing a sample of mitochondria with PBS saline solution of 300 microliters in a proportion of 1 to 64 and different powers and irradiation times are applied. This experiment shows evidence that energy irradiation and exposure time play an important role in ATP production.

Chapter 6 studies the electromagnetic inverse scattering problem for rotating axisymmetric objects. This study proposes a more sophisticated algorithm to obtain the first estimates to the problems of interest. In the first step, the forward solver is employed, assuming zero rotating speed, and the geometrical and dielectric parameters are reconstructed minimizing the cost function. The values from the first step are used to determine the rotating speed in the second step. Numerical results for this type of inverse problem are provided for the first-time considering test cases with rotating homogeneous spheres and torus. The two-step algorithm is compared with the general inversion algorithm, based on global optimization, simultaneously considering all unknown variables. It is verified that the procedure algorithm is an improvement in comparison to the general inversion procedure for all speeds of practical interest. The results are analyzed for noisy data in the near-field and far-field.

Chapter 2 State of the art for Low-Level Laser Therapy

2.1 Evolution of Low-Level Laser Therapy

The Low-Level Laser Therapy (LLLT), also known as Photobiomodulation (PBM) Therapy, has been studied and developed as a non-invasive therapeutic procedure. This therapy is well known for beneficial treatment in human patients and animals, for example in terms of inflammatory reduction or promotion healing in wounds [1],[2]. Many researchers have studied for decades this therapy and some results are reported in [3]. This therapy consists in irradiating the biological target of interest with a specific low power and a wavelength in the Infrared or near-Infrared band, where the effects have been positive.

The first experiment of irradiation using a laser with low power intensity in biological tissues happened in 1967 at Semmelweis Medical University (Hungary) made by the Dr. Endre Mester [4]. This experiment consisted of shaving the back of a mice and then implanting a tumor through an incision in the skin. Dr. Mester in this experiment has applied light using a ruby laser at 694 nm to repeat one of the experiments described in [5]. Dr. McGruff used the ruby laser to cure malignant tumors in rats and tested it in human patients using a laser in ablation mode with high energy (between 50 - 2500 J). In this experiment, Mester's laser was used with a part of the power applied by Dr. McGuff's laser. Hence, Mester failed to cure tumors in mice, but did observe a faster rate of hair growth in the treated mice confronted to the mice controls [4], calling this effect "laser biostimulation". After that, Dr. Mester used a He-Ne laser at 644 nm to stimulate wound healing in animals, as well as in clinical tests [6]. This therapeutic method is in continuous evolution and LLLT is going to be a multidisciplinary field of research in which many scientists and engineers are involved for improvement and development of new devices for clinical applications.

The application of LLLT for different treatments is still unclear because there is disagreement about the LLLT parameters (laser or LED, irradiance, dose, exposure time, etc.), and dose for the specific biological targets. To obtain reliable results it is important to establish a corresponding treatment approach taking into account the types of irradiated tissues and the target depth [1]. In [7] the type of source and wavelength for PBM therapy

are reviewed; the use of “in vitro” and “in vivo” systems are discussed. Different wavelengths lead to variable results, consequently it is important to determine the most effective wavelength that promotes wound healing.

A preliminary experimental study of the effect of laser irradiation in rats and mice for promoting wound healing is reported in [8]. This work highlights the importance of defining the parameters used for laser therapy as continuous wave or pulse radiation, wavelength, power, power density, time of irradiation, spot size or area of irradiation and energy density. Zein in [3] presents a study about the importance of implementing parameters and protocols for clinical applications; the criteria are ambiguous, for example, recommends using power density less than 100 mW cm^{-2} and energy density between 4 to 10 J cm^{-2} for level target tissue and for tissue surface as much as 50 J cm^{-2} . The effectiveness of parameters LLLT for in vitro or in vivo studies is applied for different tissues, classified as high number of mitochondria and low number of mitochondria, which corresponds to a specific dose of light. The lack of information about light parameters (spot diameter, surface of target, power density, and distribution of energy) cause significant contradictions.

The term “Biphasic dose response” describes a situation in which an optimum value of the “dose” of LLLT exist, and the energy density most often defines it. The precise dose delivered to the tissue is critical; in terms of the Arndt-Schultz curve which is indicated in Figure 2.1[134]–[136], the LLLT therapy can activate or inhibit biological responses producing significant effects on living biological systems [9]. The medical applications of infrared radiation are studied in [10], where the infrared therapy is applied in many fields, like therapeutic management of sports activities using infrared emitting materials for clothing. Far Infra-Red (FIR) saunas and Waon Therapy are used for medical treatment. Infrared Neural Stimulation (INS) is a therapy applied for wound healing, tissue regeneration, photoaging, and photo rejuvenation for dermatology.

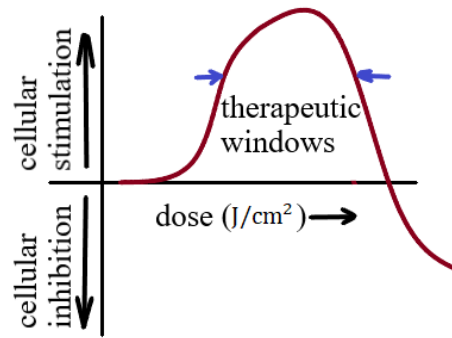


Figure 2.1. The Arndt-Shultz curve

The importance of understanding the spectrum absorption of the most important chromophore involved in the mechanism of photobiomodulation is under discussion. Dr. Tiina Karu, researcher expert who worked for many years in the field of photobiomodulation, supported by the experimental results. She maintains that the action spectrum reflects one of the intermediate forms of the cytochrome c oxidase complex. It is important to indicate that other molecules, beyond cytochrome c oxidase (COX), influence the ATP production, for example Nitric Oxide (NO) [5]. Inside mitochondria exist others chromophores which absorb radiation light and transform into chemical energy, the most important chromophore involved in ATP production is the COX, but for other authors, there are other chromophores like Nitric Oxide (NO) that inhibit the response [11]–[15]. In the last years, Low-Level Laser Therapy is under discussion because limited predictive capability exists, leading to prediction in disagreement with experimental results. This new model explains new results obtained when infrared or near-infrared light cause ATP upregulation and cell proliferation via the interaction of photons with intracellular IWL (Interfacial Water Layer) [16], [17].

In recent research, the molecular mechanism of PBM continues to puzzle the investigation. The experiment using cells was cultured using DMEM medium supplemented with fetal bovine serum (FBS), 1 mM sodium pyruvate sodium, and 50 µg/ml uridine at 37 °c in 5% CO2 atmosphere. The light source used was the “Photon Laser” (DMC Equipamentos Ltda, Brazil) at 660nm with a power of 30 mW. The measurement obtained presents an enhanced metabolism but no changes of COX (or CCO); these observations suggest that PBM may alter cellular metabolism through one or more molecular targets, even if it does

not depend on cytochrome c oxidase. It cannot be excluded that COX can participate in the metabolic alteration triggered by PBM in certain tissues or conditions. [18].

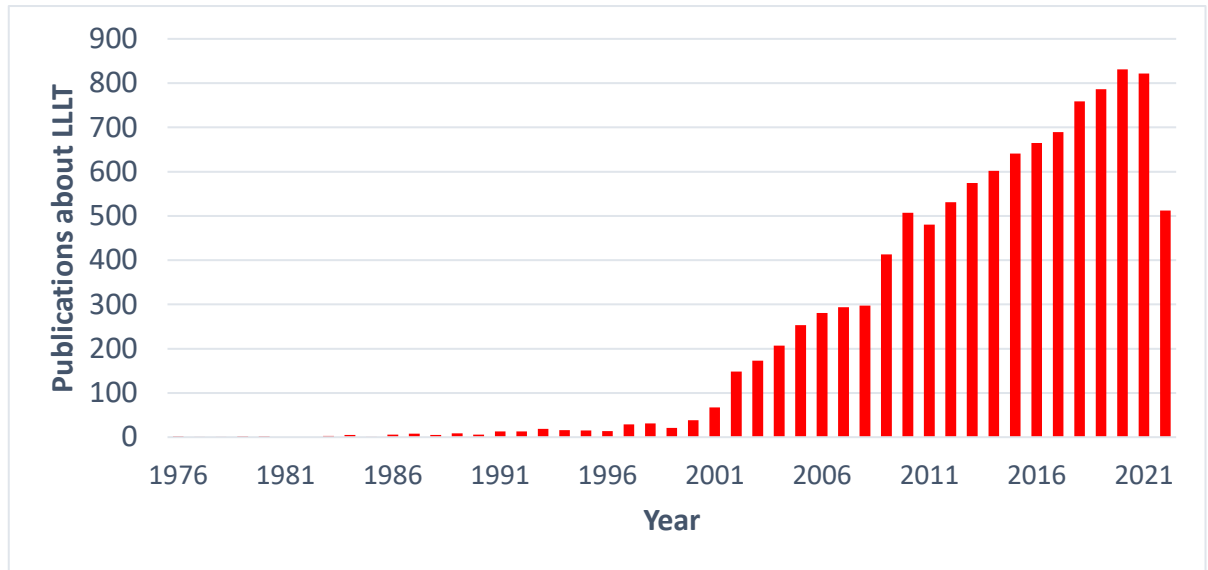


Figure 2.2 Number of LLLT publications per year according to a search for LLLT (source National Library of medicine <https://www.ncbi.nlm.nih.gov> in October of 2022).

At the moment, there are over 10000 scientific papers, conference papers, and journals related to this therapeutic treatment were published in this field of laser therapy between 1975 to 2022, with an increase in this topic in the last twenty years (Figure 2.2).

Several researchers present their results obtaining interesting outcomes for many applications. In Table 2.1 the parameters used for several therapeutic cases are reported.

λ_0 [nm]	Power density [mWcm ⁻²]	Energy density [Jcm ⁻²]	Irradiation time [s]	Spot Area [cm ²]	Emission mode	In vivo/in vitro	Biological target/disease
1064	0 to 1600	60	-	-	CW	In vivo	Arthritis[19]
808	700	84	120	-	CW	In vivo	Major Depressive Disorder[20]
810	4750	4, 8	180, 300	-	PW	In vivo	Apoptosis[21]
633	12.25	8	300	-	CW	In vivo	Traumatic Brain Injury[22]
870	1	20	720	-	-	-	-
658	79.6	1,4,8	-	-	CW	In vitro	DNA repair[23]
660	3	0.5	-	-	-	-	Diabetes[24]

830	4	4					
904	305.6	22.9	660	0.1309	PW	In vivo	Osteoarthritis OA[25]
890	1.08	0.972	900	1	PW	In vivo	Osteoporosis[26]
810	-	3.4	120	1.76	PW	In vivo	Temporomandibular joint disorder[27]
808	50	4	-	12.25	CW	In vitro	Osteoblastic and osteoclastic[28]
780	1.75	4	1.5	0.04	-	In vitro	Macrophage[29]
660	0.375	7.5	20				
810	20	3	150	25	CW	In vitro	Neural cells[30]
810	25	3	120	25	CW	In vitro	Neural cells[31]
810	25	0.03,0.3,3 and 10	300	-	CW	In vitro	Mouse cortical neuron[32]
808	50	0.05	600	-	-	In vitro	Human neural cells[33]
660	7.5	3	20	0.04	CW	In vitro	Macrophage[34]
780	3	20	3				
808	44.7	1	22.4	3.8	-	In vitro	Monocyte[35]
660	0.8	1.2	1250,2500	7.5			
850	28	2.5	90	45	CW	In vitro	Myotube C2C12[36]
630	28	2.5	90	45			
808	100, 1000	3, 64	64	1	CW	In vitro	Paramecium[37]
420	16	3	188	4	CW	In vitro	Adipose stem cells[38]
540	16	3	188				
628	11.46	0.88,2.44	76	9.6	CW	In vitro	Fibroblast[39]
830	8.4	1.5, 3	360	10	-	In vitro	Fibroblast[40]
915	150	7.2,14.4	48, 96	1.91	PW	In vitro	Fibroblast[41]
930	1580	7.8,15,39	5,10,25	0.63	CW	In	Preosteoblast[42]

						vitro	
808	80	1.2	900	-	CW	In vitro	Osteoblast[43]
980	26,73, 97	3.1,8.8, 11.6	-	-	-	In vitro	Fibroblast[44]
940	300	18	60	-	CW	In vitro	Cementoblast[45]
810	16	3	188	4	CW	In vitro	Adipose stem cells[46]
980	16	0.3	18.8	4	CW	In vitro	Adipose stem cells[47]
808	1780	142.4	80	0.028	-	In vivo	Arthritis[48]
810	5	0.3	60	1.1	-	In vivo	Heart[49]
803	6	1.08	180	-	-	In vivo	Myocardium tissue[50]
810	5,5,50	3,30,30	600,600, 6000	0.2025	-	In vivo	Arthritis[51]
810	560	1.2	-	0.07	PW	In vivo	Brain[21]
810	15	36	240	-	PW	In vivo	Brain[52]
660	1.5	36	240				
1064	250	60	240	13.6	PW	In vivo	Brain[53]
1064	250	60	240	13.6	CW	In vivo	Attention bias modification ABM[54]
810	50	36	720	0.78	PW	In vivo	Traumatic Brain Injury[55]
810	150	36	240	-	PW	In vivo	Traumatic Brain Injury[56]
660	6890	206.89	30	0.02	CW	In vivo	Femoral quadriceps[57]
850	6890		30	0.02			
635	6.37	0.96	150	1	CW	In vivo	Preconditioning myocardium[58]
655	31.25	0.5,1	32,80	0.08	-	In vivo	Muscle[59]
830	125	20,50	-	0.36	-	In vivo	Wound healing[60]
670	8	5	625	-	CW	In vivo	Ulcer[61]

632	4	2		1.75		In vivo	Wound healing[62]
670	15	5	213	-	-	In vivo	Wound tensile strength[63]
670	130	1, 5	-	1.534	-	In vivo	Wound healing[64]
790	3500	140	40	0.028	CW	In vivo	Bone[65]
830	3500	140	40	0.028			
660	3.5	0 to 20	360 to 1440	-	-	In vitro	Wound healing[66]
660	50	30	600	0.01	-	In vitro	Vascular regeneration[67]

Table 2.1. LLLT parameters with effective responses.

It is important to consider also the results obtained from other researchers which achieved ineffective or null outcomes; in Table 2.2 the parameter used with the corresponding biological target/disease are reported.

λ_0 [nm]	Power density [mWcm ⁻²]	Energy density [Jcm ⁻²]	Irradiation time [s]	Spot Area [cm ²]	Emission mode	In vivo/in vitro	Biological target/disease
810	25	30	600	-	CW	In vitro	Mouse cortical neurons[32]
660	0.8	2, 3	2500	7.5	-	In vitro	Monocyte[35]
808	100, 1000	64, 3	64	1	CW	In vitro	Paramecium[37]
915	150	20.56	144	-	PW	In vitro	Osteoblast[41]
930	1580	1.57, 78.7	1, 50	0.63	CW	In vitro	Preosteoblast[42]
980	49, 120	5.9, 14.4	120, 120	-	-	In vivo	Fibroblast[44]
810	2.5, 25	0.3, 0.3	-	1.1		In vivo	Heart[39]
660 810	4750	4	-	-	PW	In vivo	Brain[68]
980	15	36	-	-	-	In vivo	Brain[52]
808	3570	142.4	80	0.028	-	In vivo	Arthritis[48]
655	31.25	2.5	160	0.08	-	In vivo	Muscle[59]
670	0.7, 2, 40	5, 5, 5	-	-	-	In vivo	Wound healing[61]
670	15	5	-	-	-	In vivo	Wound healing[63]

632	130	9	-	1.75	--	In vivo	Wound healing[62]
670	130	9, 19	-	1.534	-	In vivo	Wound healing[64]
636	1	5	-	-	-	In vivo	Wound healing[69]
670	-	4.5	180	-	CW	In vivo	Retinal degeneration[70]
660	1000	2		0.04	CW	In vivo	Ulcers[71]
532 635	-	-	240	-	CW/PW	In vivo	Hearing[72]
830	-	120	-	0.36	CW	In vivo	Cochlera disfunction[73]
808	1000	60	60	1	CW	In vivo	Facial Paralysis[74]

Table 2.2. LLLT parameters with an ineffective or null responses.

In conclusion, the preliminary studies present important results for the treatment of LLLT in “in vivo” or “in vitro” studies. However, many scientific articles do not present all the information to replicate the same experiments regarding radiation doses and/or biological targets. Therefore, it is important to consider a general protocol. Another important consideration is the instruments’ reliability, for example the light source (laser or led). Before to start the experiments, it is necessary to verify the laser power with a calibrated power meter, in addition, the use of laser will degrate over time and it may irradiate with wrong power set.

2.2 Electromagnetic models for solving light scattering in biological cells

Electromagnetic models for solving light scattering in biological cells and organelles have been studied for many years. The interest of the research is the effect of scattering fields produced by the scattered organic objects. Since our interest is in the local field inside the scatterer, one of the essential points is that many works neglect the absorption coefficient while representing the refractive index of the cells and organelles. Also, the macroscopic medium in which the scatterer is present is considered homogeneous in most cases. Some works are based on approximations that are not suitable for getting localized fields. For example, in [75], a spectral method is defined and used to get approximate results for the scattering pattern; the resulting algorithm gives accurate results only for small scattering angles for the far-field. In [76], the authors calculate the radiation pressure exerted by laser

beams on red blood cell-like particles and is based on two-dimensional MOM. A two-dimensional Muller boundary integral equation MBIE method was used for computing scattering from single biological cell models [77]. Scattering from red blood cells using circular and elliptic geometries with the cell membranes is computed. In the research [78], the authors are interested in the modeling of photoreceptor cells in the eye at very low frequencies between 50 Hz to 1 GHz.

In [79], the model is implemented on FEM and was used to compute the cell's scattering, consisting of the cytosol and the membrane of red blood cells RBC. Using $\lambda_0 = 1.06 \mu\text{m}$, the volume is approximately $555 \mu\text{m}^3$, meshed with a size in the range from $\lambda_0/10$ to $\lambda_0/4$ and the solution was computed using the RF model of COMSOL Multiphysics. In [80], the light scattered from a cell using a three-dimensional FDTD grid for an incident field in free space with $\lambda_0 = 900 \text{ nm}$ is studied. A spherical cell with a diameter between $11 - 12 \mu\text{m}$ and having an internal spherical structure like a nucleus and mitochondria is considered with a grid spacing of $\lambda_0/20$. The final results are presented in terms of the far field scattering patterns; the method involved calculating the near fields, which are transformed into the far-field pattern by using homogeneous Green's function on the equivalent sources computed on a surface inside the computation domain.

Another interesting work in [81] in which the light scattered from red blood cells is simulated using various methods, including FDTD. The approximate method used in this paper exploits the "superposition" method and "Rytov approximation" and was very crude to be considered for obtaining any near-field solution. The FDTD and DDA (Discrete Dipole Approximation) are two methods which are full-wave methods, and these were used to obtain the scattered field pattern far from the cells. A Cell volume of $94 \mu\text{m}^3$ was simulated in less than an hour and using less than 500 MHz of RAM. The FDTD method used in [82] presents a model for simulating of biological cells with different shapes and positions. In [83] and [84] two-dimensional method FDTD for cellular imaging is used. The paper [85] focuses on the post-processing of data from FDTD for nanobioimaging.

In conclusion, we confirm that previous studies involving electromagnetic fields in biological cells only are concerned with scattering fields in far-field. Some techniques are rigorous to obtain the near-field solution but do not report the local fields inside the cells

and organelles. Furthermore, the cells are considered to have a homogeneous external medium, and a multilayer macroscopic configuration is not studied.

2.3 Mechanism of interaction between light and biological organelles

The study of this topic is under research in the field of biomedical applications. There are several explanations or theories, many of which involve light absorption. The main concept behind the explanations of this treatment is that a photobiological reaction occurs within the mitochondria. Specific molecules inside the mitochondria convert the absorbed light into chemical energy.

Dr. Tiina Karu in their works indicates that the most important chromophore involved in Low-Level Laser Therapy is COX, which is a molecule present in the respiration chain inside mitochondria. Dr. Karu in [86] proposes that laser light irradiation of isolated mitochondria involves the activation of ROS (Reactive Oxygen Species) by increasing COX levels. In [87], it is suggested that the primary chromophore responsible for improving the beneficial effects of PBM is located within the mitochondria, by influencing their pathophysiological function and by stimulating their components. In [88], it is reported that the LLLT can increase the intracellular generation of ROS at a particular wavelength, activating specific biochemical reactions and altering the whole cellular metabolism.

Experimental measurements have shown that significant reactions are produced inside the mitochondria when a light source of coherent radiation in the near-infrared spectra is applied [86]–[88]. The stimulation of ATP synthesis by isolated mitochondria increased at 415, 602, 632.8 and 725 nm; at 477 and 554 nm it proved ineffective, while at 760 nm, the ATP synthesis decreased. At a wavelength of 808 nm, the photobiomodulation effect with a higher-fluence diode laser (64 Jcm^{-2} with power 1 watts and continuous wave) irradiated by a flat-top handpiece exhibits mitochondrial activities, such as oxygen consumption and activation of mitochondrial complexes I, II, III, and IV, as well as the ATP synthesis is verified [12].

The photon energy is absorbed by the mitochondrial chromophores and then transformed into chemical energy; this energy is used to power up the cell. This statement is supported by many researchers who have described the increase of ATP production after laser

therapy [89]–[91]. The dose of LLLT or PBM Therapy for the experiments is under discussion, which means that the irradiation parameters can be adjusted to produce different results for each type of biological target. Finding effective irradiation parameters depends on the conditions and characteristics of the biological target. The irradiation time for laser therapy plays a significant role when it is used for very short or very long times and may cause no effect or negative response, respectively. These characteristics agree with the biphasic dose-response, which is the generalization of the “Arndt Shultz’s law”, a rule used in pharmaceuticals products for the biological effects of drugs [9]. The Arndt Shultz’s law describes that substances that inhibit biological processes at sub-lethal levels might be expected to stimulate at lower levels. This law was later generalized and explained the stimulatory effects caused by a low level of potentially toxic agent called “Hormesis”[92].

In conclusion, the principal organelle within cells responsible for enhanced cellular metabolism when is applied photobiomodulation experiments is the mitochondria. Inside mitochondria there are photomolecules, the most important is COX, which transform irradiated light into chemical energy.

2.4 Influence of irradiation parameters and biological organelles involved in low-level laser therapy experiments

The importance of defining the parameters for obtaining good results in LLLT experiments is still studied because, until now, there is a lack of information in the literature reporting incomplete and unverified irradiation parameters [3], [93]. Several researchers report the most important irradiation parameters related to the light source are:

- Wavelength (λ_0): Is defined as the spatial period of a periodic wave or the distance over which the wave’s shape is repeated. Assuming the wave is sinusoidal and moving at a fixed wave speed; the wavelength is inverse proportional to the wave’s frequency and depends on the medium involved. The values most used for LLLT applications are present in infrared or near-infrared region, most commonly called “therapeutic windows” in the range between 600 to 1100 nm [3], [89].

- Irradiance [Wcm^{-2}]: It is defined as power irradiated over beam area at the surface of physical objects illuminated for biological tissue or cell culture samples. It is also known as “power density” or “fluence rate” [93].
- Energy density or fluence [Jcm^{-2}]: It is defined as the energy delivered per unit area of cells during light stimulation for LLLT. It is also known as “Dose” or “radiant exposure” [3], [93].
- Continuous wave or pulsed wave: The light source could be irradiated using a “continuous wave” mode or “pulsed wave” mode. When is applied a “Continuous Wave” mode (CW), the average power of the light source is constant in time. When “Pulsed Wave” mode (PW) is applied, a modulated pulse is a continuous beam switched on and off. The rate of the switching is expressed in Hertz (Hz) [3], [89], [93].
- Coherence and not Coherence light source: Lasers (Light Amplification by Stimulated Emission of Radiation) are a type of light source which is used in stimulated emission to create a monochromatic and coherent beam of light [3], [89], [94]. Instead, LED (Light Emitting Diodes) are other types of the light sources based on phenomena of electroluminescence made of semiconductor materials and present characteristics of no coherence. In LLLT applications, significant differences exist using a laser or LED.
- Polarization: Light is polarized when the electromagnetic waves oscillate in one orientation (one plane). Some lasers emit polarized light (linear, circular, etc.), and other light sources can be projected through a filter to polarize them. Polarized light may affect superficial birefringent protein structures such as collagen. Several authors have demonstrated effects on wound healing, and burns with broad-spectrum polarized light. However, the polarization is soon lost due to scattering and has not shown to be a significant parameter in LLLT applications [86], [95].
- Irradiation time: Also known as “Exposure duration”, is another important parameter for LLLT applications. It is the duration of exposure to produce beneficial effects when the biological target is irradiated.
- Spot size: It is the surface area illuminated by the light source; it is expressed in cm^2 .

For the parameters involving the biological target, it is important to know the following information:

- Optical properties of biological target: Biological tissues are characterized by optical parameters such as refractive index, absorption coefficient, scattering coefficient, and scattering anisotropy.
- Depth of biological target: The depth, also known as “optimal penetration” of electromagnetic field is also important.
- Geometric parameters of biological target: To study the biological target is necessary to know the shape and the geometric dimensions to be accurately modeled.

The most important irradiation parameters for LLLT are irradiance, fluence and irradiation time. In the future it will be necessary to established a protocol for LLLT with relevant information about the experimental measurements; it would be possible to obtain more reliable results. The knowledge of the optical properties of the biological target and the tissues are very important for implementation of electromagnetic modeling.

Chapter 3 Study and implementation of new electromagnetic scattering algorithms applied to Low-Level Laser Therapy

This chapter presents the implementation of the experimental setup to study the mechanism of interaction between light and biological organelles. This system requires a laser source that irradiates a monochromatic electromagnetic field with a wavelength belonging to infrared or near-infrared spectrum region (600-1100 nm), linearly polarized and positioned on the top of the incubation chamber (Figure 3.1 representing a sample of mitochondria detected by using fluorescence microscopy). The laser illuminates an incubation chamber with a cylindrical shape containing saline solution and a sample of mitochondria hosted at the bottom of it (Figure 3.2)[96]. The dimension of the incubation chamber is on the order of centimeters. In contrast, every mitochondrion organelle has dimensions less than 1 μm . The group of mitochondria would create difficulties in calculating the electromagnetic field due to their complex structure, including the presence of interstices between one mitochondrion and another. To simplify the analysis of the problem, we will consider the presence of one isolated mitochondrion instead of an entire group, which can be approximated with an ellipsoid of a circular section. The presence of the mitochondrial membrane will also be neglected.

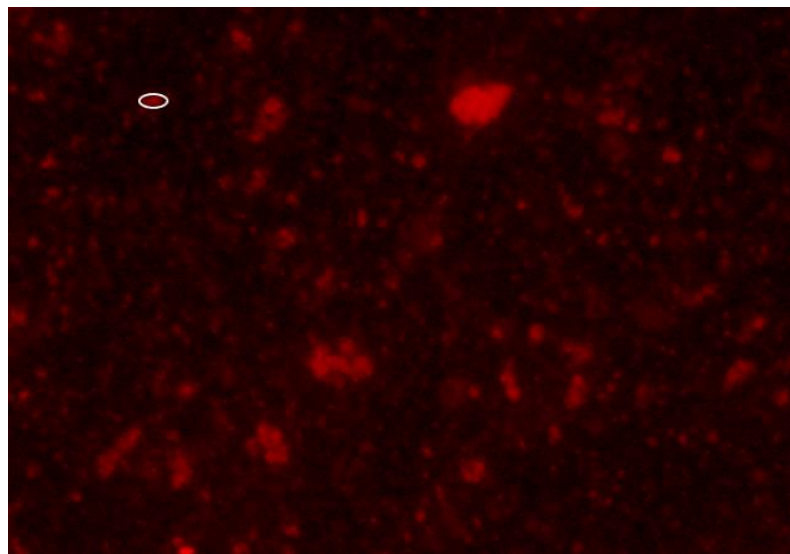


Figure 3.1. Analysis with fluorescence microscopy for detecting sample of mitochondria. The white outline indicates an isolated mitochondrion.

In the incubation chamber, we can find a setup composed of air, a saline solution, and a group of mitochondria at the bottom. The medium below the chamber glass is air and it must be ensured that there are no obstacles under the glass chamber that could cause an outgoing wave outside to be reflected into the camera. The corresponding saline solution shows a very small molarity and is close to the smallest concentration value (refractive index present values between 1.328 to 1.331 for wavelengths between 808 nm to 1064 nm, this is explained in detail in page 33, Table 3.1). This reference shows that the refractive index of various mixed salt solutions shows a negligible difference from that of deionized water or standard salt solutions at different concentrations and wavelengths; for this reason, it is assumed that the refractive index of the solution is the same as that of simple water. In a complex process, mitochondria are isolated from the bovine liver by a standard differential centrifugation technique and are suspended in the solution. After a while, they spread out at the bottom of the incubation chamber because mitochondria have a mass density a little bit higher than that of the surrounding saline solution.

The sample of mitochondria involved in these experiments is expressed in terms of mass of the proteins. Let's consider 50 μg of these proteins and assume an average protein concentration of 0.5 g/ml (in "respiring state")[97]. A mitochondria volume of 10^{-4} ml was obtained, corresponding to a medium thickness of 1 μm distributed over the entire lower surface of 1 cm^2 . Even if the end of the arrangement of the organelles on the floor of 1 cm^2 is not regular for its morphology, we can conclude that it is unlikely to have to deal with groups of mitochondria with a height larger than very few micrometers.

The geometric dimensions of the experimental setup are huge with respect to the wavelength operation; the electromagnetic field inside the incubation chamber will be approximates a plane wave (neglecting the effects present at the borders), polarized along the x or y-axis and propagating along the z-axis. The implemented model's structure is shown in Figure 3.2, where the geometric parameter t_{ss} and t_g are set to 5 mm and 2 mm, respectively.

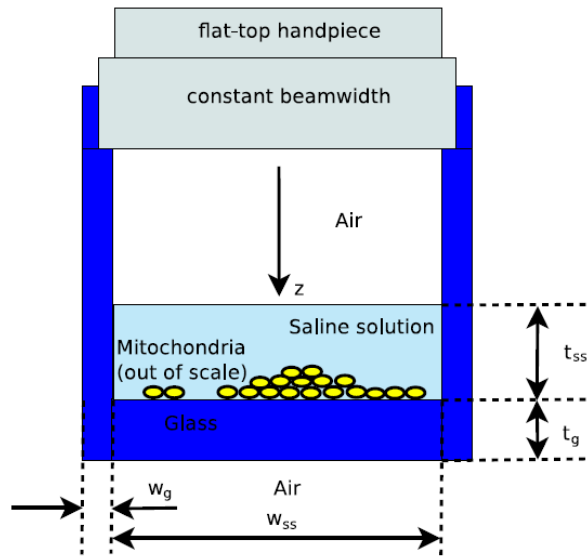


Figure 3.2. Model of the experimental setup. A laser with a flat top handpiece is positioned on the top to generate a monochromatic electromagnetic field linearly polarized which illuminates a sample of mitochondria placed at the bottom of an incubation chamber made of glass [96].

3.1 Algorithm implementation for the first simplified experimental model

The experimental model in question would not present difficulties to solve without the mitochondria. In that situation, the electromagnetic field presents two layers (saline solution and glass). The experimental model is simplified exclusively to solve plane waves in a multilayer structure. Even in the air in contact with the saline solution, there would be two plane waves (progressive and regressive waves), while in the air under the glass layer, there would be a single progressive plane wave on the base of the adopted model (Figure 3.3). The scattering electromagnetic field produced by the mitochondrion cannot be calculated analytically; in this case, we solved using commercial computational electromagnetic software. To correctly set the problem in the numerical software, it is necessary to carry out preliminary evaluations on the execution times of the simulations so that they have reasonable values. The three-dimensional geometry of the entire experimental setup has some dimensions equal to several thousand times the wavelength of the electromagnetic radiation used; this would imply an impractical simulation time. Therefore, it was decided to run the simulations in one limited domain, as is usually done

in multiscale problems. This domain consists of a cube of sides 10 μm , centered in the position where the mitochondrion is present (Figure 3.3).

The presence of the mitochondria complicates the situation, and the total electric field \mathbf{E}_{tot} is no longer constituted by the incident field \mathbf{E}_{inc} , but by the sum of the latter and scattering electric field (\mathbf{E}_{scat}).

$$\mathbf{E}_{\text{tot}} = \mathbf{E}_{\text{inc}} + \mathbf{E}_{\text{scat}} \quad (1)$$

In this case, a current density (called equivalent or secondary current density) is formed on the surface on scatterer. It is proportional to the total electric field, and it is responsible for irradiating the scattered field. The approximate approach we chose is to consider the mitochondrion as a weak scatterer. In the presence of a weak scatterer, it is assumed that the equivalent current density is proportional to the incident electric field.

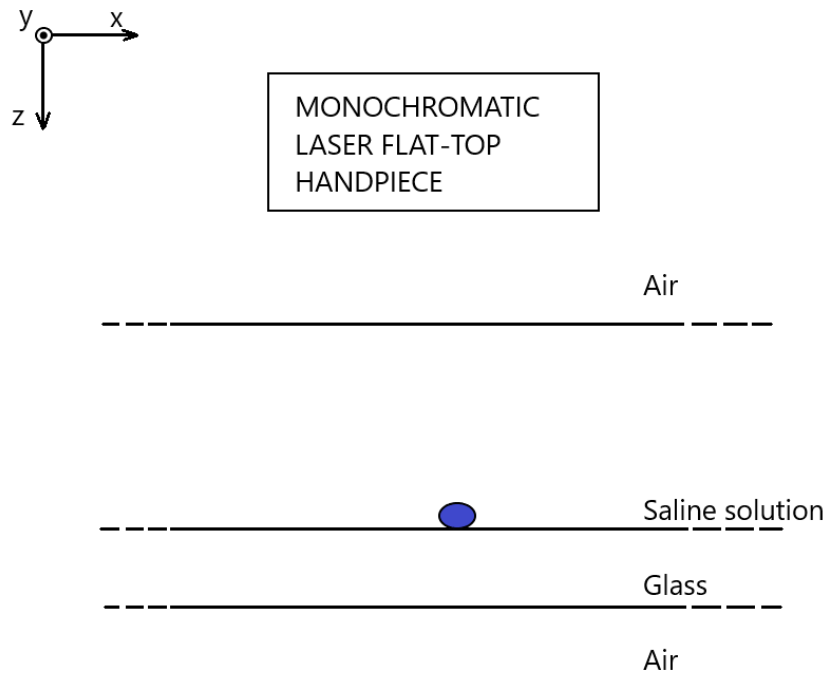


Figure 3.3. Proposed simplified experimental setup.

By exploiting the hypothesis of weak scatterer, the central idea of the algorithm is to impose a boundary condition $\mathbf{n} \times \mathbf{E}_{\text{inc}}$ on the boundary of the domain of investigation

instead that $\mathbf{n} \times \mathbf{E}_{\text{tot}}$, which is unknown. By setting the problem with a boundary condition in the form $\mathbf{n} \times \mathbf{E}$, thanks to the uniqueness theorem, we know that a single-field solution exists.

The problem is solved analytically by setting the bounds of the domain of interest using $\mathbf{n} \times \mathbf{E}_{\text{inc}}$, it is important to calculate \mathbf{E}_{inc} in the domain. To compute \mathbf{E}_{inc} we solve a structure using a transmission matrix-based algorithm without sample of mitochondria. The geometry consists of a multilayer structure of media with complex refractive indices. The incident electromagnetic field linearly polarized (along the x or y-axis) and propagates along the z-axis.

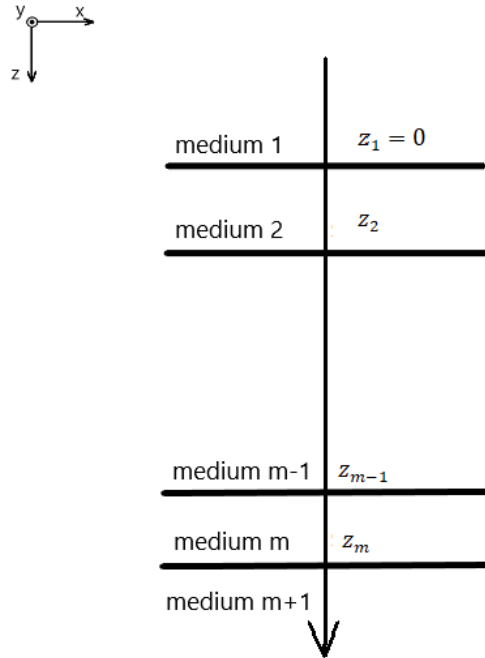


Figure 3.4. Geometry of multilayer structure

The first interface is located at $z = 0$. In this multilayer structure are present “m” interfaces, “m-1” layers of finite thickness and “m+1” overall layers (Figure 3.4). The relative media are characterized by μ_i (relative permeability) and ϵ_i (relative permittivity) $\in \mathbb{C}$. In the problem of interest, it is legitimate to assume that $\mu_i = 1$ for $i = 1, \dots, m + 1$. For the implementation of the problem, ϵ_i is characterized by complex dielectric media and is sufficient to provide $\epsilon_i \in \mathbb{C}$ for $i = 1, \dots, m + 1$. It is possible to compute the characteristic impedance Z_i , the refractive index n_i , and the wave number k_i of each dielectric media by using complex dielectric media.

$$Z_i = \sqrt{\frac{\mu_i}{\epsilon_i}} \quad (2)$$

$$n_i = \sqrt{\epsilon_i} \quad (3)$$

$$k_i = \frac{2\pi f}{C_0} n_i \quad (4)$$

The multilayer structure can be solved considering that the electric incident field propagate along the z-axis and is linearly polarized along the x-axis (denoted by \hat{x}), the transmitted electromagnetic field in medium 1 is denoted by:

$$\mathbf{E}_{\text{inc},1}(z) = A_1 e^{-jk_1 z} \hat{x} \quad (5)$$

$$\mathbf{H}_{\text{inc},1}(z) = \frac{A_1}{Z_1} e^{-jk_1 z} (\hat{z} \times \hat{x}) = \frac{A_1}{Z_1} e^{-jk_1 z} \hat{y} \quad (6)$$

The reflected electromagnetic field in medium 1 is denoted by:

$$\mathbf{E}_{\text{refl},1}(z) = B_1 e^{jk_1 z} \hat{x} \quad (7)$$

$$\mathbf{H}_{\text{refl},1}(z) = -\frac{B_1}{Z_1} e^{jk_1 z} \hat{y} \quad (8)$$

For $i = \{2, \dots, m\}$ is possible to calculate the transmitted and reflected electromagnetic field in every layer, denoted by:

$$\mathbf{E}_i(z) = (A_i e^{-jk_i z} + B_i e^{jk_i z}) \hat{x} \quad (9)$$

$$\mathbf{H}_i(z) = \frac{1}{Z_i} (A_i e^{-jk_i z} - B_i e^{jk_i z}) \hat{y} \quad (10)$$

The medium “m+1” is air, and there is no reflection, so we have important information of $B_{m+1} = 0$. If we know the incident field using the power of the laser source, we know A_1 . The other coefficients A_i and B_i between the layers 2 to “m” are unknowns; also unknown is the coefficient B_1 . In the “m” interface, we must impose the two continuity constraints of the tangential components of \mathbf{E} and \mathbf{H} , for which we obtain a “2m” boundary conditions. The vectorial problem will be solved by focusing on the scalar part. The problem of finding “2m” unknowns is solved more simply by using the transmission matrix method. We obtain the following scalar equations of the x component of the electric field $E_x(z)$ and y component of the magnetic field $H_y(z)$, denoted by:

$$E_x(z) = A e^{-jkz} + B e^{jkz} \quad (11)$$

$$H_y(z) = \frac{1}{Z} (A e^{-jkz} - B e^{jkz}) \quad (12)$$

For interface in $z = z_2 = z_1 + h$

$$E_x(z_2) = E_x(z_1 + h) = A e^{-jkz_1} e^{-jkh} + B e^{jkz_1} e^{jkh} \quad (13)$$

$$H_y(z_2) = H_y(z_1 + h) = \frac{1}{Z} (A e^{-jkz_1} e^{-jkh} - B e^{jkz_1} e^{jkh}) \quad (14)$$

The electric field $E_x(z_2)$ is calculated in function of $E(z_1)$ and $H(z_1)$

$$E_x(z_2) = Ae^{-jkz_1}(\cos hk - j \sin hk) + Be^{jkz_1}(\cos hk + j \sin hk) \quad (15)$$

$$E_x(z_2) = Ae^{-jkz_1} \cos hk + Be^{jkz_1} \cos hk - j(Ae^{-jkz_1} \sin hk - Be^{jkz_1} \sin hk) \quad (16)$$

$$E_x(z_2) = \cos hk (Ae^{-jkz_1} + Be^{jkz_1}) - j \sin hk (Ae^{-jkz_1} - Be^{jkz_1}) \quad (17)$$

$$E_x(z_2) = \cos hk (E(z_1)) - j \sin hk (Z H(z_1)) \quad (18)$$

The magnetic field $H_y(z_2)$ is calculated in function of $E(z_1)$ and $H(z_1)$

$$H_y(z_2) = \frac{1}{Z}(Ae^{-jkz_1}(\cos hk - j \sin hk) - Be^{jkz_1}(\cos hk + j \sin hk)) \quad (19)$$

$$H_y(z_2) = \frac{1}{Z}(Ae^{-jkz_1} \cos hk - jAe^{-jkz_1} \sin hk - Be^{jkz_1} \cos hk - jBe^{jkz_1} \sin hk) \quad (20)$$

$$H_y(z_2) = \frac{1}{Z}((Ae^{-jkz_1} - Be^{jkz_1}) \cos hk - j(Ae^{-jkz_1} + Be^{jkz_1}) \sin hk) \quad (21)$$

$$H_y(z_2) = H_y(z_1) \cos hk - j \frac{1}{Z} E_x(z_1) \sin hk \quad (22)$$

Hence, the final equation can be written in this way:

$$\begin{bmatrix} E_x(z_2) \\ H_y(z_2) \end{bmatrix} = \begin{bmatrix} \cos hk & -jZ \sin hk \\ -j\frac{1}{Z} \sin hk & \cos hk \end{bmatrix} \begin{bmatrix} E_x(z_1) \\ H_y(z_1) \end{bmatrix} = T \begin{bmatrix} E_x(z_1) \\ H_y(z_1) \end{bmatrix} \quad (23)$$

Where T is transmission matrix for a generic layer of thickness h.

We consider the vector \underline{V} defined by:

$$\underline{V}(x_i) = \begin{bmatrix} E_x(x_i) \\ H_y(x_i) \end{bmatrix} \quad (24)$$

And transmission matrix:

$$T_i = \begin{bmatrix} \cos h_i k_i & -jZ \sin h_i k_i \\ -j\frac{1}{Z_i} \sin h_i k_i & \cos h_i k_i \end{bmatrix} \quad (25)$$

with $h_i = z_i - z_{i-1}$ is thickness of the i-th layer, with $i = 2, \dots, m$.

For any finite thickness layer, the vector \underline{V} is equal to:

$$\underline{V}(z_i) = T_i \underline{V}(z_{i-1}) \quad (26)$$

Considering the tangential continuity of E and H in the interface, we obtain:

$$\left. \begin{array}{l} \underline{V}(z_i) = T_i \underline{V}(z_{i-1}) \\ \underline{V}(z_{i-1}) = T_{i-1} \underline{V}(z_{i-2}) \end{array} \right\} \rightarrow \underline{V}(z_i) = T_i T_{i-1} \underline{V}(z_{i-2}) \quad (27)$$

Then, we can proceed to medium 2 as

$$\underline{V}(z_i) = T_i T_{i-1} \dots T_2 \underline{V}(z_1) \quad (28)$$

If $i = m$ then the final expression is:

$$\underline{V}(z_m) = T_m T_{m-1} \dots T_2 \underline{V}(z_1) \quad (29)$$

In the medium “ $m+1$ ” there is no reflection, and we have $B_{m+1} = 0$:

$$\underline{V}(z_m) = \begin{bmatrix} E_x(z_m) \\ H_y(z_m) \end{bmatrix} = \begin{bmatrix} A_{m+1} e^{-jk_{m+1}z_m} \\ \frac{1}{Z_{m+1}} A_{m+1} e^{-jk_{m+1}z_m} \end{bmatrix} \quad (30)$$

When $z_1 = 0$, the equations in interface 1 are:

$$\underline{V}(z_1) = \begin{bmatrix} E_x(z_1) \\ H_y(z_1) \end{bmatrix} = \begin{bmatrix} A_1 e^{-jk_1 z_1} + B_1 e^{jk_1 z_1} \\ \frac{1}{Z_1} (A_1 e^{-jk_1 z_1} - B_1 e^{jk_1 z_1}) \end{bmatrix} = \begin{bmatrix} A_1 + B_1 \\ \frac{1}{Z_1} (A_1 - B_1) \end{bmatrix} \quad (31)$$

The definition of Transmission matrix \mathbf{T} is a complex matrix of dimension 2×2

$$\mathbf{T} = T_m T_{m-1} \dots T_2 = \begin{bmatrix} T_{11} & T_{12} \\ T_{21} & T_{22} \end{bmatrix} \quad (32)$$

$$\underline{V}(z_m) = \mathbf{T} \underline{V}(z_1) = \begin{bmatrix} T_{11} & T_{12} \\ T_{21} & T_{22} \end{bmatrix} \begin{bmatrix} A_1 + B_1 \\ \frac{1}{Z_1} (A_1 - B_1) \end{bmatrix} \quad (33)$$

$$\underline{V}(z_m) = \begin{bmatrix} A_{m+1} e^{-jk_{m+1}z_m} \\ \frac{1}{Z_{m+1}} A_{m+1} e^{-jk_{m+1}z_m} \end{bmatrix} = \begin{bmatrix} T_{11}(A_1 + B_1) + T_{12} \frac{1}{Z_1} (A_1 - B_1) \\ T_{21}(A_1 + B_1) + T_{22} \frac{1}{Z_1} (A_1 - B_1) \end{bmatrix} \quad (34)$$

$$A_{m+1}e^{-jk_{m+1}z_m} = T_{11}(A_1 + B_1) + T_{12}\frac{1}{Z_1}(A_1 - B_1) \quad (35)$$

$$\frac{1}{Z_{m+1}}A_{m+1}e^{-jk_{m+1}z_m} = T_{21}(A_1 + B_1) + T_{22}\frac{1}{Z_1}(A_1 - B_1) \quad (36)$$

We deduced the term A_{m+1} :

$$A_{m+1} = T_{11}(A_1 + B_1)e^{jk_{m+1}z_m} + T_{12}\frac{1}{Z_1}(A_1 - B_1)e^{jk_{m+1}z_m} \quad (37)$$

Replaced in the equation:

$$\frac{1}{Z_{m+1}}T_{11}(A_1 + B_1) + T_{12}\frac{1}{Z_1}\frac{1}{Z_{m+1}}(A_1 - B_1) = T_{21}(A_1 + B_1) + T_{22}\frac{1}{Z_1}(A_1 - B_1) \quad (38)$$

$$\begin{aligned} \frac{1}{Z_{m+1}}T_{11}B_1 - T_{12}\frac{1}{Z_1}\frac{1}{Z_{m+1}}B_1 + \frac{1}{Z_{m+1}}T_{11}A_1 + \frac{1}{Z_{m+1}}T_{11}A_1 + T_{12}\frac{1}{Z_1}\frac{1}{Z_{m+1}}A_1 \\ = T_{21}A_1 + T_{21}B_1 + T_{22}\frac{1}{Z_1}A_1 - T_{22}\frac{1}{Z_1}B_1 \end{aligned} \quad (39)$$

$$\begin{aligned} \left(\frac{1}{Z_{m+1}}T_{11} - T_{12}\frac{1}{Z_1}\frac{1}{Z_{m+1}} - T_{21} + T_{22}\frac{1}{Z_1}\right)B_1 \\ = \left(T_{21} + T_{22}\frac{1}{Z_1} - \frac{1}{Z_{m+1}}T_{11} - T_{12}\frac{1}{Z_1}\frac{1}{Z_{m+1}}\right)A_1 \end{aligned} \quad (40)$$

We obtained B_1

$$B_1 = \frac{T_{21} + T_{22} \frac{1}{Z_1} - \frac{1}{Z_{m+1}} T_{11} - T_{12} \frac{1}{Z_1} \frac{1}{Z_{m+1}}}{\frac{1}{Z_{m+1}} T_{11} - T_{12} \frac{1}{Z_1} \frac{1}{Z_{m+1}} - T_{21} + T_{22} \frac{1}{Z_1}} A_1 \quad (41)$$

$$B_1 = \frac{Z_1 Z_{m+1} T_{21} + T_{22} Z_{m+1} - Z_1 T_{11} - T_{12}}{Z_1 T_{11} - T_{12} - T_{21} Z_1 Z_{m+1} + T_{22} Z_{m+1}} A_1 \quad (42)$$

Using the information of the term A_1 , it is possible to calculate the term B_1 which corresponds to coefficients of reflection in the medium 1. It is possible to calculate $E_x(z_1)$ and $H_y(z_1)$, and consequently the vector $\underline{V}(z_1)$.

The term A_{m+1} is calculated using A_1 , B_1 and the terms of the transmission matrix T_{11} and T_{12} .

The vector $\underline{V}(z_i)$ is calculated using the following equations:

$$\underline{V}(z_2) = T_2 \underline{V}(z_1) = T_2 \begin{bmatrix} E_x(z_1) \\ H_y(z_1) \end{bmatrix} \quad (43)$$

$$\underline{V}(z_3) = T_3 \underline{V}(z_2) = T_3 \begin{bmatrix} E_x(z_2) \\ H_y(z_2) \end{bmatrix} \quad (44)$$

⋮

$$\underline{V}(z_{m-1}) = T_{m-1} \underline{V}(z_{m-2}) = T_{m-1} \begin{bmatrix} E_x(z_{m-2}) \\ H_y(z_{m-2}) \end{bmatrix} \quad (45)$$

At this point, we can calculate the electromagnetic fields in every medium for any z position.

3.2 Implementation of the electromagnetic model using finite element method with homogeneous mitochondria model

A laser generates the electromagnetic field in the experimental setup previously studied. It comes out of a flat-top handpiece that can guarantee good illumination uniformity largely independent of the distance of the handpiece from the target. For these reasons, with a good approximation, the content of the incubation chamber will be illuminated by a monochromatic uniform plane wave propagating along the z-axis and polarized in the x or y-axis. Such a monochromatic uniform plane wave, whose time-harmonic dependence factor $e^{j\omega t}$ is assumed and suppressed in the following (ω is the angular frequency and t is time)[98] [99], propagates inside the incubation chamber. When no mitochondria are present, it interacts with a multilayer structure of plane layers made up of air, saline solution, glass, and air, if we neglect the regions very close to the vertical walls of the chamber. This problem can be easily considered and exploited just to give preliminary indications on the magnitudes of the quantities of interest. The thicknesses of the media involved in this experimental setup have complex refractive indices (n_{ss} is the complex refractive index of saline solution, and n_g is the complex refractive index of glass) and are known quantities for all the wavelengths of interest. In the experimental setup, the thickness and the refractive index (t_m and n_m) of the plane layer representing the cluster of mitochondria have to be considered as variable quantities to analyze for different situations of potential interest. In general, the complex refractive index n is defined by $n = n' - jn''$, $n' > 0$, $n'' \geq 0$, where n' is real part of refractive index and n'' is imaginary part of refractive index, very often the imaginary part of refractive index “ n'' ” is calculated by using the corresponding absorption coefficient μ_a [m^{-1}], since $\mu_a = 4\pi n''/\lambda_0$ [100].

Three-dimensional models represented the best models for computing the electromagnetic field within mitochondria. Unfortunately, with present-day commercial simulators and computers it is not possible to consider models with all the details of the three-dimensional scattering problem of interest, because the corresponding domains of numerical investigations would be huge with respect to λ_0^3 . The typical values of t_g and t_{ss} are of the order of a few millimeters. The flat-top handpiece can be close to the air-saline solution interface, but, in any case, one has to consider the height of several millimeters in all horizontal interfaces.

Moreover, the cross-section of the incubation chamber is about 1 cm^2 . Even neglecting the vertical walls of the chamber, one would have to deal with a domain of investigation of about 1 cm^3 . Considering that we are interested in λ_0 values of 808, 980, and 1064 nm, one easily understands that the domain of investigation could be as one thousand billion cubic wavelengths. To solve this problem, it is necessary to perform a good discretization of a three-dimensional domain, which means that it is necessary to consider a cubic wavelength. Consequently, it is required approximately one thousand degrees of freedom in any discretization procedure. We conclude that any realistic three-dimensional simulation should be able to deal with about 10^{15} unknowns, which is too large for present-day computers and simulators.

Fortunately, we can avoid such approach by observing that, independently of our knowledge of the details of the internal structure of the mitochondria, they are weak scatterers. The mitochondria have dimensions of the same order as the vacuum wavelength of interest for LLLT [101]. In terms of electromagnetic scattering, they behave as homogeneous ellipsoids having an estimated effective refractive index [97], [102], [103], which is close to the refractive index of the saline solution and glass. For the saline solution [104], [105] and glass [106], we can consider the information of complex refractive indices reported in Table 3.1.

λ_0 [nm]	n_{ss}'	$\mu_{a,ss}$ [m ⁻¹]	n_{ss}''	n_g'	$\mu_{a,g}$	n_g''
808	1.331	1.95	1.25×10^{-7}	1.511	0.170	1.09×10^{-8}
980	1.328	50.2	3.91×10^{-7}	1.508	0.122	9.50×10^{-9}
1064	1.328	16.2	1.37×10^{-6}	1.507	0.099	8.37×10^{-9}

Table 3.1. Complex refractive indices of saline solution and glass for different wavelengths.

The three-dimensional models are implemented using commercial electromagnetic software called COMSOL Multiphysics (Radiofrequency module version 5.5). This software employs the finite element method to solve the Maxwell's equations and compute the electromagnetic fields within the modeling domain. Under the assumption that the fields vary sinusoidally in time at a known angular frequency ω and that all material

properties are linear with respect to the field, the governing Maxwell's equations in three-dimensional are reduced to:

$$\nabla \times (\mu_r^{-1} \nabla \times \mathbf{E}) - \frac{\omega^2}{c_0^2} \left(\epsilon_r - \frac{i\sigma}{\omega\epsilon_0} \right) \mathbf{E} = 0 \quad (46)$$

where the relative permittivity and relative permeability are defined as ϵ_r and μ_r , c_0 is defined as the light of speed in vacuum and σ is defined as conductivity. the above equation is solved by using the electric field, $\mathbf{E} = \mathbf{E}(x, y, z)$, throughout the modeling domain, and \mathbf{E} is a vector with components \mathbf{E}_x , \mathbf{E}_y and \mathbf{E}_z . The above equation is solved via the finite element method [107].

In the boundaries of the three-dimensional model, the impedance boundary conditions (or Leontovich boundary conditions) are applied for the limited domain of interest [108], [109] when is considered the presence of mitochondria. The Leontovich boundary condition is used in classical electrodynamic problems related to the tangential component of the electric field \mathbf{E}_t and magnetic field \mathbf{H}_t on the surface of well- conducting bodies. It is defined using the following equation:

$$\mathbf{E}_t = R_s(1 + j)\mathbf{H}_t \times \mathbf{n} \quad (47)$$

Where R_s is defined as surface resistance and is equal to $1/\delta\sigma$.

All the present results have been performed on an HP Z240 workstation equipped with an Intel core i7-7700 quad-core processor with 64 GB of RAM.

The optical properties of mitochondria (n_m' and $\mu_{a,m}$) are expected in the ranges [1.35-1.45] and [20 - 150] m^{-1} , respectively, whereas $n_m'' \in [1.28 \times 10^{-6}, 9.61 \times 10^{-6}]$ at $\lambda_0 = 808$ nm [97], [102], [103]. The same ranges are retained at 980 and 1064 nm. Since the field in a mitochondrion is not affected by the neighboring mitochondria, we can consider the presence of small numbers of mitochondria in our models. The few mitochondria considered in our three-dimensional models generate the scattered field, which becomes negligible with respect to the incident field [107], at a small distance away

from the scatterers. For this reason, we will approximate the scattering problems of interest by enforcing inhomogeneous impedance boundary conditions [107], [110]–[112] on a surface enclosing the few mitochondria that we will consider. The negligible amplitude of the scattered field on such a surface allows us to calculate the inhomogeneous term of the impedance boundary condition using the incident field provided by the analytical procedure described above [107].

Some configurations of the three-dimensional models that are studied are presented below:

- The model of the isolated mitochondrion is shown in Figure 3.5.
- The model of seven horizontal mitochondria is shown in Figure 3.6.
- The model of the periodic arrangement of mitochondria is shown in Figure 3.7 (in this case, the boundary conditions on the lateral surfaces of the limited domain will be replaced by periodic boundary conditions [113]).

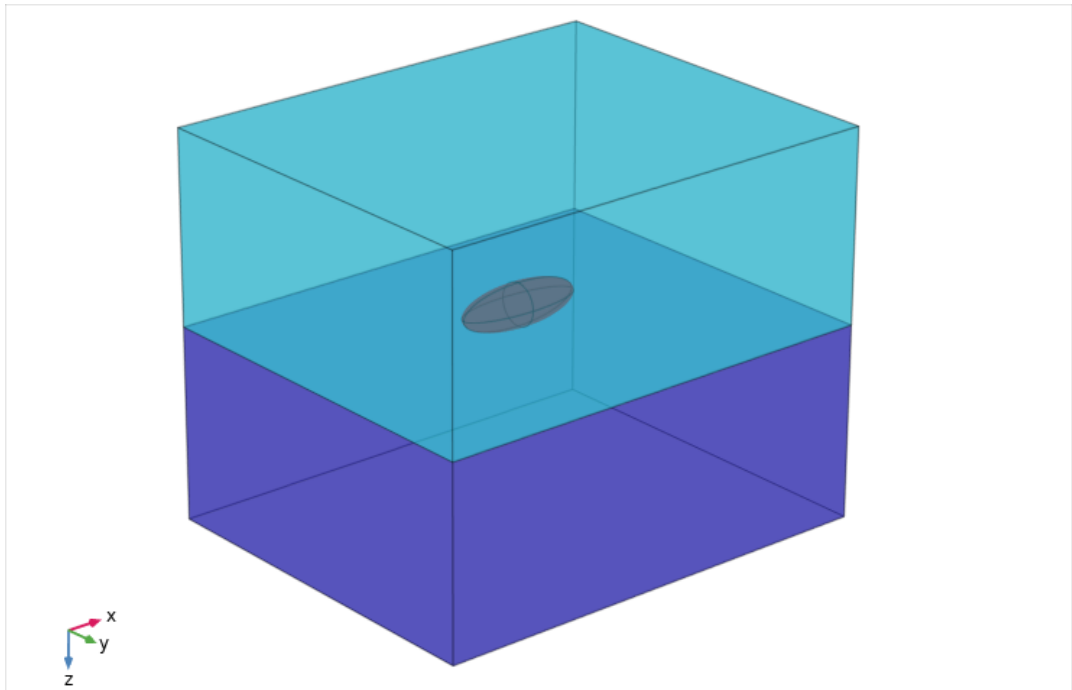


Figure. 3.5. Three-dimensional model of isolated mitochondrion

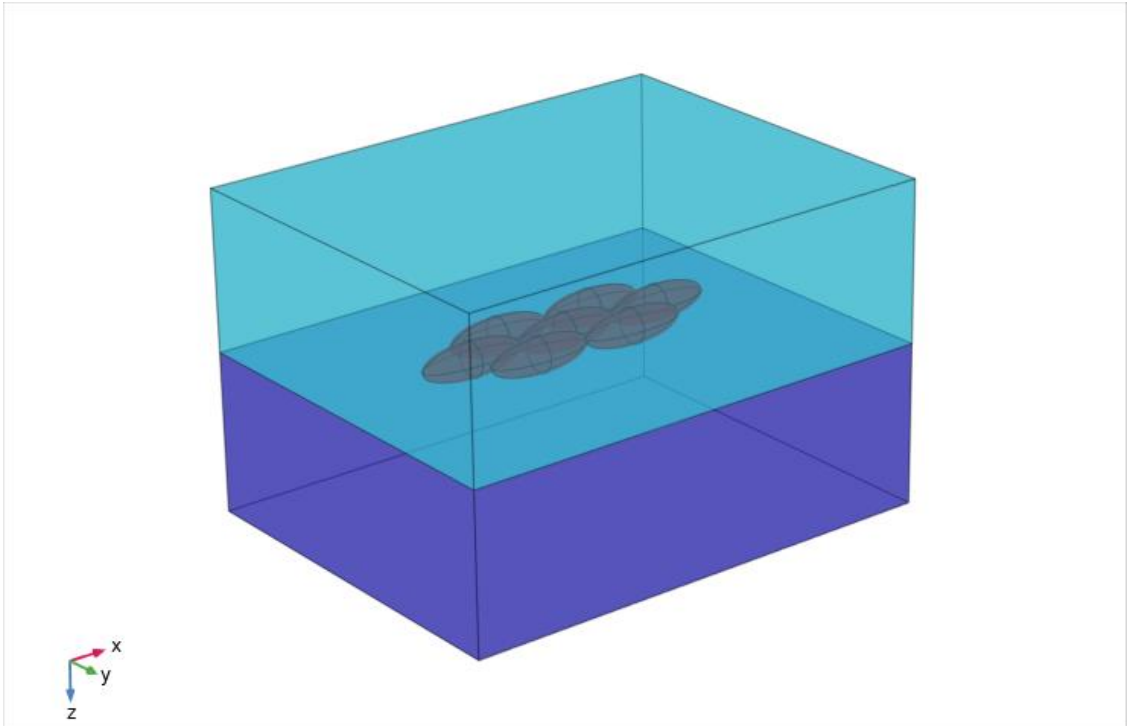


Figure 3.6. Three-dimensional model of seven horizontal mitochondria.

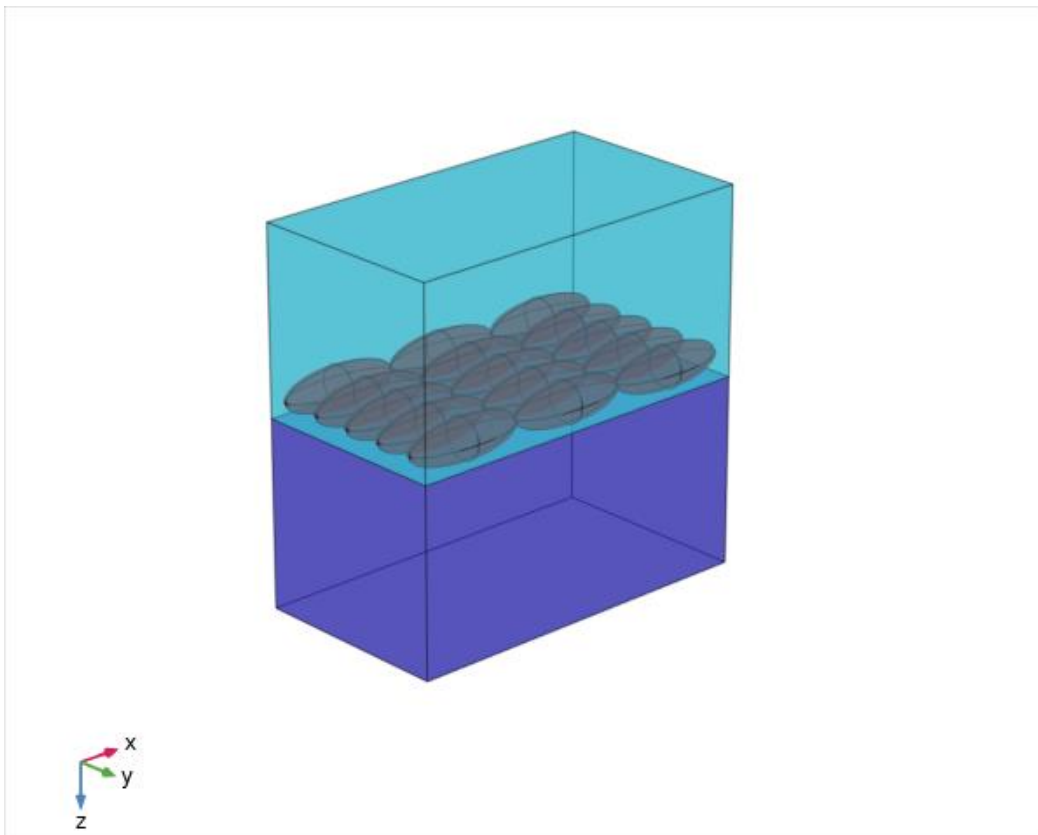


Figure 3.7. Three-dimensional model of periodic array of mitochondria.

3.3 Stability of the three-dimensional electromagnetic model

In the previous section, we defined several three-dimensional electromagnetic models involving the possible disposition of mitochondria. To find the optimal distance of mitochondrion to the surface of the limited domain for obtaining reliable results and simulation times not higher, is considered the model defined in Figure 3.5. The optimal distance should be found by balancing the need to consider small volumes of the domain of investigation, resulting in simulations with few unknowns and increasing the separation between the boundary and the scatterer.

For this analysis, we consider $\lambda_0 = 980$ nm, the constitutive parameters used in Table 3.1. For the simulation, we used the parameters of the mitochondrion, giving the largest scattering effect to consider the worst case, which is $n_m' = 1.45$ and $\mu_a = 150$ [m^{-1}]. The geometrical parameter of the ellipsoidal mitochondrion is the diameter d_m and length l_m equal to 1 and 3 micrometers, respectively. Since it is known that the minimum distance should be at least a few wavelengths, we consider such a distance equal to 1, 1.5, 2, ..., 5 micrometers.

Next, in the smaller numerical domain a cubic grid of $N=49011$ points uniformly distributed at every $0.1 \mu\text{m}$. In the smallest numerical domain, if we denote by $E_l(r_i)$, ($l = 1, 2, \dots, 9$), the electric field computed at the point r_i by the numerical simulator, the three-dimensional geometric parameters are $w_{3D} = 5, 6, \dots, 13 \mu\text{m}$, $h_{3D} = 3, 4, \dots, 11 \mu\text{m}$, $t_{3D,ss} = 2, 3, \dots, 10 \mu\text{m}$ and $t_{3D,g} = 1, 2, \dots, 9 \mu\text{m}$. The root mean square is calculated for the difference field $\mathbf{E}_{m+1} - \mathbf{E}_m$ and $\mathbf{H}_{m+1} - \mathbf{H}_m$ to satisfy our requirement.

$$\text{rms}(\Delta \mathbf{E}_m) = \sqrt{\frac{1}{N} \sum_{i=1}^N |\mathbf{E}_{m+1}(r_i) - \mathbf{E}_m(r_i)|^2} \quad (48)$$

In all simulations, we have considered an impinging monochromatic plane wave having a power density of 1 Wcm^{-2} . For these simulations, the incident field is polarized along the y-axis. The next figures present the behavior of $\text{rms}(\Delta \mathbf{E}_m)$ and $\text{rms}(\Delta \mathbf{H}_m)$ when $\lambda_0 = 980$ nm.

Figures 3.8 and 3.9 report the results of $\text{rms}(\Delta \mathbf{E}_m)$ and $\text{rms}(\Delta \mathbf{H}_m)$. The behaviors of the root mean square of the difference stabilize at a value of $m > 2$. For this reason, we can say that our results are stable and do not significantly change if the minimum distance of the boundary from the scatterer is larger than or equal to 1.5 micrometers. In order to have a margin of safety, such a distance is set to be at least 2.5 micrometers.

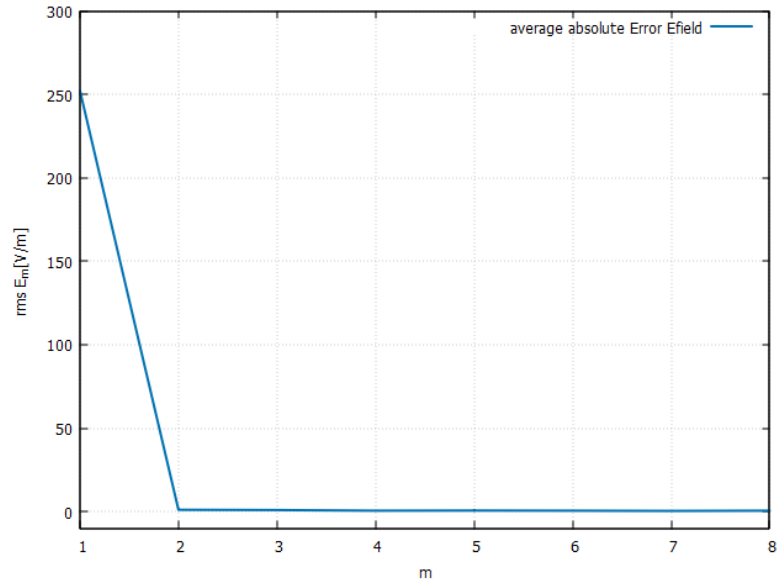


Figure 3.8. Behavior of the root mean square of the difference field $\mathbf{E}_{m+1} - \mathbf{E}_m$ versus m when $\lambda_0 = 980 \text{ nm}$.

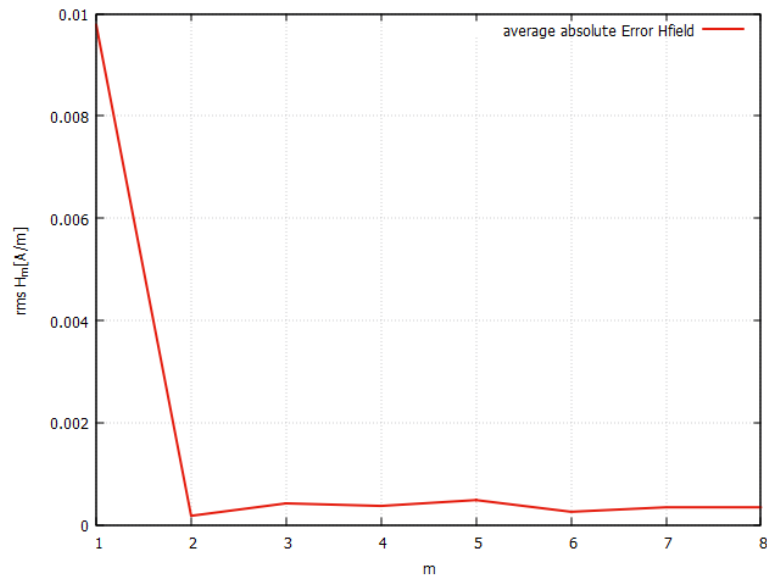


Figure 3.9. Behavior of the root mean square of the difference field $\mathbf{H}_{m+1} - \mathbf{H}_m$ versus m when $\lambda_0 = 980 \text{ nm}$.

Figures 3.10 and 3.11 present the magnitude of total electric field for isolated mitochondrion, which is essentially the same in both figures. The maximum value is approximately 2050 V/m and occurs within the mitochondrion, and the value of total electric field at $x = \pm 4 \mu\text{m}$ (Figure 3.10), and $x = \pm 4.5 \mu\text{m}$ (Figure 3.11) is about 1850 V/m. These results confirm that our model is stable when the separation is around 2.5 or 3 micrometers.

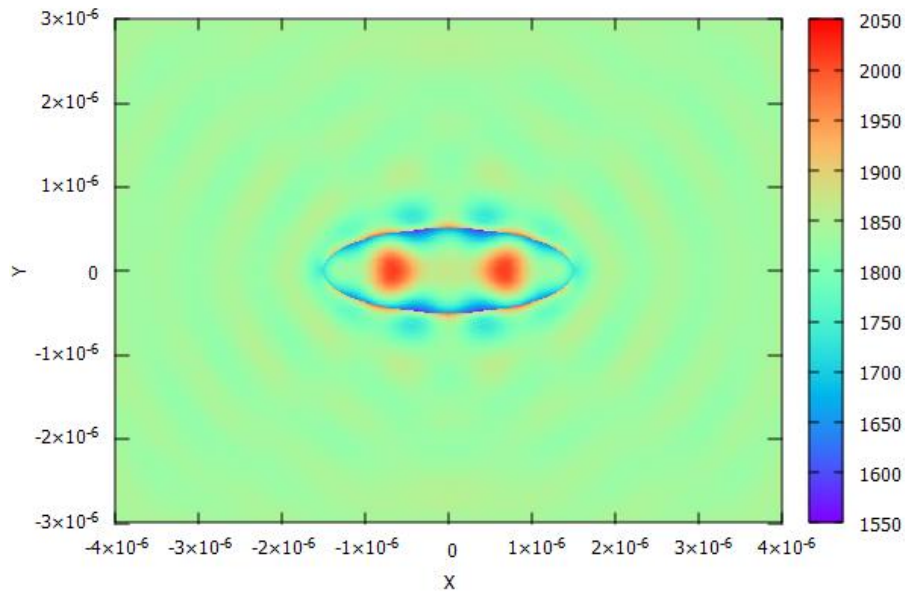


Figure 3.10. Total electric field for the three-dimensional model of an isolated mitochondrion with domain $w_{3D} \times h_{3D} \times t_{3D}$ equal to $8\mu\text{m} \times 6\mu\text{m} \times 6\mu\text{m}$ at $z = 4.995 \text{ mm}$

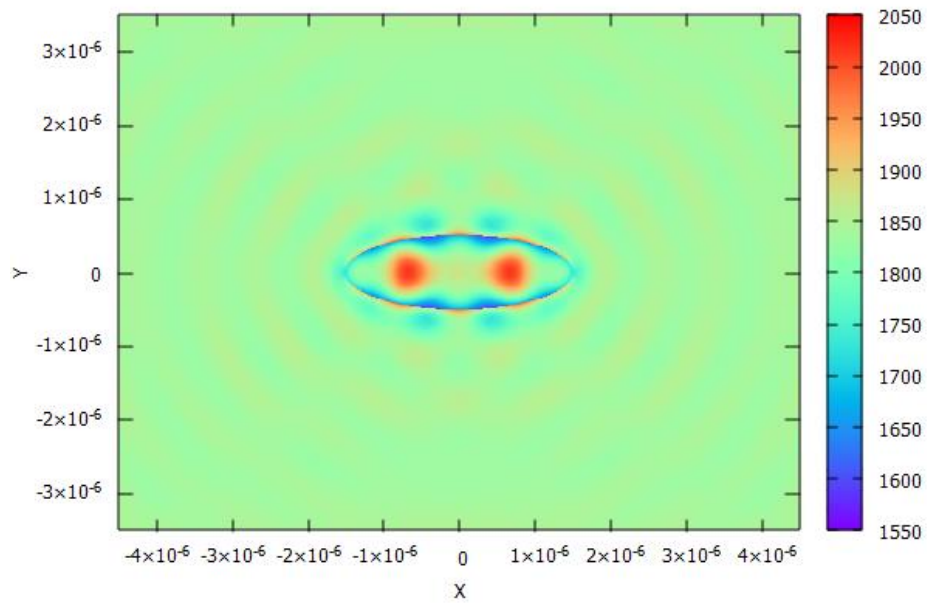


Figure 3.11. Total electric field for the three-dimensional model of an isolated mitochondrion with domain $w_{3D} \times h_{3D} \times t_{3D}$ equal to $9\mu\text{m} \times 7\mu\text{m} \times 7\mu\text{m}$ at $z = 4.995 \text{ mm}$

Figures 3.12 and 3.13 present the magnitude of total electric field at the plane xz at $y = 0$, showing a very intense electric reflected wave in the glass region (in $z \in [5 \text{ mm} - 5.0025 \text{ mm}]$), with a maximum value of 3200 V/m in both cases, whereas the value of the magnitude of total electric field at the boundaries at $x = \pm 4 \mu\text{m}$, and $\pm 4.5 \mu\text{m}$ of the mitochondria varies between 1400 and 2200 V/m .

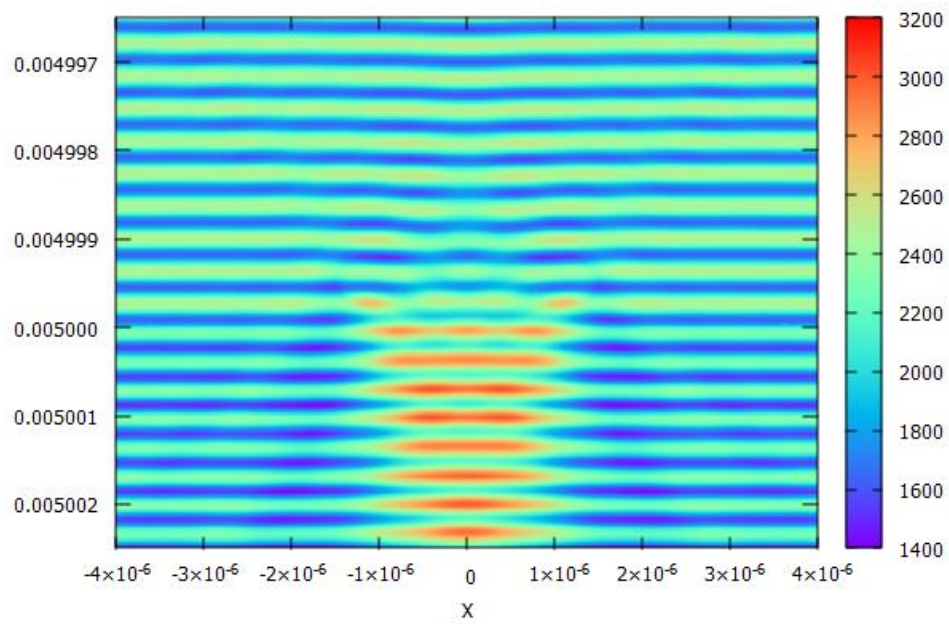


Figure 3.12. Total electric field in the three-dimensional model of an isolated mitochondrion with domain $8\mu\text{m} \times 6\mu\text{m} \times 6\mu\text{m}$ in plane XZ at $y = 0\text{ mm}$

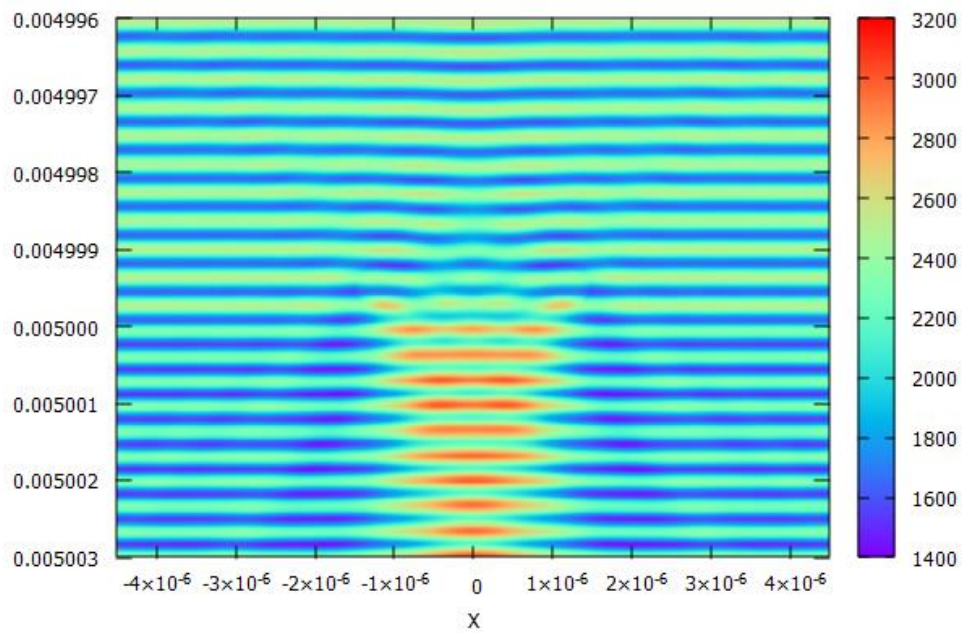


Figure 3.13. Total electric field in the three-dimensional model of an isolated mitochondrion with domain $9\mu\text{m} \times 7\mu\text{m} \times 7\mu\text{m}$ in plane XZ at $y = 0\text{ mm}$

Figures 3.14 and 3.15 present the magnitude of total electric field at the plane yz at $x=0$ presents a peak of intensity in the glass area, with a maximum value of 3000 V/m.

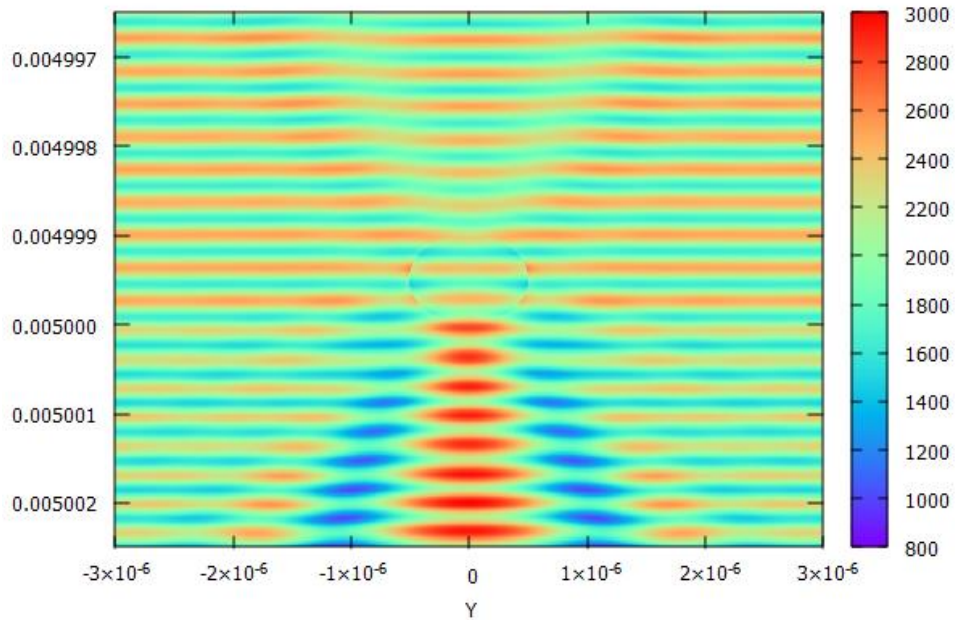


Figure 3.14. Total electric field in the three-dimensional model of an isolated mitochondrion with domain $8\mu\text{m} \times 6\mu\text{m} \times 6\mu\text{m}$ in plane YZ at $y = 0$ mm

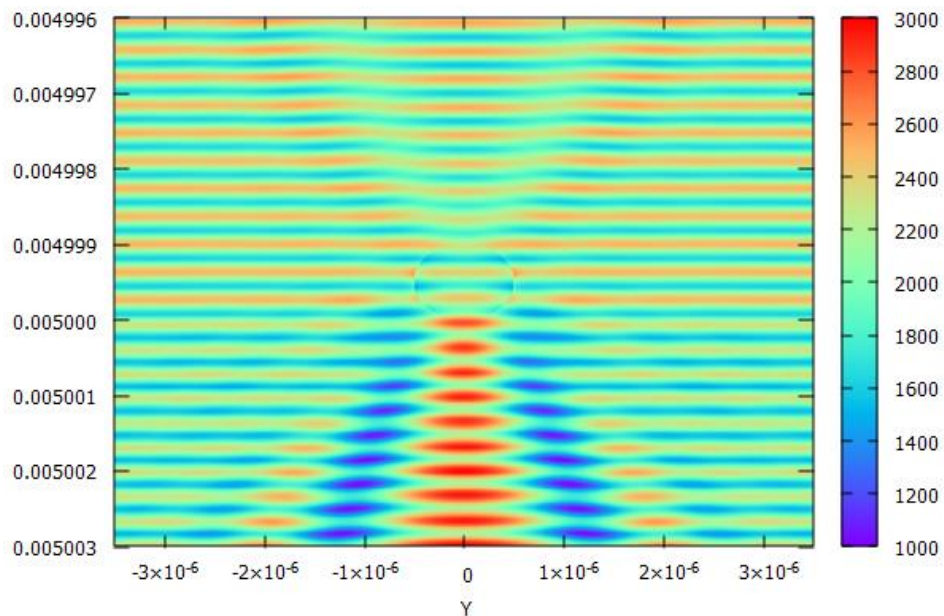


Figure 3.15. Total electric field in the three-dimensional model of an isolated mitochondrion with domain $9\mu\text{m} \times 7\mu\text{m} \times 7\mu\text{m}$ in plane YZ at $x = 0$ mm

3.4 Study of polarization for three-dimensional electromagnetic model

In this section, the effect of polarization on the proposed three-dimensional models is studied. The incident field is linearly polarized along the x or y-axis and an isolated mitochondrion model is considered. We show the magnitude of the electric field along the x, y and z-axis passing through the center of mitochondrion in Figures 3.16 to 3.18. For the mitochondrion with ellipsoidal shape is posed major axis along x-axis (length of mitochondrion) and the minor axis posed along y-axis, with diameter of 1 μm and length of 3 μm . The results are calculated for $n_m' = 1.425$, $\mu_{a,m} = 85 \text{ m}^{-1}$ and $\lambda_0 = 980\text{nm}$.

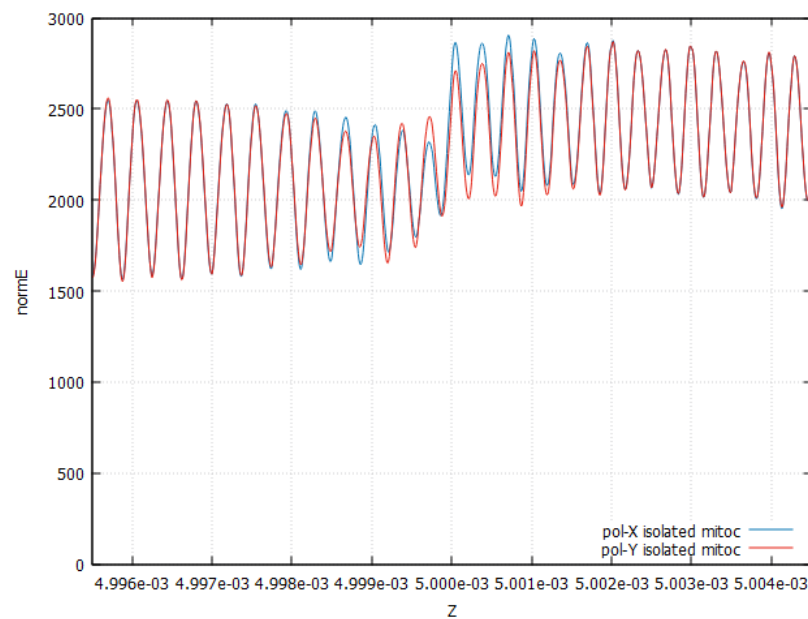


Fig 3.16. Total electric field along the z-axis passing through the center of gravity of the mitochondrion. The results are computed using the three-dimensional model involving an isolated mitochondrion for different linear polarizations.

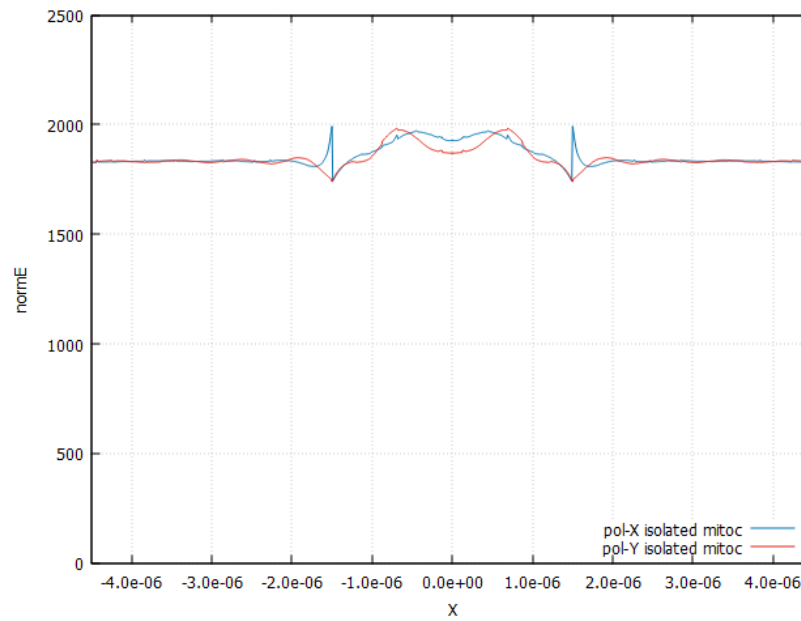


Fig 3.17. Total electric field along the x-axis passing through the center of gravity of the mitochondrion. The results are computed using the three-dimensional model involving an isolated mitochondrion for different linear polarizations.

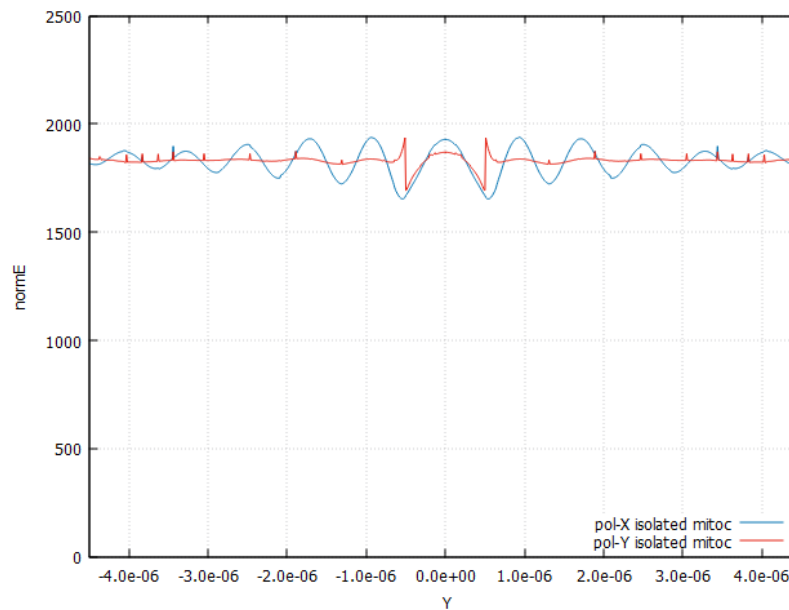


Fig 3.18. Total electric field along the y-axis passing through the center of gravity of the mitochondrion. The results are computed using the three-dimensional model involving an isolated mitochondrion for different linear polarizations.

The results present some differences when is polarized in x or y-axis, which is not large for the average values of the magnitude of the electric fields; if one focuses on the isolated mitochondrion model, we can see that the effects due to the different polarizations of the

incident field are negligible. The average energy density of the electromagnetic field E_d (in space and time) and average power density P_d (in space and time)[114] are computed for the isolated mitochondrion with homogeneous media in the region V_m , the following equations are denoted by:

$$E_d = \frac{1}{V_m} \int_V \frac{1}{4} (\epsilon_0 \epsilon'_{r,m} |\mathbf{E}|^2 + \mu_0 |\mathbf{H}|^2) dv \quad (49)$$

$$P_d = \frac{1}{V_m} \int_V \frac{1}{2} \omega \epsilon_0 \epsilon''_{r,m} |\mathbf{E}|^2 dv \quad (50)$$

Where $\epsilon'_{r,m}$ and $\epsilon''_{r,m}$ are the real part and the imaginary part of the relative permittivity of the homogeneous mitochondrion. The relative permittivity is calculated using the equation:

$$\epsilon_{r,m} = \epsilon'_{r,m} - j\epsilon''_{r,m} = n_m^2 = (n'_m - j \lambda_0 \mu_{a,m} / 4\pi)^2.$$

The effects of the dispersion characterized by the medium involved in the isolated mitochondrion model were verified to be negligible at the wavelength of interest. E_d and P_d are computed by using different polarizations for the isolated mitochondrion model. The results obtained by considering different polarizations of the incident field are almost identical, with a maximum difference for E_d of less than 1.64% and P_d less than 3.36%. The results of E_d and P_d using different polarizations is presented in Table 3.2.

	E_d [J/m ³]	P_d [W/m ³]
x-pol. incident field	3.957×10^{-5}	7.092×10^5
y-pol. incident field	3.893×10^{-5}	6.861×10^5

Table 3.2. Values of E_d and P_d computed for three-dimensional model of isolated mitochondrion.

The previous consideration does not exclude the possibility of getting reasonably good approximations from one-dimensional model. For this reason, we compare the outcomes of the one-dimensional model with the others three-dimensional models. In this way, we hope to derive some conclusions about the quality of the first results provided by the simple

model. The value of the optical parameters of mitochondria and the geometrical dimensions are fixed to $n_m' = 1.425$, $\mu_{a,m} = 85 \text{ m}^{-1}$, $l_m = 3\mu\text{m}$ and $d_m = 1\mu\text{m}$. The thickness of the layer of mitochondria is $t_{m,1D} = 1\mu\text{m}$ in the one-dimensional model. The magnitude of the total electric field is plotted along lines parallel to the x, y and z axes passing through the center of gravity of the central mitochondrion (when seven mitochondria model and periodic arrangement mitochondria are considered). The one-dimensional approximation is compared against the results obtained from the three-dimensional models involving isolated mitochondrion, seven mitochondria or periodic arrangements in a horizontal position.

Although the one-dimensional model cannot provide the detail about the spatial variation of the electromagnetic fields, the results obtained using it can nevertheless be a good first approximation to those obtained from the more accurate models. In particular, the maximum difference between the magnitude of total electric fields of the three-dimensional models and the one-dimensional one is less than 6.3%.

The results obtained using the 1D model with the three-dimensional models involving seven horizontal mitochondria and a periodic array of mitochondria are presented in Figures 3.19 to 3.21.

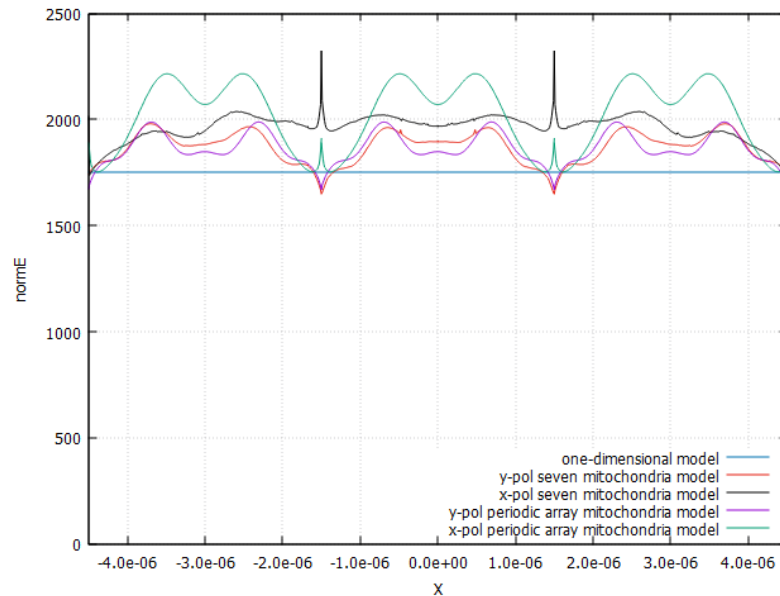


Fig 3.19. Total electric field along the x-axis passing through the center of gravity of the mitochondrion. The results are computed using the one-dimensional model, the three-dimensional models, and periodic array of mitochondria for different linear polarization.

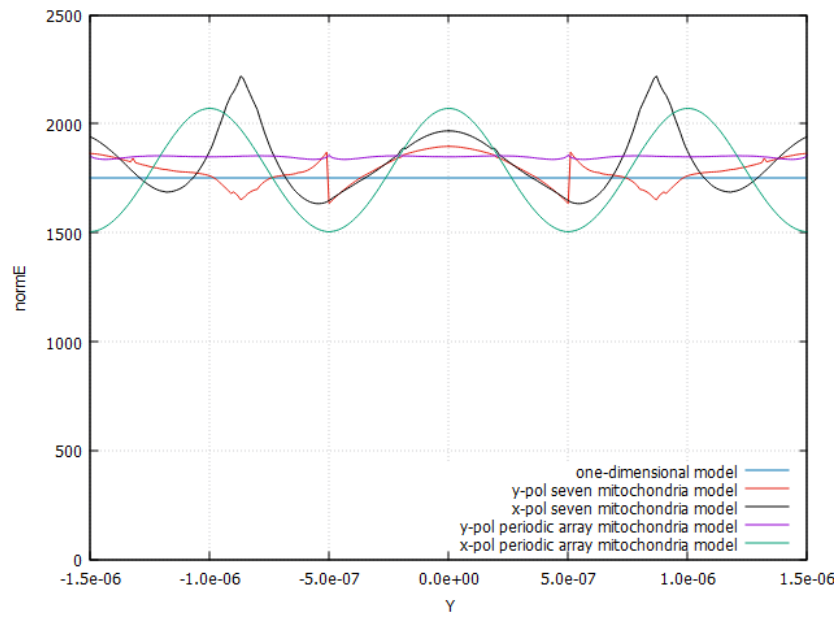


Fig 3.20. Total electric field along the y-axis passing through the center of gravity of the mitochondrion. The results are computed using the one-dimensional model, the three-dimensional models, and periodic array of mitochondria for different linear polarizations.

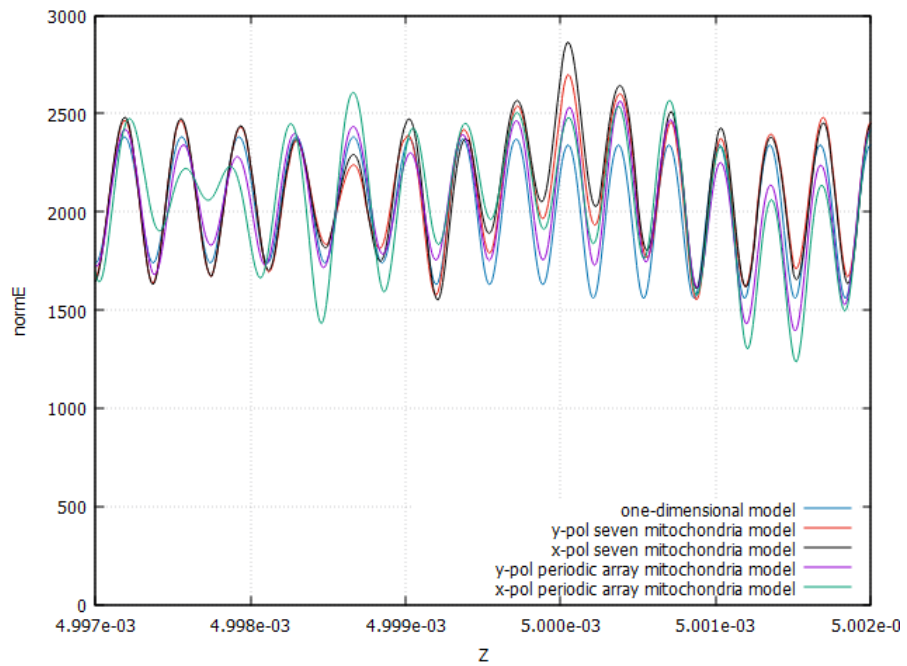


Fig 3.21. Total electric field along the z-axis. The results are computed using the one-dimensional model, the three-dimensional models, and periodic array of mitochondria for different linear polarizations.

In the Figure 3.21, the fields for the different models and polarizations are compared along a line parallel to the z-axis and passing through the center gravity of the central mitochondrion. The one-dimensional model result is close to all the three-dimensional models, giving a maximum difference of less than 5.2% of the incident field. In this case, the fields are comparable, although there is a maximum difference of about 12.6% in the glass area. However, the difference in the saline solution and inside mitochondria is not larger than 3.7% of the incident field. These considerations can be extended to the averages of energy and dissipated power densities. The E_d value given by the one-dimensional model differs from that obtained by the three-dimensional models involving either one isolated mitochondrion (Figure 3.5) or seven mitochondria in a horizontal disposition (Figure 3.6), respectively, by 4.94% and 2.63%. Likewise, the P_d value differs by 4.08% and 1.78% in the two cases. In Table 3.3 is resumed the results of E_d and P_d for all three-dimensional mitochondria model considered with different polarization.

	E_d [J/m ³]	P_d [W/m ³]
x-pol. incident field, isolated mitochondrion	3.957×10^{-5}	7.092×10^5
y-pol. incident field, isolated mitochondrion	3.893×10^{-5}	6.861×10^5
x-pol. incident field, seven mitochondria	3.843×10^{-5}	6.897×10^5
y-pol. incident field, seven mitochondria	3.776×10^{-5}	6.657×10^5
x-pol. incident field, periodic array	3.887×10^{-5}	6.965×10^5
y-pol. incident field, periodic array	3.807×10^{-5}	6.699×10^5

Table 3.3. Values of E_d and P_d computed for the three-dimensional models of isolated mitochondrion, seven mitochondria and periodic array.

For the three-dimensional models and polarizations studied in this section, we considered wavelengths of 808 nm and 1064 nm, E_d and P_d are calculated and shown in Tables 3.4 and 3.5. For 808 nm they present a maximum difference for E_d less than 2.4% and P_d less than 2.33%. For 1064 nm they present a maximum difference for E_d less than 2.63% and P_d less than 2.45%.

	E_d [J/m ³]	P_d [W/m ³]
x-pol. incident field, isolated mitochondria	5.380×10^{-5}	9.668×10^5
y-pol. incident field, isolated mitochondria	5.315×10^{-5}	9.429×10^5
x-pol. incident field, seven mitochondria	5.241×10^{-5}	9.429×10^5
y-pol. incident field, seven mitochondria	5.187×10^{-5}	9.209×10^5
x-pol. incident field, periodic array	5.273×10^{-5}	9.485×10^5
y-pol. incident field, periodic array	5.204×10^{-5}	9.237×10^5

Table 3.4. Values of E_d and P_d computed for the three-dimensional models for $\lambda_0 = 808$ nm.

	E_d [J/m ³]	P_d [W/m ³]
x-pol. incident field, isolated mitochondria	4.712×10^{-5}	8.057×10^5
y-pol. incident field, isolated mitochondria	4.635×10^{-5}	8.230×10^5
x-pol. incident field, seven mitochondria	4.582×10^{-5}	8.283×10^5
y-pol. incident field, seven mitochondria	4.513×10^{-5}	8.028×10^5
x-pol. incident field, periodic array	4.595×10^{-5}	8.273×10^5
y-pol. incident field, periodic array	4.545×10^{-5}	8.071×10^5

Table 3.5. Values of E_d and P_d computed for three-dimensional models for $\lambda_0 = 1064$ nm

Chapter 4 Electromagnetic implementation and simulation of complex and more realistic structures in the context of Low-Level Laser Therapy

4.1 Implementation of complex electromagnetic models involving mitochondria models

The internal structure of the mitochondria has been studied for many years, and diverse techniques exist to obtain images of its internal morphology, for example, electron-microscopy tomography, cryoelectron tomography, etc. [101], [115], [116]. Advanced electron microscopy techniques have revealed that the morphology of the cristae of mitochondria is more complex is shown in Figure 4.1. However, for our considerations, the simplified model should give the first results, which are also valid for the more complex morphology [116]–[118]. The mitochondria’s internal morphology consists of an outer membrane enclosing an inner membrane which presents a complex pattern of invaginations called cristae. These cristae have a lamellar shape or tubular shape in others [101], [117], [118]. This kind of structure will be considered in the following electromagnetic models. The size of healthy mitochondria present a length from 1 to 2 μm and width from 0.2 to 1 μm , the inner membrane is the place where the respiratory chain and oxidative phosphorylation occurs [115]. In [116] the authors present a mitochondrion model like parallelepiped-shaped with dimensions 1.5 x 0.3 x 0.3 μm consisting of 294 tubular cristae (7 layers, each with 42 cristae per plane).

Many researchers confirm that the centers of ATP production are located at the bottom of the cristae, located deep, away from the outer membrane [115], [116]. Previous works presented an analysis of electromagnetic propagation in mitochondria modeled presented a mitochondria model as a multilayer system with alternating indices of refraction represented by intramembrane and matrix mitochondrial [97], [119]. In this context, our work aims to study this morphology by considering electromagnetic models involving inhomogeneity inside the mitochondria. The effect of polarization is discussed.

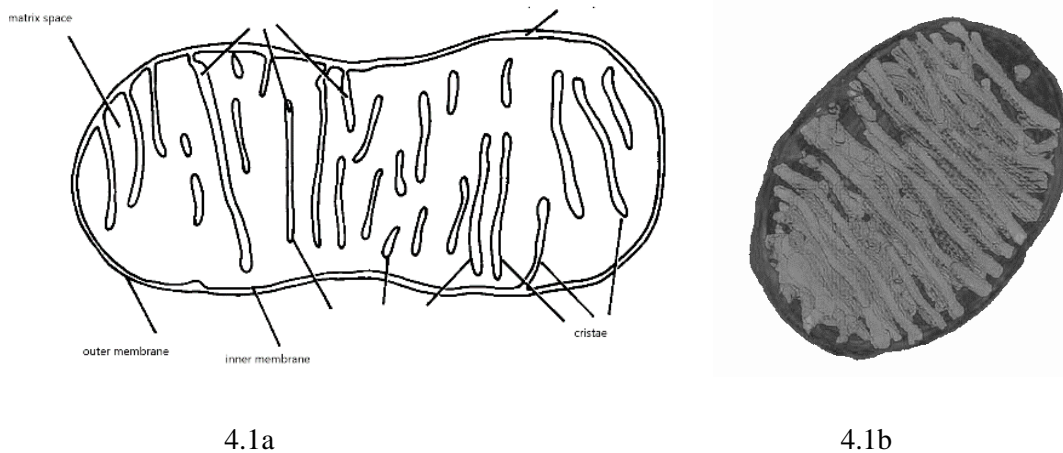


Figure 4.1. Morphology of mitochondrion. 4.1a. Internal morphology of mitochondria like lamellar. 4.1b. Internal morphology of mitochondria like tubular.

The electromagnetic models defined in this work are exploited to evaluate the electromagnetic field inside inhomogeneous mitochondria, considering the three-dimensional models previously studied in [96]. The initial analysis gave important results but did not consider the internal inhomogeneity of the mitochondrion. Some conclusions of this work must therefore be confirmed, taking into account possible internal inhomogeneities. These are two types of inhomogeneity classified as lamellar and tubular. The results are interesting, confirming that similar results can be obtained using the approximate three-dimensional model with homogeneous media. The electromagnetic models describing the morphology of the mitochondrion are presented below.

4.1.1 Lamellar mitochondria model

For our models, we are considering the mitochondria as weak scatterers and having an ellipsoidal shape, their length l_m is set to $2\ \mu\text{m}$, and their diameter d_m is fixed to $0.5\ \mu\text{m}$ (is used for all three-dimensional models). Two membranes surround the mitochondria: outer and inner mitochondrial membranes, which divide the mitochondrion into two sections: the intramembrane space and the matrix mitochondrial. Inside the mitochondrion, cristae which are perpendicular to the axis of the mitochondrion are present. The lamellar model is shown in Figure 4.2, the shape of the matrix membrane is similar to a “snake”, the width that connects lamellar layers in matrix mitochondrial is fixed to $50\ \text{nm}$. The distance between the external matrix and outer membrane is fixed at $50\ \text{nm}$. The thicknesses of the

membranes are fixed at $d_{intra} = 50$ nm and $d_{matrix} = 50$ nm when the organelles present high oxygen concentrations, this is defined as “respiring state.”

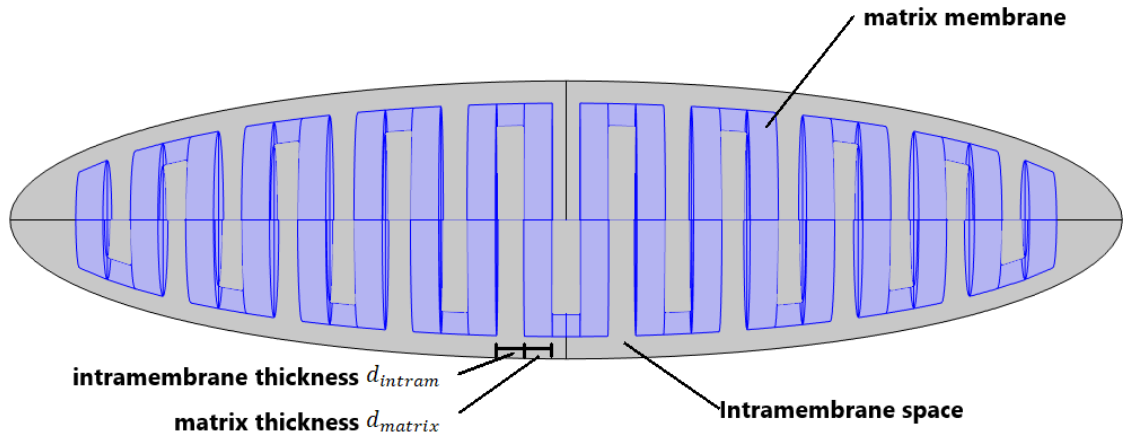


Figure 4.2. A three-dimensional lamellar model of inhomogeneous mitochondrion.

4.1.2 Tubular mitochondria model

In order to model the case of Figure 4.1b I implemented internal cylinders with a diameter fixed at 40 nm; these internal cylinders pass through the mitochondrion, orthogonally with the major axis of mitochondria. The tubular model presents a separation between every internal cylinder of 100 nm (Figure 4.3). The number of cylinders implemented is 126.

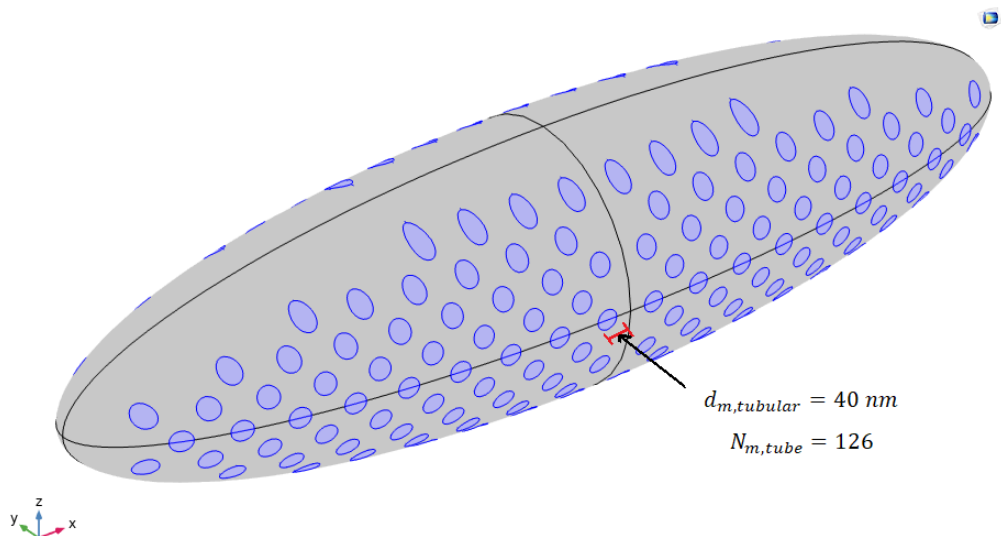


Figure 4.3. A three-dimensional tubular model of inhomogeneous mitochondrion.

4.1.3 Simplified lamellar mitochondria model

The simplified lamellar model is formed by an ellipsoid multilayer structure in which layers are orthogonal to major axis of the mitochondrion. The matrix membrane is defined with blue and the intramembrane space is defined with gray. The thicknesses are fixed at $d_{intra} = 50$ nm and $d_{matrix} = 50$ nm.

The geometric value of the experimental setup is fixed at $t_{ss} = 5$ mm and $t_g = 2$ mm. A monochromatic source is used, having a power density of 1 Wcm^{-2} and a wavelength of 808 nm is considered.

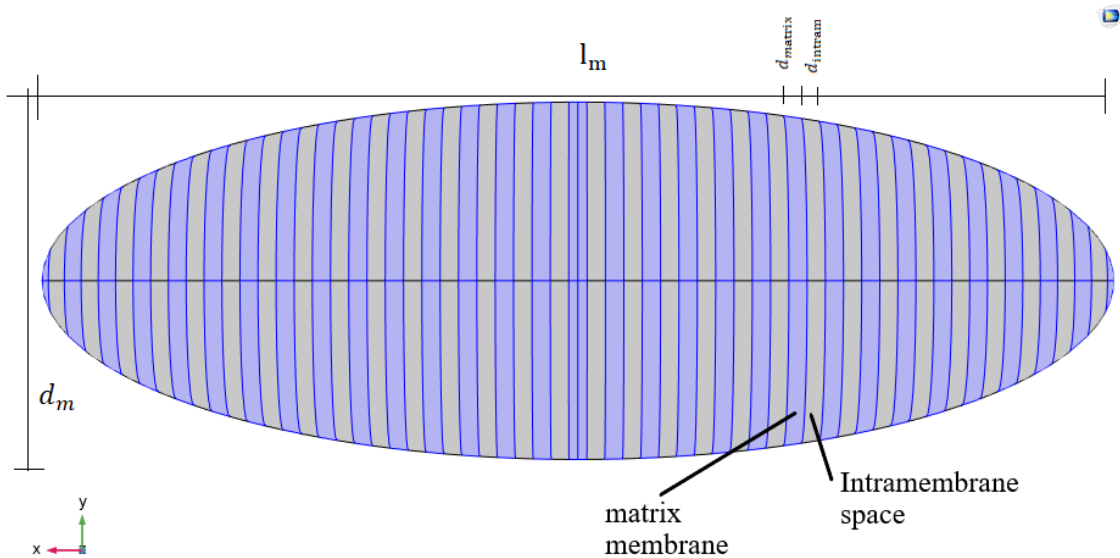


Figure 4.4. Three-dimensional simplified lamellar model of inhomogeneous mitochondrion

Several cases are proposed in which the mitochondrion is isolated in a horizontal position (Figure 4.5), a group of seven neighboring mitochondria is placed in horizontal position (Figure 4.6) and a periodic arrangement of mitochondria is placed in a horizontal position (Figure 4.7).

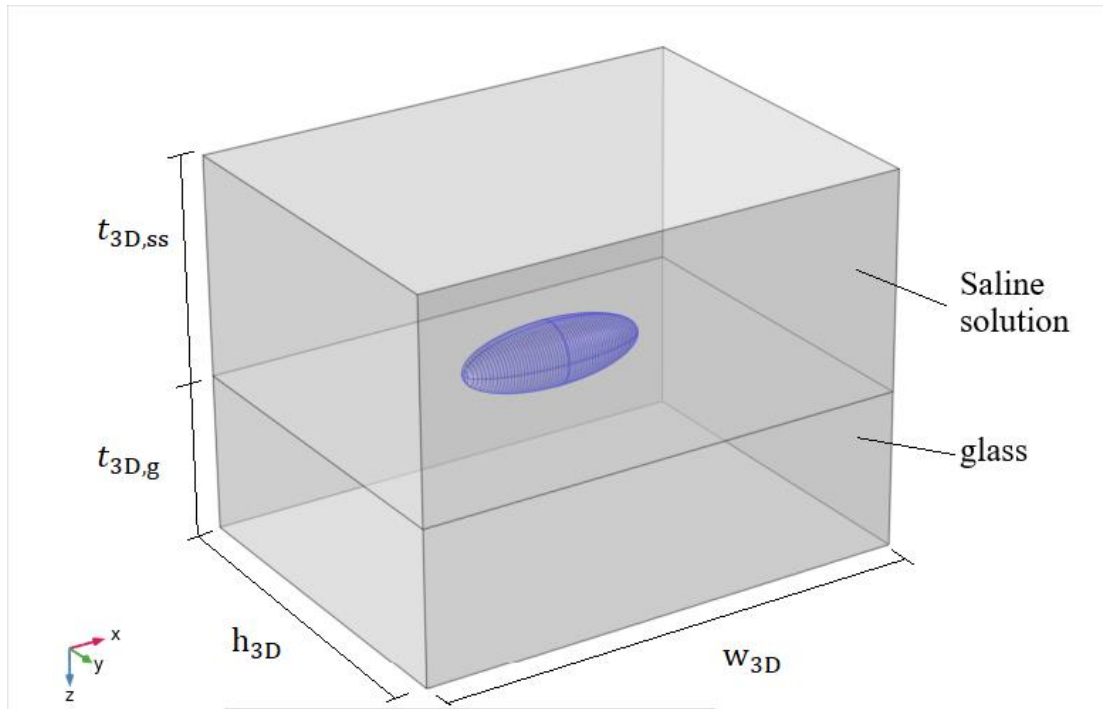


Figure 4.5. A three-dimensional model with one inhomogeneous mitochondrion placed in horizontal position.

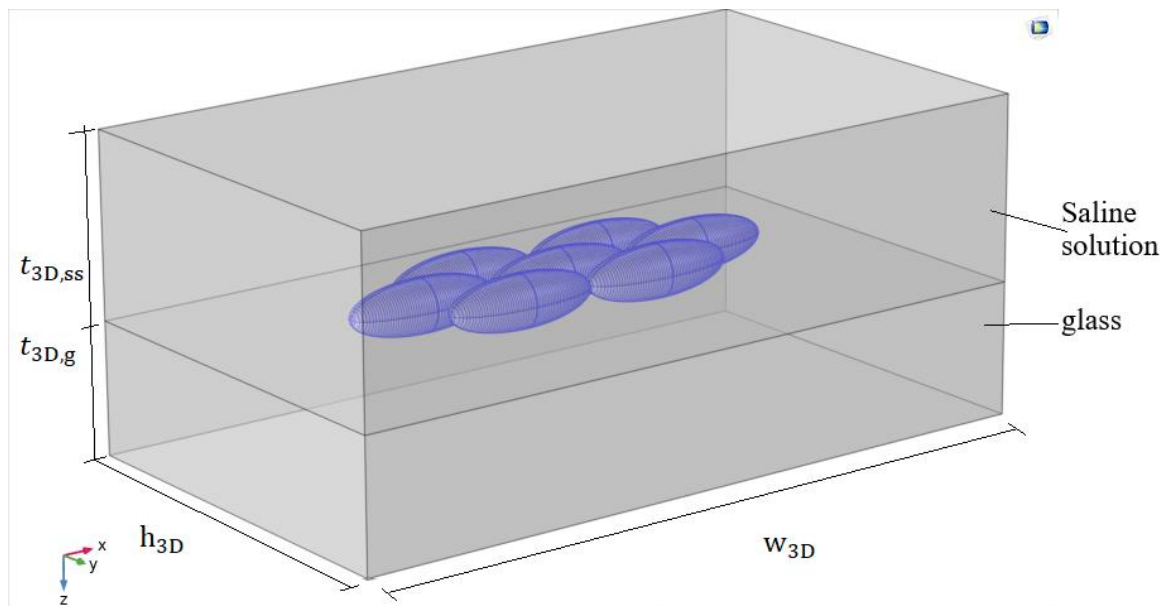


Figure 4.6. A three-dimensional model with seven inhomogeneous mitochondria representing a single layer placed in horizontal position.

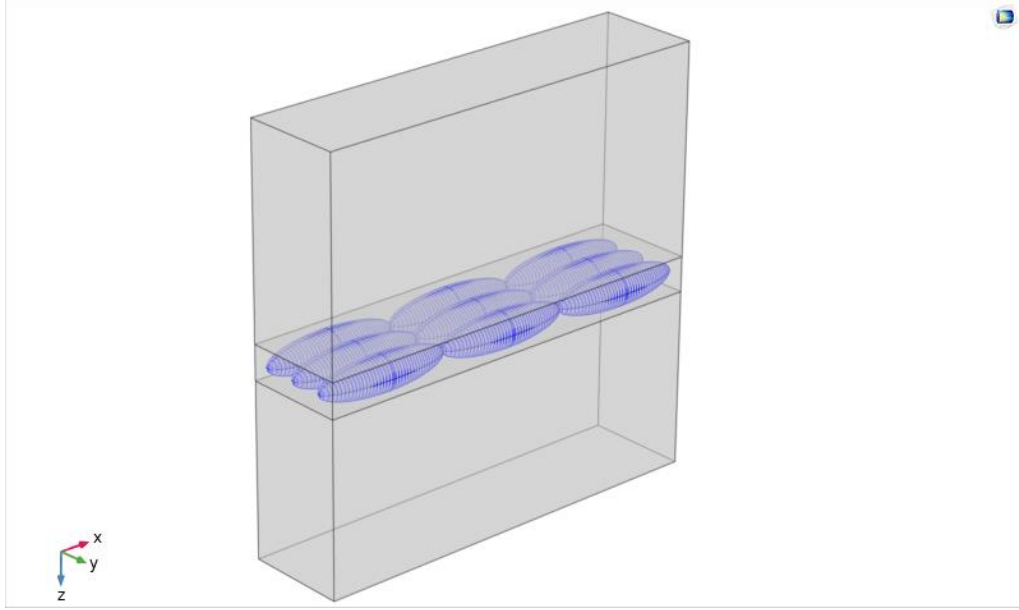


Figure 4.7. A three-dimensional model considering an array of inhomogeneous mitochondria with periodicity in horizontal position.

4.2 Numerical results of energy density, power density, polarization and scattering electric field

This section presents the effect of polarization in the presence of the three-dimensional electromagnetic models of inhomogeneous mitochondria. The results are calculated using a refraction index and attenuation coefficient of matrix membrane equal to $n'_{\text{matrix}} = 1.5$, $\mu'_{a,\text{matrix}} = 85 \text{ m}^{-1}$, and refraction index and attenuation coefficient of intramembrane space equal to $n'_{\text{intram}} = 1.35$, $\mu'_{a,\text{intram}} = 85 \text{ m}^{-1}$. These values are used when the organelle is in “respiring state” [120]. These results are compared to three-dimensional models with homogeneous mitochondria, the refractive index is the mean arithmetic of the present media’s refraction indices; for this case, $n'_{\text{mitoc}} = 1.425$ and $\mu'_{a,\text{mitoc}} = 85 \text{ m}^{-1}$.

The organelles are positioned horizontally in the range [4.99975, 5] mm along the z-axis, passing through the center of the central mitochondrion indicated in the previous Figures. The energy density and power density of the electromagnetic field (in average in space and time) in the volume V_m of the inhomogeneous mitochondrion are calculated using the following equations:

$$E_d = \frac{1}{V_m} \left\{ \int_{V_{\text{matrix}}} \frac{1}{4} (\epsilon_0 \epsilon'_{r,\text{matrix}} |\mathbf{E}|^2 + \mu_0 |\mathbf{H}|^2) + \int_{V_{\text{intram}}} \frac{1}{4} (\epsilon_0 \epsilon'_{r,\text{intram}} |\mathbf{E}|^2 + \mu_0 |\mathbf{H}|^2) \right\} \quad (51)$$

$$P_d = \frac{1}{V_m} \left\{ \int_{V_{\text{matrix}}} \frac{1}{2} \omega \epsilon_0 \epsilon''_{r,\text{matrix}} |\mathbf{E}|^2 + \int_{V_{\text{intram}}} \frac{1}{2} \omega \epsilon_0 \epsilon''_{r,\text{intram}} |\mathbf{E}|^2 \right\} \quad (52)$$

$$V_m = V_{\text{matrix}} + V_{\text{intram}} \quad (53)$$

The simplified lamellar model present similar results in comparison with lamellar model, however, the simplified model employes less computational resource and less simulation time. The maximum difference for E_d less than 1.17 % and P_d less than 1.04 %. For that reason, the simplified lamellar model is used for different configurations.

The energy and power density using three-dimensional models are presented in Tables 4.1 to 4.4. The effect of polarization and morphology is considered in the models. The result obtained by considering the diverse polarization of incident fields is practically the same, with a maximum difference for E_d less than 5.5% and P_d less than 5.4%.

	Figure 4.5	Figure 4.6	Figure 4.7
x-pol. Homogeneous model	5.394×10^{-5}	5.159×10^{-5}	5.194×10^{-5}
x-pol. Simplified lamellar model	5.357×10^{-5}	5.136×10^{-5}	5.168×10^{-5}
y-pol. Homogeneous model	5.245×10^{-5}	5.061×10^{-5}	5.050×10^{-5}
y-pol Simplified lamellar model	5.258×10^{-5}	5.072×10^{-5}	5.058×10^{-5}

Table 4.1. Values of E_d (J m^{-3}) computed by using different three-dimensional models and polarizations.

	Figure 4.5
x-pol. Tubular model	5.692×10^{-5}
y-pol. Tubular model	5.484×10^{-5}

Table 4.2. Values of E_d ($J m^{-3}$) computed by using three-dimensional tubular model for different polarizations.

	Figure 4.5	Figure 4.6	Figure 4.7
x-pol. Homogeneous model	9.659×10^5	9.243×10^5	9.332×10^5
x-pol. Simplified Lamellar model	9.655×10^5	9.264×10^5	9.343×10^5
y-pol. Homogeneous model	9.150×10^5	8.874×10^5	8.838×10^5
y-pol Simplified Lamellar model	9.145×10^5	8.875×10^5	8.827×10^5

Table 4.3. Values of P_d ($W m^{-3}$) computed by using different three-dimensional models and polarizations.

	Figure 4.5
x-pol. Tubular model	9.985×10^5
y-pol. Tubular model	9.247×10^5

Table 4.4. Values of P_d ($W m^{-3}$) computed by using three-dimensional tubular model and polarizations.

Figures 4.8 to 4.11 shown the total electric field for the different models and polarizations are compared, along a line parallel to the x and y-axis, passing through the center of gravity of the central mitochondrion. Figure 4.8 shown the incident electric field with x-polarized, the electric field inside the inhomogeneous mitochondrion presents energy jumps in correspondence with the internal morphology. This result is confirmed using different dispositions of organelles, for example, for a group of seven mitochondria (Figure 4.6) or a periodic arrangement of mitochondria (Figure 4.7). Moreover, when the incident field with y-polarized is used, these energy jumps are less evident and the response is more similar in comparison to homogeneous mitochondria model. These first observations are

later confirmed by studying the response of the scattering field for the three-dimensional models.

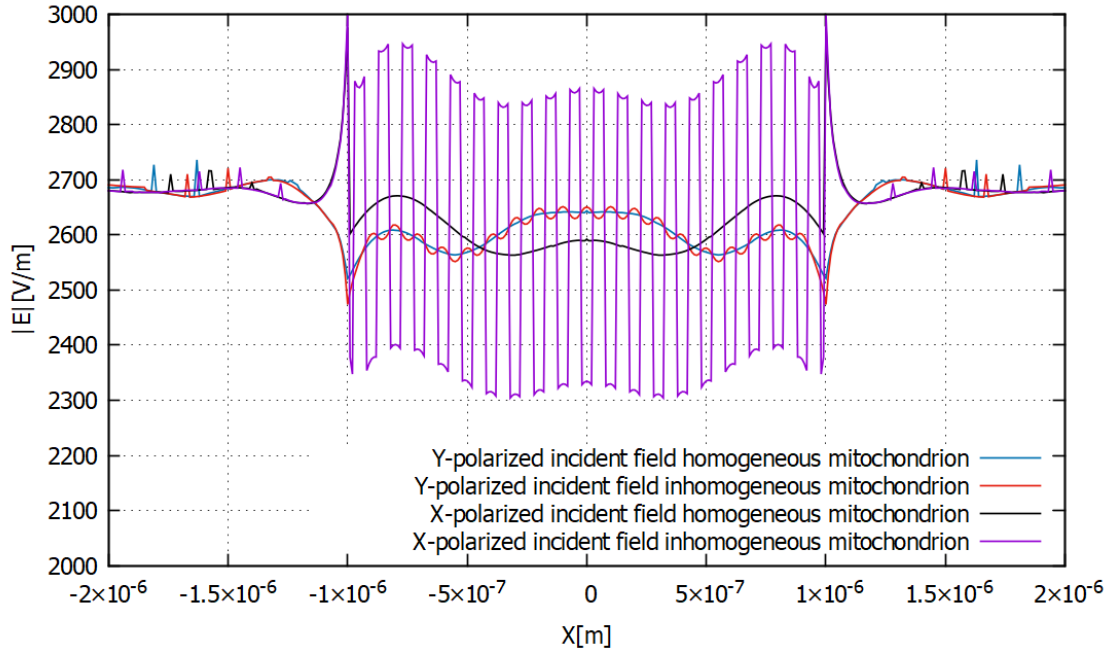


Figure 4.8. Behavior of $|\mathbf{E}|$ along a line parallel to the x axis, passing through the center of gravity of the mitochondrion. The results are computed using the model of Figure 4.5 and different polarizations.

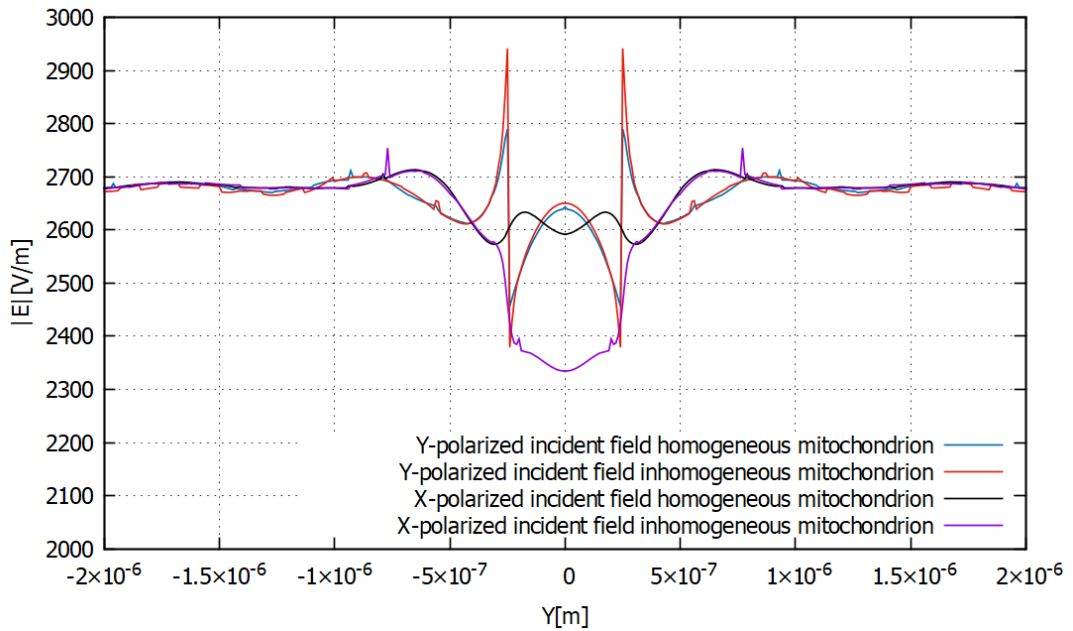


Figure 4.9. Behavior of $|\mathbf{E}|$ along a line parallel to the y axis, passing through the center of gravity of the mitochondrion. The results are computed using the model of Figure 4.5 and different polarizations.

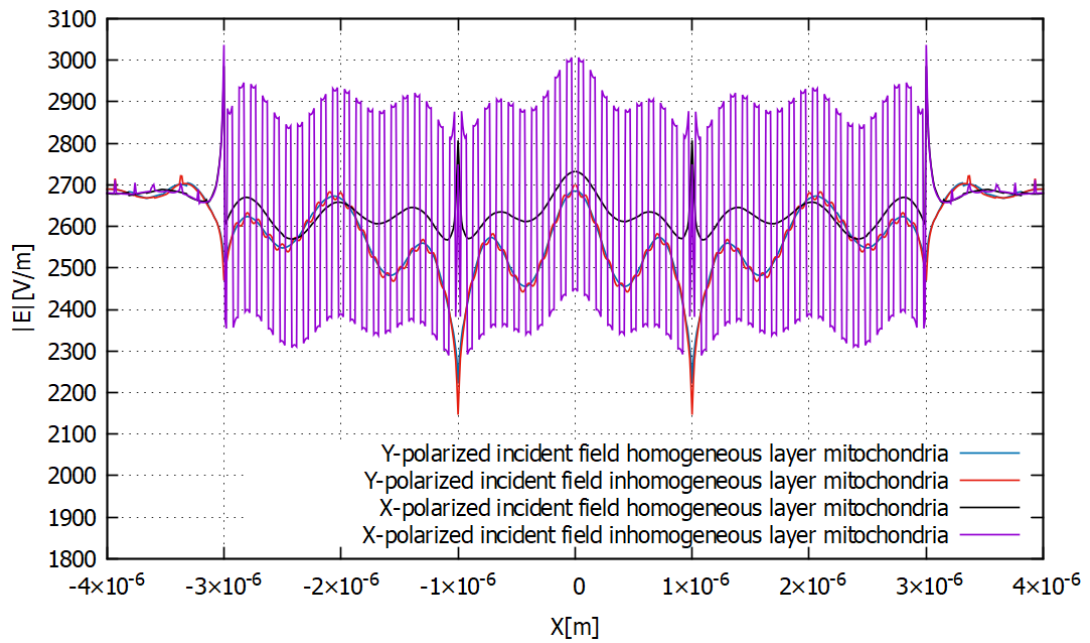


Figure 4.10. Behavior of $|\mathbf{E}|$ along a line parallel to the x axis, passing through the center of gravity of the central mitochondrion. The results are computed using the model of Figure 4.6 and different polarizations.

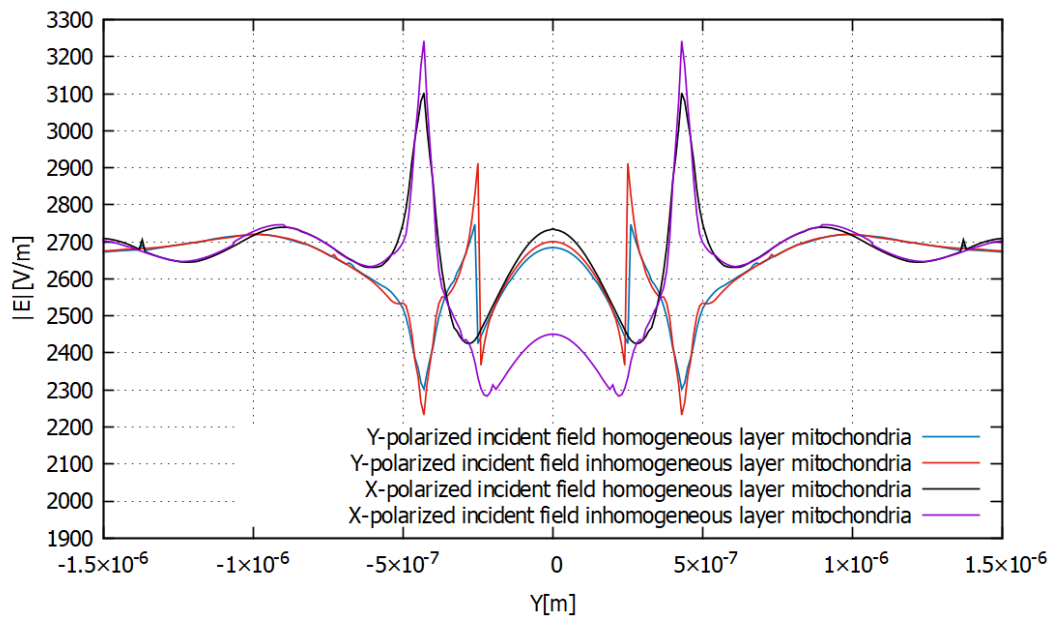


Figure 4.11. Behavior of $|\mathbf{E}|$ along a line parallel to the y axis, passing through the center of gravity of the central mitochondrion. The results are computed using the model of Figure 4.6 and different polarizations.

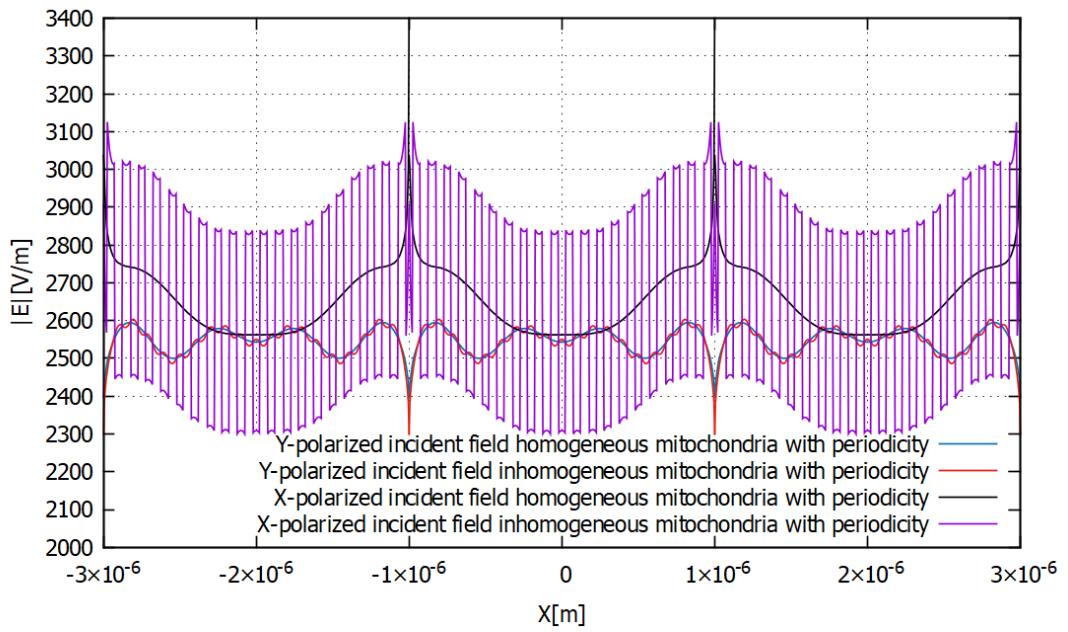


Figure 4.12. Behavior of $|\mathbf{E}|$ along a line parallel to the x axis, passing through the center of gravity of the central mitochondrion. The results are computed using the model of Figure 4.7 and different polarizations.

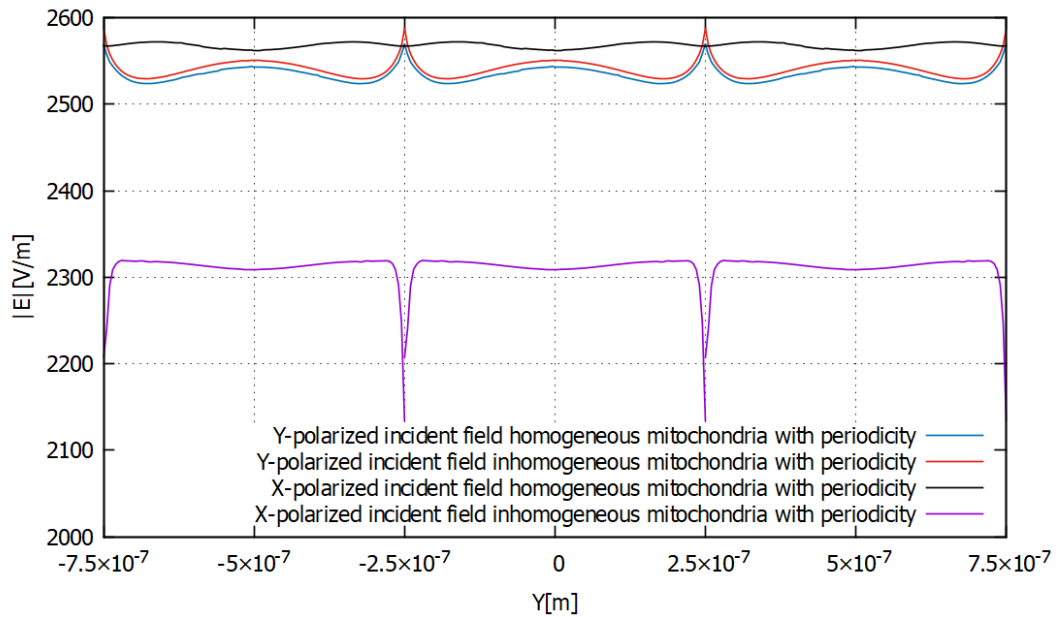
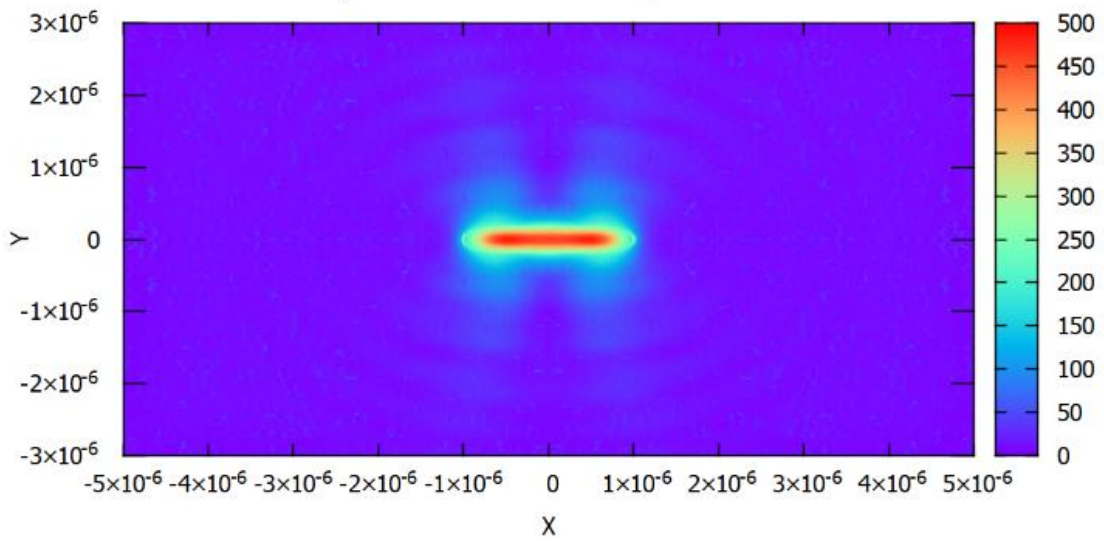


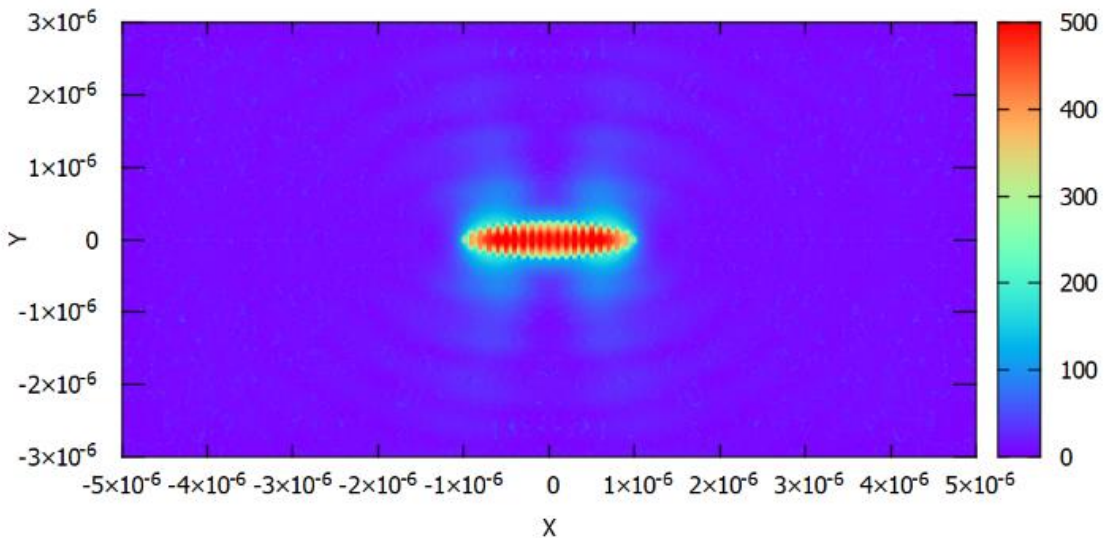
Figure 4.13. Behavior of $|\mathbf{E}|$ along a line parallel to the y axis, passing through the center of gravity of the central mitochondrion. The results are computed using the model of Figure 4.7 and different polarizations.

In most of our three-dimensional models, we assumed that the inhomogeneous mitochondria are weak scatterers and, for that reason is not necessary to consider the positions of far-away organelles view from the plane perpendicular to the direction of

propagation of the incident field. We define the scattered field \mathbf{E}_s , as the difference between the electric field in the presence of mitochondria and the electric field without the organelles (E_i). Figures 4.8 to 4.13 show the behavior of $|\mathbf{E}_s|$ on the plane $z = 4.99975$ mm passing through the center of gravity of the central mitochondria for the different configurations and polarizations. The fields are computed for the three-dimensional models involving an isolated mitochondrion, a group of seven mitochondria, and a periodicity array of mitochondria using simplified lamellar model.

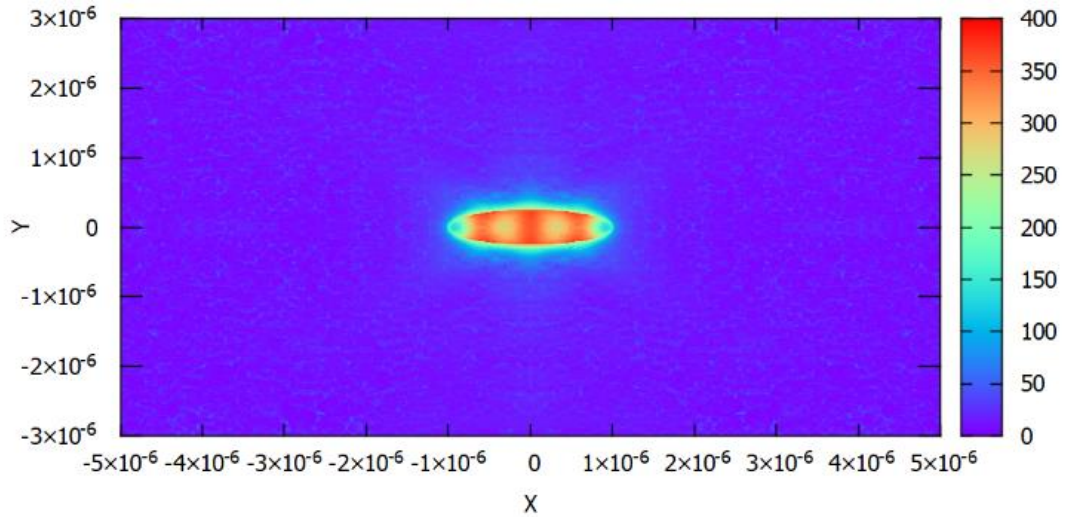


4.14a

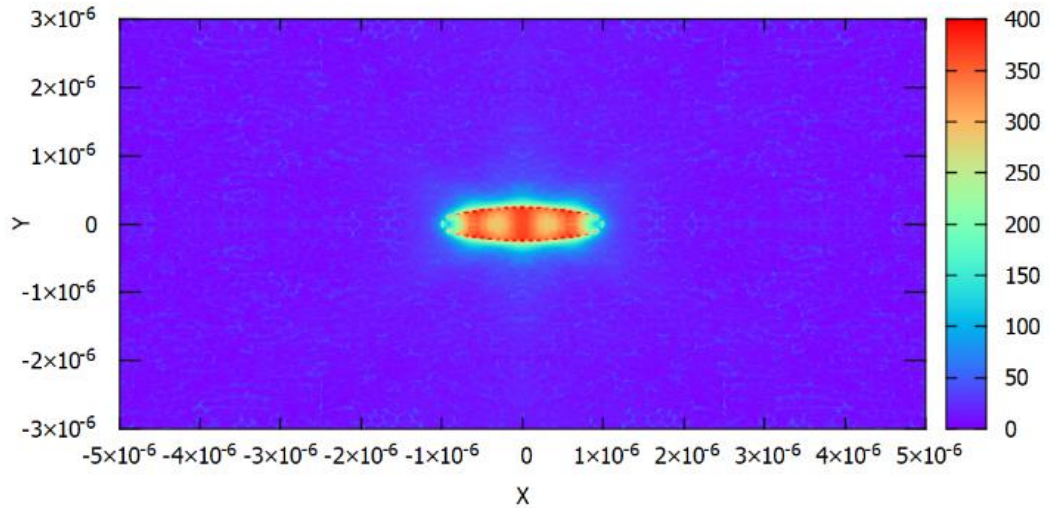


4.14b

Figure 4.14. Behavior of $|\mathbf{E}_s|$ on the plane $z = 4.99975$ mm passing through the center of gravity of the isolated mitochondrion homogeneous model (Fig. 4.14a) and simplified lamellar model (Fig. 4.14b) with x-polarized incident field.



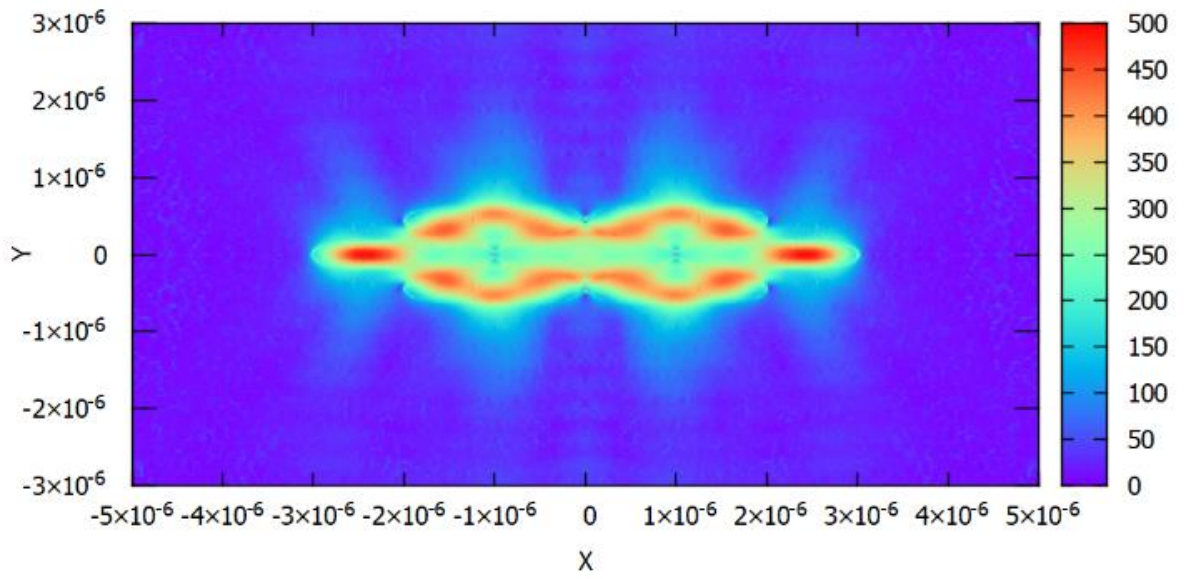
4.15a



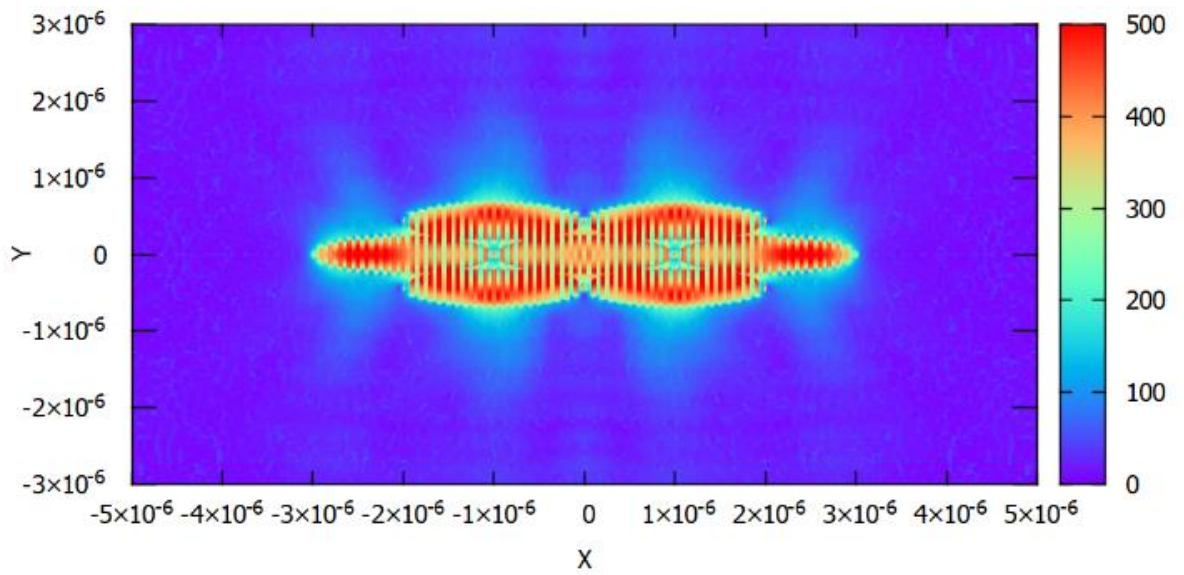
4.15b

Figure 4.15. Behavior of $|\mathbf{E}_s|$ on the plane $z = 4.99975$ mm passing through the center of gravity of the isolated mitochondrion homogeneous model (Fig. 4.15a) and simplified lamellar model (Fig. 4.15b) with y-polarized incident field.

Figures 4.14 and 4.15 show the module of the scattering field for isolated mitochondrion when the internal morphology and polarization are considered. The incident field polarization affects the scattering field and presents electric jumps on the borders, with maximum value of 500 V/m; instead, when a homogeneous model is used, are not present electric jumps, and maximum value is 500 V/m, at the borders the value varies between 250 – 300 V/m when the incident field is x-polarized. Moreover, his effect on the scattered field is less evident and similar to the homogeneous mitochondrion when the incident field is y-polarized.

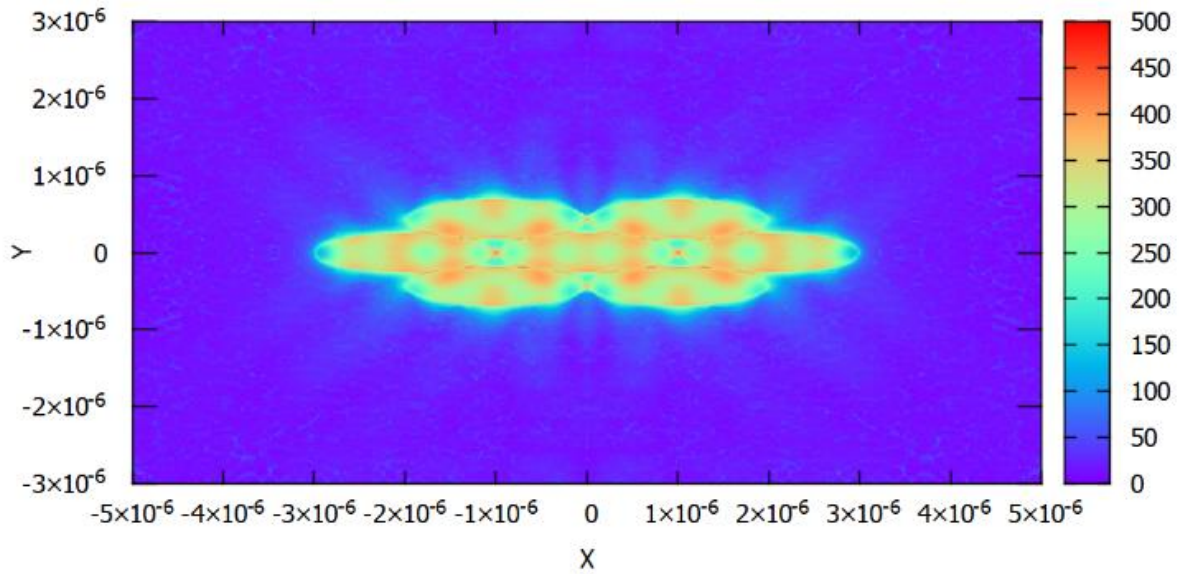


4.16a

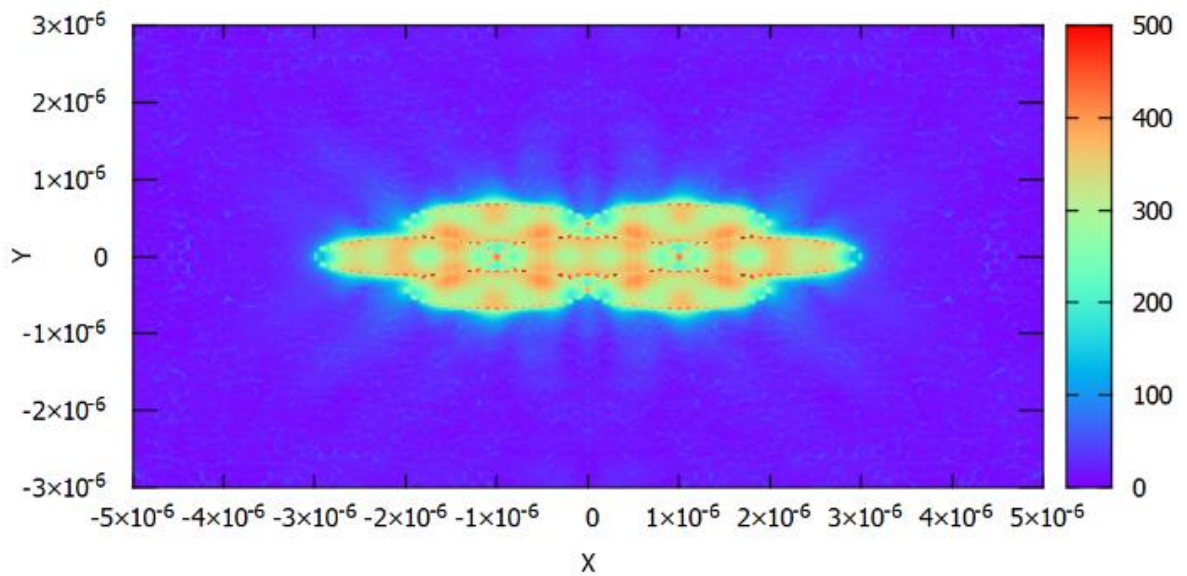


4.16b

Figure 4.16. Behavior of $|\mathbf{E}_s|$ on the plane $z = 4.99975$ mm passing through the center of gravity of the group of seven mitochondria homogeneous model (Fig. 4.16a) and simplified lamellar model (Fig. 4.16b) with x-polarized incident field.



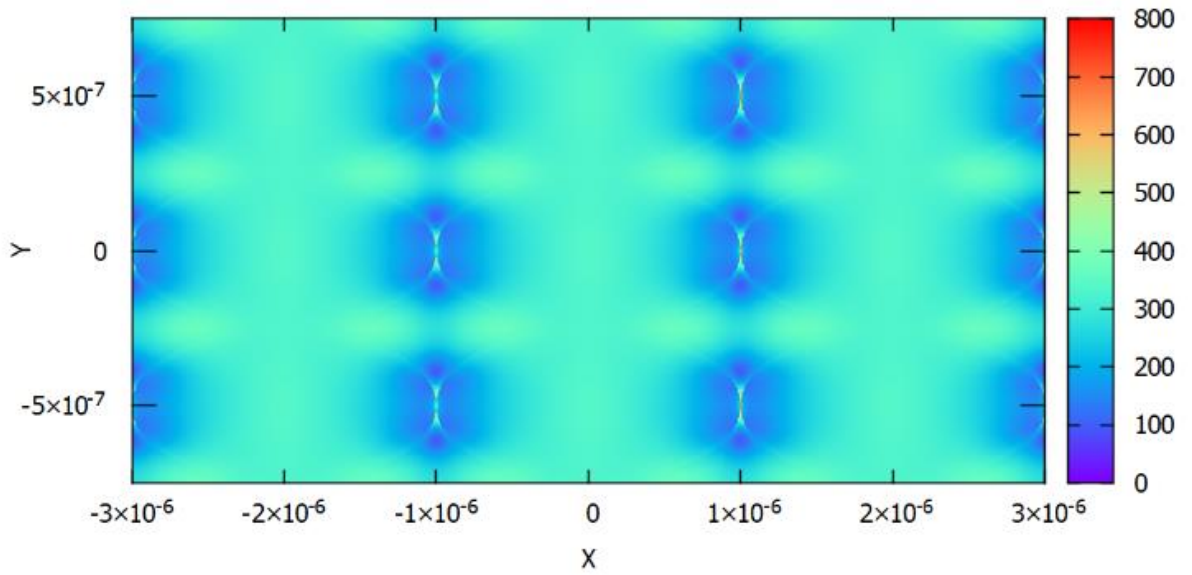
4.17a



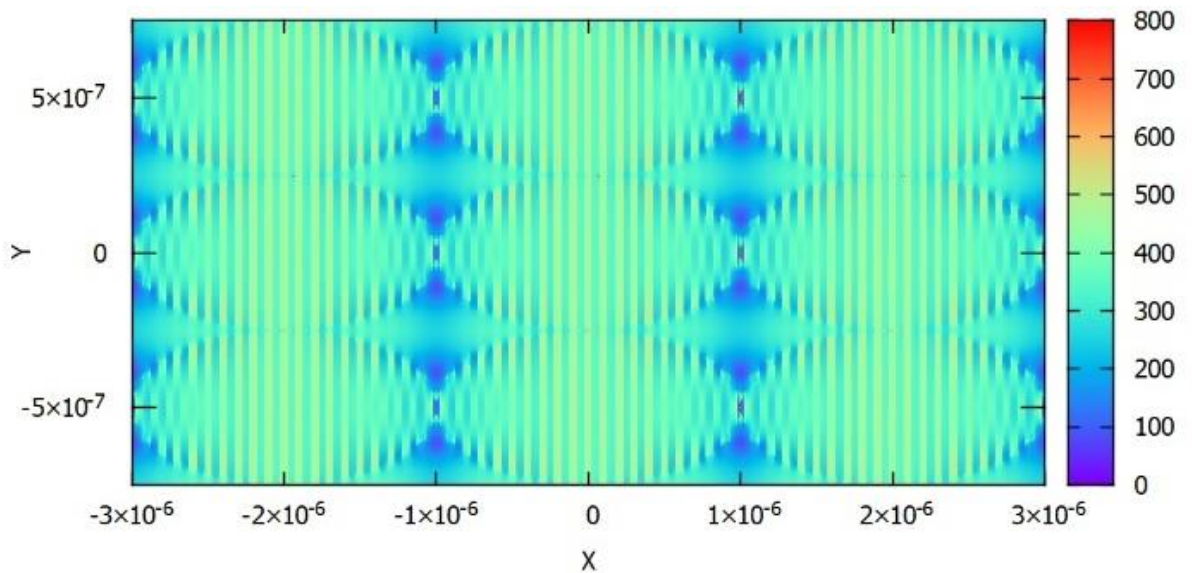
4.17b

Figure 4.17. Behavior of $|\mathbf{E}_s|$ on the plane $z = 4.99975$ mm passing through the center of gravity of the group of seven mitochondria homogeneous model and simplified lamellar model with y-polarized incident field.

Figures 4.16 and 4.17 report the scattering field module for the seven mitochondria models; in this case, the effect of neighboring with the central mitochondrion considering inhomogeneity and polarization is studied. The response when the incident field is x-polarized shows again electric jumps inside the organelles. In contrast, when the incident field is y-polarized, the response is more similar to the case of homogeneous mitochondria.



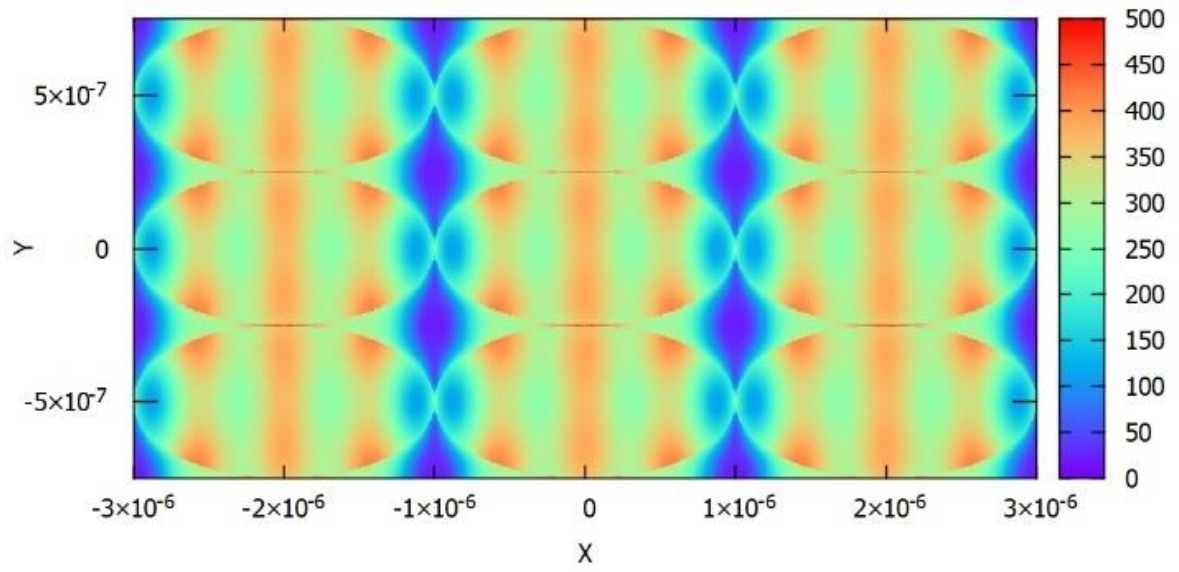
4.18a



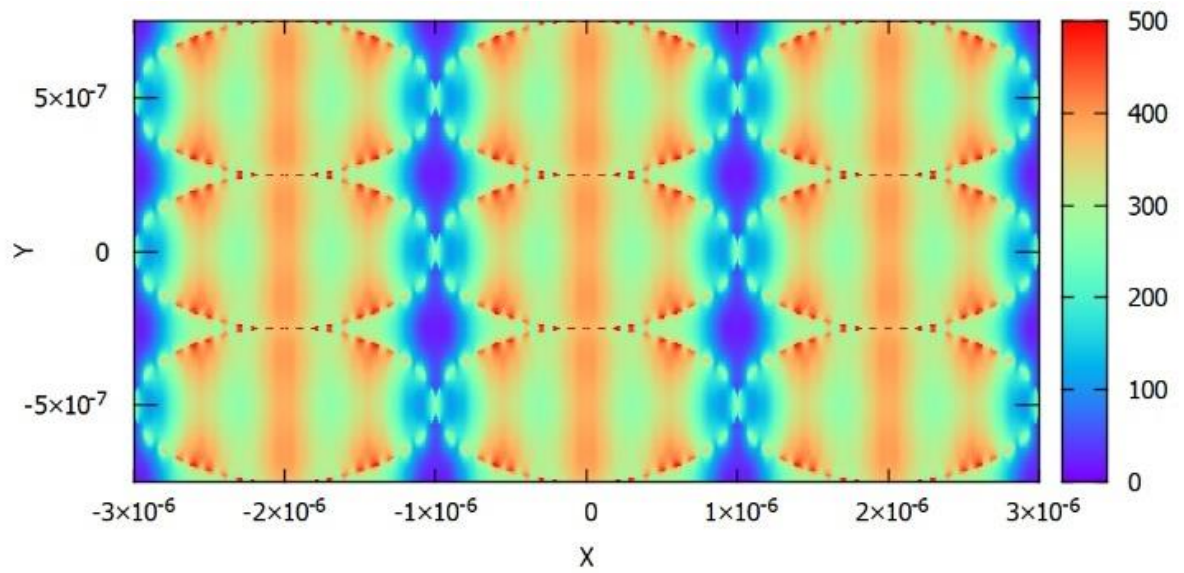
4.18b

Figure 4.18. Behavior of $|\mathbf{E}_s|$ on the plane $z = 4.99975$ mm passing through the center of gravity of the array of mitochondria homogeneous model (Fig. 4.18a) and simplified lamellar model (Fig. 4.18b) considering periodicity with x-polarized incident field.

Finally, the results of the periodic array of mitochondria are presented in Figures 4.18 and 4.19. The effect of polarization and morphology is studied. The scattering field with x-polarized incident field exhibits a similar behavior previously studies. The effect is less evident when the incident field is y-polarized and the response is similar to the homogenous model.

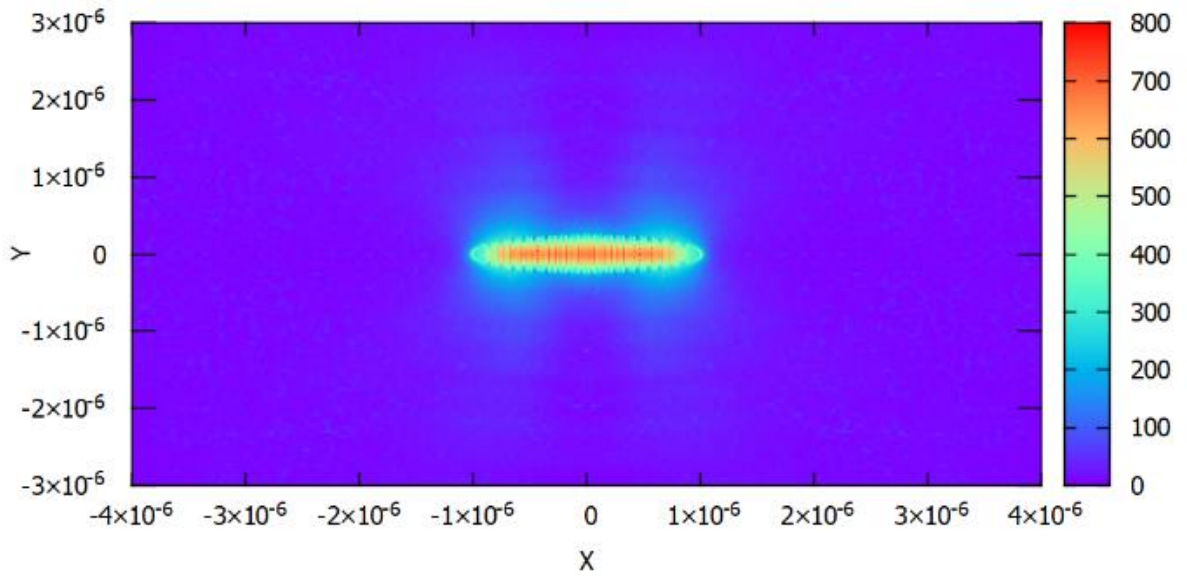


4.19a

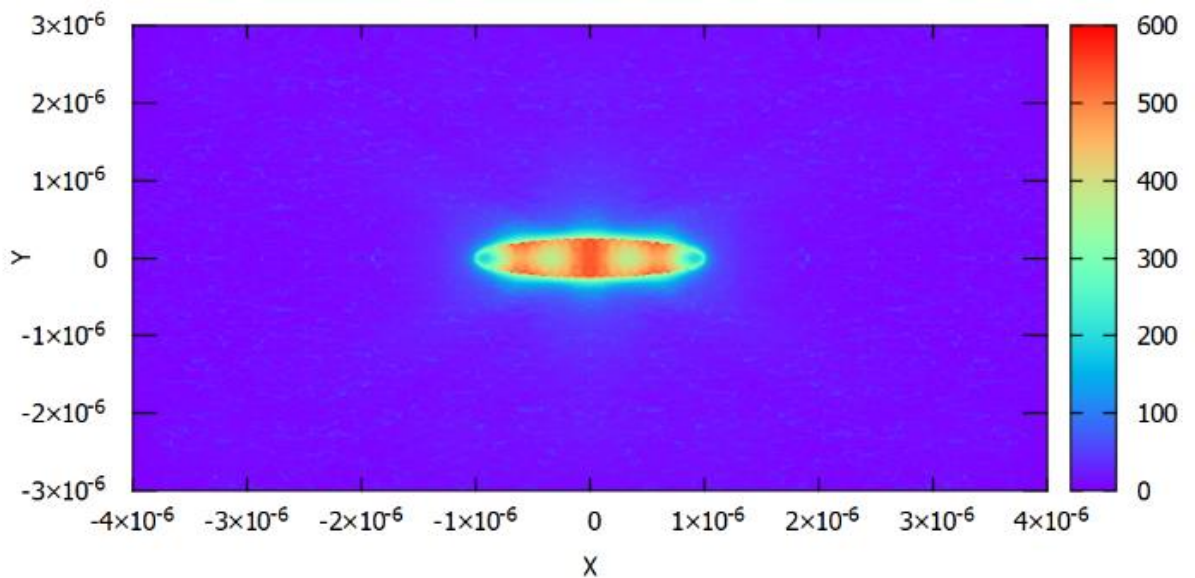


4.19b

Figure 4.19. Behavior of $|\mathbf{E}_s|$ on the plane $z = 4.99975$ mm passing through the center of gravity of the array of mitochondria homogeneous model (Fig. 4.19a) and simplified lamellar model (Fig. 4.19b) considering periodicity with y-polarized incident field.



4.20a



4.20b

Figure 4.20. Behavior of $|\mathbf{E}_s|$ on the plane $z = 4.99975$ mm passing through the center of gravity of the isolated mitochondrion tubular model for the cases of x-polarized incident field (Fig. 4.20a) and y-polarized incident field (Fig. 4.20b).

Figure 4.20 presents the behavior of the scattering field of an isolated mitochondrion corresponding to the tubular model for the different polarizations; the behavior of the

scattering field presents a similar response to the case of the lamellar model previously studied.

The interaction mechanism between irradiation light and organelles with more realistic models is studied. We have considered three-dimensional models in a well-defined experiment setup, allowing the analysis of the electromagnetic field inside the mitochondria. The models set considers several dispositions that mitochondria can assume. The internal morphology of the mitochondria is considered to a lamellar or tubular model. The results obtained in terms of the energy density and power density are very interesting: the values of E_d and P_d are very similar compared with the homogeneous models with arithmetic mean of the refractive index of the medium involved (mitochondrial matrix and intramembrane space).

The scattering field of the inhomogeneous models presents interesting behavior. When the polarization of the incident field is orthogonal to the discontinuity on the internal morphology, it reveals electric jumps, which present a maximum variation in terms of $|E_s|$ between 500-600 V/m. Therefore, when the incident field polarization is parallel to the discontinuity, the effect is less evident, and behavior is similar to the homogeneous three-dimensional model. The importance of employing inhomogeneous models of mitochondria can reveal how much energy is provided by a light source to the chromophores presents to the internal mitochondria. However, it is still difficult to know the dimension, position and quantity of these chromophores present in each organelle.

Chapter 5 Experimental measurement: study in vitro

In this chapter, the first experimental tests of an in vitro mitochondrial system are carried out. A mechanical laser handpiece holder ensures full irradiation with a small margin of error, a glass incubation chamber, a light absorbing sheet, and a plane wave laser source.



Figure 5.1. Mechanical support for laser handpiece.

5.1 Material and Methods

The laser handpiece is fixed vertically 42 mm from the surface on which the absorbent sheet is positioned; the incubation chamber with the liquid exposed to irradiation is placed above the absorbent sheet. For the saline solution a Phosphate-buffered saline (PBS) is used, which is a buffer solution (pH ~ 7.4) commonly used in biological research. It is a water-based salt solution containing disodium hydrogen phosphate, sodium chloride, and, in some formulations, potassium chloride and potassium dihydrogen phosphate. The buffer

helps to maintain a constant pH. The osmolarity and ion concentrations of the solutions match those of the human body (isotonic). PBS (phosphate-buffered saline) is a pH-adjusted blend of ultrapure-grade phosphate buffers and saline solutions. When diluted to a 1X working concentration, it contains 137 mM NaCl, 2.7 mM KCl, 8 mM Na₂HPO₄, and 2 mM KH₂PO₄. Each 10X PBS solution is ready to use upon dilution to the desired concentration.

The company **Garda Laser ENEA** manufactures a laser with wavelength operation of 810 nm, which is used in many medical fields. The dimensions of the instrument are 270 mm x 195 mm x 270 mm, max frequency 30000 Hz, mode continuous/pulsed/single pulse, is used GaAlAs diode laser. The wavelength operation is 810nm +/- 10nm, with a pointer light of 635nm +/- 10nm (1mW). Maximum power in continuous wave is 3 W, 7 W, and 15 W.



Figure 5.2. Laser fixed with mechanical support and manipule connected at source and impinging red light for alignment and light absorbed sheet.

Light absorption material absorbs laser light in the infrared band. The company **Acktar Advanced coating** manufactures this material and is chosen this type: “Metal velvet Light absorbed panel”. Present extremely low reflectance (less than 1% in infrared band), sheet

dimension is 20 cm x 30 cm, thickness is 120 μm , with certificate RoHS, REACH, ISO 9001:2015, AS9100.

The incubation chamber is manufactured by the company **Spaziani Srl.** and is made of borosilicate glass with dimensions outer diameter of 1.5mm, an outer height of 8mm, and a thickness of 1.2mm. The company **Thorlabs** manufacture this power meter. It is a wireless Power Meter with an attached Thermal Sensor; Optical Power Range is 10 mW to 70 W; the wavelength range operation is 0.19 to 20000 nm, the optical power resolution is 1 mW, the laser pointer, always present during the exposure, contributes an additional five mW., the power linearity is $\pm 1\%$ and the operating temperature is 0 to 50 degree.



Figure 5.3. Wireless power meter used for verifying stability of laser source.

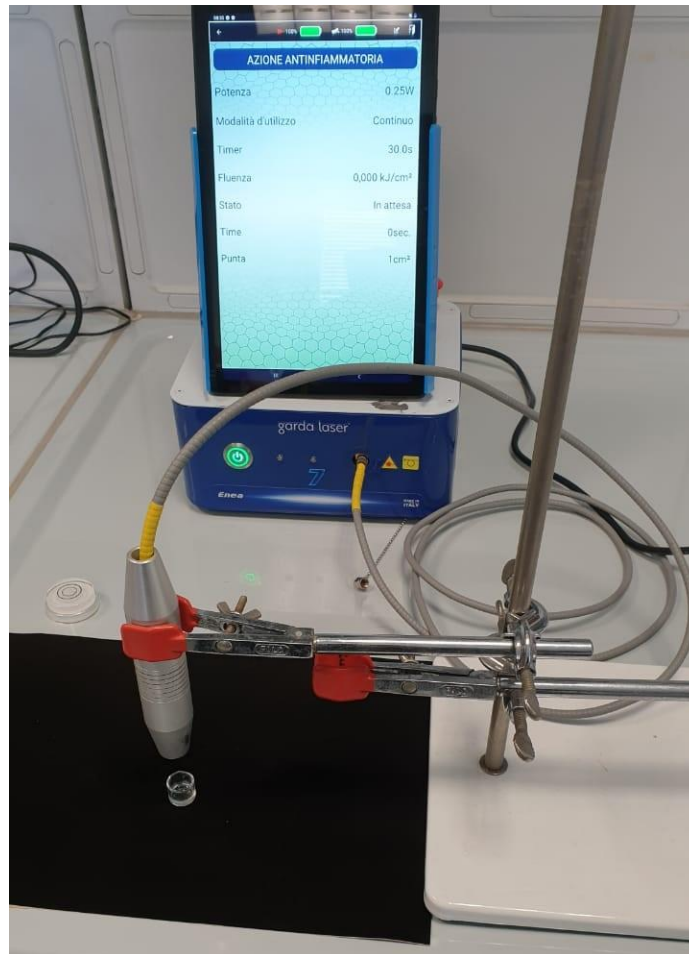


Figure 5.4. Experimental setup before irradiation of laser. Absorption light sheet is posted below of incubation chamber.

Before starting the experiments, we verified the laser stability, and we used the wireless power meter. We made several tests at the distance of 42mm. In the Figure 5.5 is presented the histogram of the laser stability by using different level of power irradiated. Every measurement has been repeated three times. The maximum measured relative standard deviation is 1.52%.

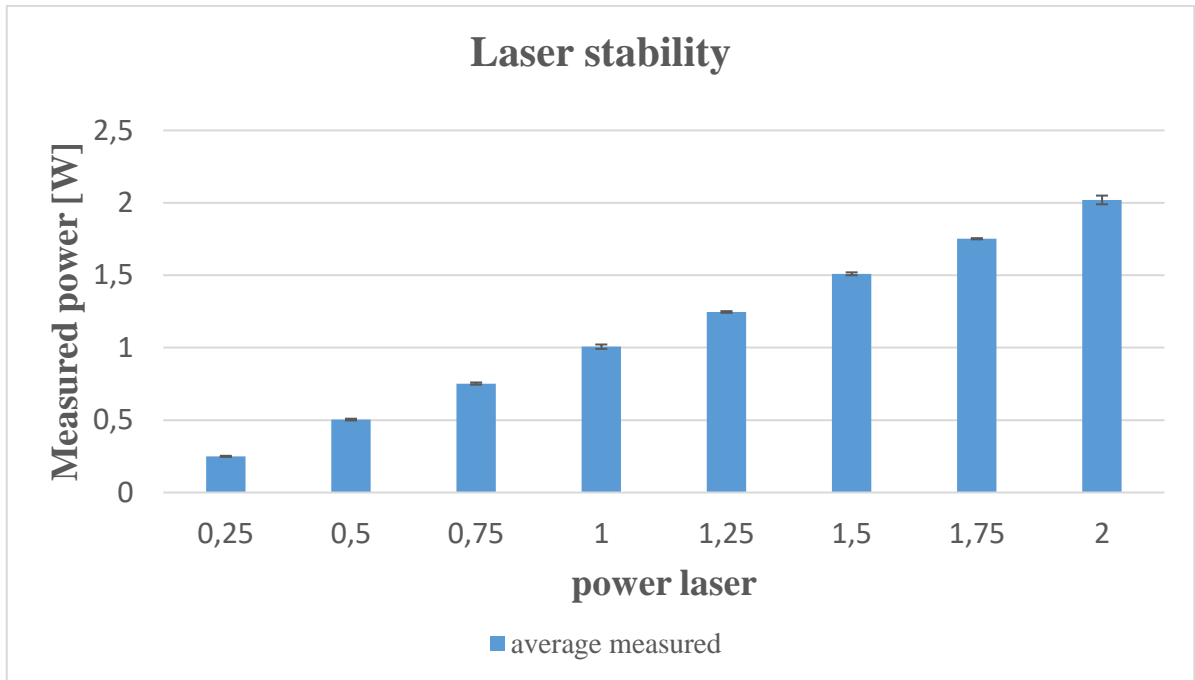


Figure 5.5. Histogram of analyze laser stability of power.



Figure 5.6. Test with wireless power meter for verify reliability of laser

The PBS solution with mitochondria contains a volume of 300 microliters. The circular section of the incubation chamber is 1.25cm^2 , the calculation of the height of the composite is manageable using the equation $\text{height} = \text{volume}/\text{area}$. The solution

prepared contain 1/64 of bovine liver mitochondria and 63/64 of saline solution. For $300 \mu\text{l} = 1.25 \text{ cm}^2 * \text{h}$. the thickness value of the composite is 2.3625 mm of PBS, and 37.5 μm contain sample of mitochondria. The absorbent light sheet is positioned below the incubation chamber.



Figure 5.7. Incubation chamber with mitochondria and PBS.



Figure 5.8. Exposition of incubation chamber with composition of mitochondria with PBS at 810 nm.

5.2 Evaluation of Mitochondrial ATP Synthesis.

The evaluation of ATP production requires chemical techniques, the mitochondrial enriched fraction was dissolved in a solution containing 100 mM Tris-HCl pH 7.4, 100 mM KCl, 1 mM EGTA, 2.5 mM EDTA, 5 mM MgCl₂, 0.2 mM di(adenosine-5') pentaphosphate, 0.6 mM ouabain, ampicillin (25 µg/ml), 5 mM KH₂PO₄, and 5 mM pyruvate+2.5 mM malate, used as respiratory substrates. ATP synthesis started after the addition of 0.1 mM ADP and was monitored for 1 minute, in a luminometer (**GloMax 20/20, Promega**) by the luciferin/- luciferase chemiluminescent method.



Figure 5.9. Luminometer GloMax® 20/20 used for detecting the ATP production for “in vitro” experiments.

Before each experiment, we wait for 120 s to allow time for the mitochondria to settle at the bottom of the incubation chamber. Each experiment is repeated three times. For power density equal to 0.25 Wcm^{-2} , does not have considerable effects using the exposure time of 30 s, 60 s and 120 s, equivalent for dosage of 7.5 Jcm^{-2} , 15 Jcm^{-2} and 30 Jcm^{-2} . For power density equal to 0.5 Wcm^{-2} the first effects of oxygen production appear, in comparison with the not irradiated “control”. For power density equal to 1 Wcm^{-2} the

effects are more evident for dosage of 30 Jcm^{-2} , 60 Jcm^{-2} and 120 Jcm^{-2} (exposure time 30, 60 and 120 seconds).

This campaign of experimental measurements shows that irradiating in our system (made up of the laser, PBS solution, sample of mitochondria, incubation chamber, and the light absorption sheet), the oxygen production due to the excitation of the chromophores present inside the mitochondria is verified. The results of this experiment are being processed and will be presented in a future contribution. The preliminary result obtained is presented below: in figure 5.10 it is measured the effect on the luminescence produced by mitochondria in different dosage of time and power. The luminescence is measured in RLU (Relative Luminescence Unit).

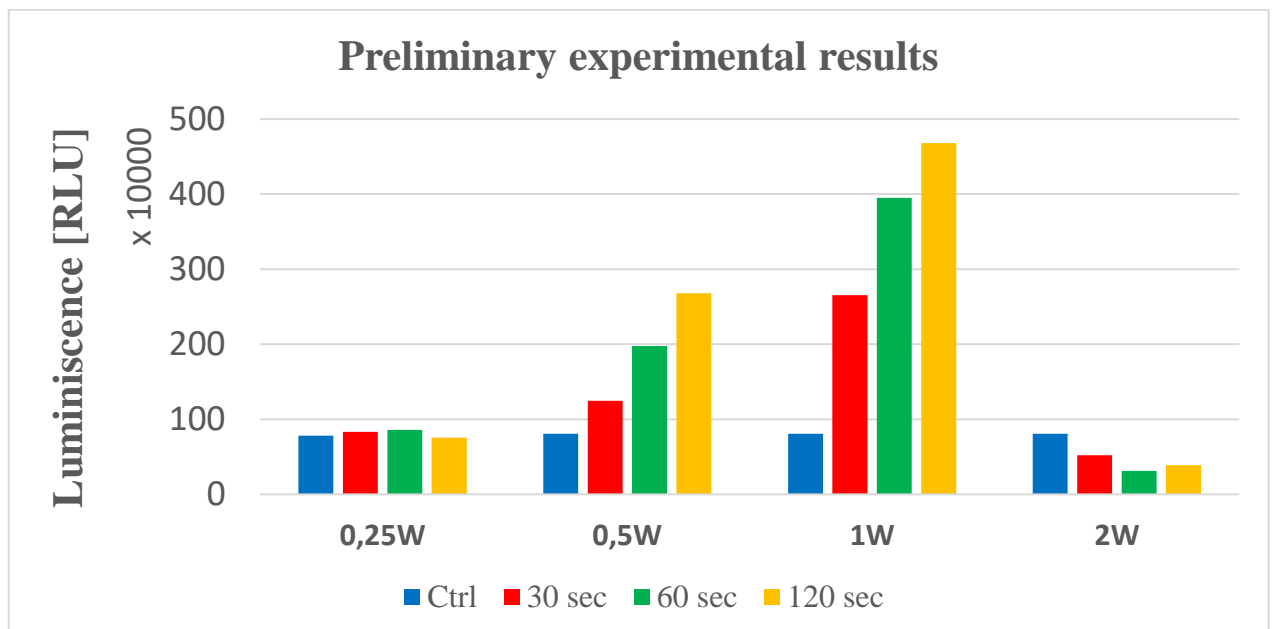


Figure 5.10. Preliminary experimental results of measurement oxygen production using luminometer instrument for different power levels and exposure time

Chapter 6 Electromagnetic simulations of problems involving moving objects

In this work I deal with computational electromagnetics problems mainly working on the low-level laser therapy. A part of this activity was dedicated to the study of problems involving moving objects. In this chapter the activity carried out on this topic will be presented.

Albert Einstein developed the theory of the electrodynamics of moving bodies in the framework of relativity in his revolutionary paper published in 1905 [121], building upon the work of Maxwell and other scientists before him. An excellent introduction to the electrodynamics of moving bodies is given in [122]. It is well-known that Maxwell's equations remain unaltered in all inertial frames of reference. The electric field, magnetic field, current density, and charge density get transformed according to relativistic relationships. The constitutive relations and material boundary conditions have to be transformed from the rest frame of the body to the laboratory frame. Even if it is isotropic in its rest frame, a moving media will be perceived as bianisotropic in laboratory frame [123]. The material boundary conditions are also changed unless the velocity is tangential to the boundary. Further, there is a doppler shift due to which the frequency of electromagnetic fields from moving media gets modified [122]. In the following equations the relationship between \mathbf{D} and \mathbf{H} with respect to \mathbf{E} and \mathbf{B} are presented [111], [124].

$$\mathbf{D} = \frac{1}{c_0} \mathbf{P}\mathbf{E} + \mathbf{L}\mathbf{B} \quad (54)$$

$$\mathbf{H} = \mathbf{M}\mathbf{E} + c_0 \mathbf{Q}\mathbf{B} \quad (55)$$

The electromagnetic problems involving moving objects are important in various applications, for example, astrophysics, nuclear and plasma physics, and engineering. In continuation, we will introduce a new research topic: electromagnetic scattering for media in motion involved in several important electromagnetic problems [122]. In most of these

applications, the solutions must be found using the natural space-time framework defined by the theory of relativity [125],[122]. However, in some cases, the movement takes place in such a way that it is still possible to work in the frequency domain, for example, in the presence of moving media with stationary boundaries [123], [126].

6.1 State of the art related to electromagnetic scattering for moving object

A fundamental class of the problems involves rotating axisymmetric objects, which can be studied using three-dimensional time-harmonic models [127], [128]. A set of sufficient conditions for well-posedness and the finite element approximability of the forward problem of calculating the fields were established in [112]. In some of the indicated problems, the rotating velocity is unknown, and it is of particular interest to be able to detect it using inverse scattering procedures. However, to the authors' knowledge, there are no results on detecting the rotating velocity from scattered field data.

In [129], the authors developed a two-step algorithm for reconstructing the velocity of two-dimensional problems involving axially moving cylinders when the speeds are not too large. The idea was because for a particular polarization of incident field (TM or TE), one of the polarizations (cross-polarized component) is absent in the scattered field when there is no motion and varies linearly with the velocity for low speeds. In addition, the other polarization of the scattered field (co-polarized component) is affected only slightly (second-order effect) due to motion. This procedure allows the algorithm to use the co-polarized component of the scattered field used in the first step to reconstruct the media's dielectric and geometric properties, ignoring motion effects. The values deduced in the first step were then used in the second step to finding the axial speed from the cross-polarized component. The authors demonstrated the efficiency of the two-step procedure over directly using the whole field in a single step to reconstruct all the unknowns simultaneously. The better performance of the two-step procedure stems from the complexity of the inversion algorithm increasing much faster than linear with the number of unknowns, and hence the solution using two more straightforward steps is much more efficient than solving the whole problem in a single step. Further, in [130], the authors studied the limitations of the reconstruction algorithm when the measured data are noisy and the sensors have limited capabilities.

In general, in three-dimensional problems, the effects of bianisotropic are more complex [111], [122], and it could be difficult or even impossible to isolate field components to provide a clear indication of the velocity field. However, the first numerical results for the fields in the presence of motion were presented. They indicate that the effect due to motion is insignificant even for relatively high values of rotating speeds. Moreover, for higher velocities, the reconstruction of the geometric and dielectric unknowns by ignoring the motion can be even better than using the general algorithm since having a reduced number of unknowns not only speeds up the solution process but also gives improved precision. Therefore, in this case, we propose to define a cost function using all the components of the fields in the first step, which is used to reconstruct the geometric and dielectric properties assuming that the media are under rest. The values from the first step are used to evaluate the rotation speed in the second step. For low rotating speed, the numerical results demonstrate that such an approach is practical and fast compared to inverting all the unknowns in a single step. The numerical results are obtained for a test problem involving a homogeneous rotating sphere that admits an analytic solution [121]. The robustness of the results is demonstrated by examining the effect of different noise levels in the input data. The results are also demonstrated for measurement scenarios with amplitude and phase data from near-field or far-field. The effect of using simple sensors with only amplitude data is also studied. Within the range of rotating speeds considered, the reconstruction can obtain accurate values even for significant noise levels if the speed is large enough. In the case of low rotating speeds, the inversion can give correct values if the noise levels can be reduced. Finally, to show the generality of the approach, results are provided for a test case involving a rotating torus. For this case, the forward solver employed uses the finite element method without an analytic solver.

6.2 Inversion procedure for rotating media

The reconstruction of velocity profiles of moving objects using electromagnetic inverse scattering techniques is an important research topic. Such techniques have been exploited for axially moving cylinders in [129], [130]. The reconstruction of the rotation speeds of axisymmetric media has been studied for many years; there are numerous applications, such as tachymetry, applied in astronomy [122], [127], [128]. The unknown parameters of

the inverse scattering problem may be represented by the algebraic vector $\mathbf{u} = \mathbf{u}_g, \mathbf{u}_d, \mathbf{u}_v \in \mathbb{R}^{I+J+K}$, where $\mathbf{u}_g \in \mathbb{R}^I$, $\mathbf{u}_d \in \mathbb{R}^J$ and $\mathbf{u}_v \in \mathbb{R}^K$ are respectively the components having the geometry, dielectric and velocity parameters.

A set of S plane wave sources illuminates the scatterer; the parameter $s = 1, \dots, S$ denotes the position of the source. The electric and magnetic fields are measured using M sensors; the parameter "m" indicates the actual position of the sensor, which have a range between 1 to M . The measured electric and magnetic fields are denoted by $\mathbf{E}^{\text{meas}}(s, m, \mathbf{u})$ and $\mathbf{H}^{\text{meas}}(s, m, \mathbf{u})$. For a trial solution $\mathbf{u}^{\text{trial}} = (\mathbf{u}_g^{\text{trial}}, \mathbf{u}_d^{\text{trial}}, \mathbf{u}_v^{\text{trial}}) \in \mathbb{R}^{I+J+K}$, we assume to have a forward scattering procedure (fsp), either semi-analytic or numerical, that enables us to calculate the fields $\mathbf{E}^{\text{fsp}}(s, m, \mathbf{u}^{\text{trial}})$ and $\mathbf{H}^{\text{fsp}}(s, m, \mathbf{u}^{\text{trial}})$.

The above quantities can be used to define the following cost function $\text{CF}(\mathbf{u}, \mathbf{u}^{\text{trial}})$, which is to be minimized using an optimization algorithm to get the best estimate of unknown parameters:

$$\begin{aligned} \text{CF}(\mathbf{u}, \mathbf{u}^{\text{trial}}) = & \frac{\sum_{s=1}^S \sum_{m=1}^M \|\mathbf{E}^{\text{fsp}}(s, m, \mathbf{u}^{\text{trial}}) - \mathbf{E}^{\text{meas}}(s, m, \mathbf{u})\|^2}{\sum_{s=1}^S \sum_{m=1}^M \|\mathbf{E}^{\text{meas}}(s, m, \mathbf{u})\|^2} \\ & + \frac{\sum_{s=1}^S \sum_{m=1}^M \|\mathbf{H}^{\text{fsp}}(s, m, \mathbf{u}^{\text{trial}}) - \mathbf{H}^{\text{meas}}(s, m, \mathbf{u})\|^2}{\sum_{s=1}^S \sum_{m=1}^M \|\mathbf{H}^{\text{meas}}(s, m, \mathbf{u})\|^2} \end{aligned} \quad (56)$$

The norms are just Euclidean norms for three-dimensional complex vectors. The above step provides the general way to obtain the parameters using the inverse scattering algorithm. However, if the rotating speed of object is low enough, we may adopt a two-step procedure for the inversion. Since the contribution to the fields due to the rotation will be low, the media may be assumed to be at rest for reconstructing geometric and dielectric data. Thus, the cost function for the first step will be as follows:

$$\begin{aligned} \text{CF}_1(\mathbf{u}, \mathbf{u}_1^{\text{trial}}) = & \frac{\sum_{s=1}^S \sum_{m=1}^M \|\mathbf{E}^{\text{fsp,rest}}(s, m, \mathbf{u}_1^{\text{trial}}) - \mathbf{E}^{\text{meas}}(s, m, \mathbf{u})\|^2}{\sum_{s=1}^S \sum_{m=1}^M \|\mathbf{E}^{\text{meas}}(s, m, \mathbf{u})\|^2} \\ & + \frac{\sum_{s=1}^S \sum_{m=1}^M \|\mathbf{H}^{\text{fsp,rest}}(s, m, \mathbf{u}_1^{\text{trial}}) - \mathbf{H}^{\text{meas}}(s, m, \mathbf{u})\|^2}{\sum_{s=1}^S \sum_{m=1}^M \|\mathbf{H}^{\text{meas}}(s, m, \mathbf{u})\|^2} \end{aligned} \quad (57)$$

Here the vector $\mathbf{u}_1^{\text{trial}} = (\mathbf{u}_g^{\text{trial}}, \mathbf{u}_d^{\text{trial}})$ contains the geometric and dielectric unknowns and the fields are calculated with analytic or numerical solvers for the rest case.

In the second step, we estimate the velocity by optimizing the following cost function that uses a forward scattering procedure for the rotating media along with the approximate geometric and dielectric data \mathbf{u}_1^{as} obtained from the previous step:

$$\begin{aligned} \text{CF}_2(\mathbf{u}, \mathbf{u}_1^{\text{as}}, \mathbf{u}_1^{\text{trial}}) &= \frac{\sum_{s=1}^S \sum_{m=1}^M \|\mathbf{E}^{\text{fsp,rest}}(s, m, \mathbf{u}_1^{\text{trial}}) - \mathbf{E}^{\text{meas}}(s, m, \mathbf{u})\|^2}{\sum_{s=1}^S \sum_{m=1}^M \|\mathbf{E}^{\text{meas}}(s, m, \mathbf{u})\|^2} \\ &+ \frac{\sum_{s=1}^S \sum_{m=1}^M \|\mathbf{H}^{\text{fsp,rest}}(s, m, \mathbf{u}_1^{\text{trial}}) - \mathbf{H}^{\text{meas}}(s, m, \mathbf{u})\|^2}{\sum_{s=1}^S \sum_{m=1}^M \|\mathbf{H}^{\text{meas}}(s, m, \mathbf{u})\|^2} \end{aligned} \quad (58)$$

Both these steps are much simpler than using the cost function in (56). The forward scattering procedure is much simpler for the first step due to the lack of motion. The optimization is also simpler because the unknowns related to the velocity are not present. The second step is simpler because it requires the optimization for only the velocity parameters. Since the complexity of the optimization increases much faster than linear, the two steps combined can be more efficient than doing the direct optimization of the full cost function.

For the optimization, is adopted the differential evolution (DE) algorithm [131]. DE is a metaheuristic algorithm that starts with a random initial population of size N_p in the search space and keeps on improving the solution by introducing stochastic variations to the candidate solutions until a termination criterion is satisfied. Here is the condition used for termination is either the maximum number of iterations, N_{lim} , is reached, or the cost function does not improve more than by a factor of f_{conv} in N_{conv} consecutive iterations.

6.3 Numerical results

The simulations are performed on an Intel i7-8565U, 1.8GHz, 4-core machine with 16 GB RAM. For the proposed two-step algorithm, the first step involves the traditional problem of recreating the geometric and dielectric unknowns for stationary objects and is already

widely studied in the literature [132]. On the other hand, the second step of the algorithm for recreating the rotating speeds is new and therefore is analyzed here more carefully. In 6.3.1 the proposed two-step procedure is compared to the general algorithm by solving a test case that has a semi-analytic solution. For this, a homogeneous rotating sphere is considered. The near-field measurement on a full circle around the scatterer is used for this. The effect of different noise levels is also studied. The same test case is used in 6.3.2 and 6.3.3 to study the accuracy of the two-step procedure with simpler sensors and far-field data, respectively. In particular, in 6.3.2 is discussed the effect of having scattered field data with the measurement restricted to be on an arc in the backscattered direction and when only the amplitude data is available. In 6.3.3 are examined results for the far-field and the effect of uncertainty in knowing the axis of rotation of the scatterer. In 6.3.4 is described the effect of changing the dielectric parameter on the algorithm's accuracy. Finally, a different test case is considered for which no analytic solution is available in 6.3.5. A homogeneous rotating torus is studied for this, and a numerical forward solver is exploited in the solution procedure.

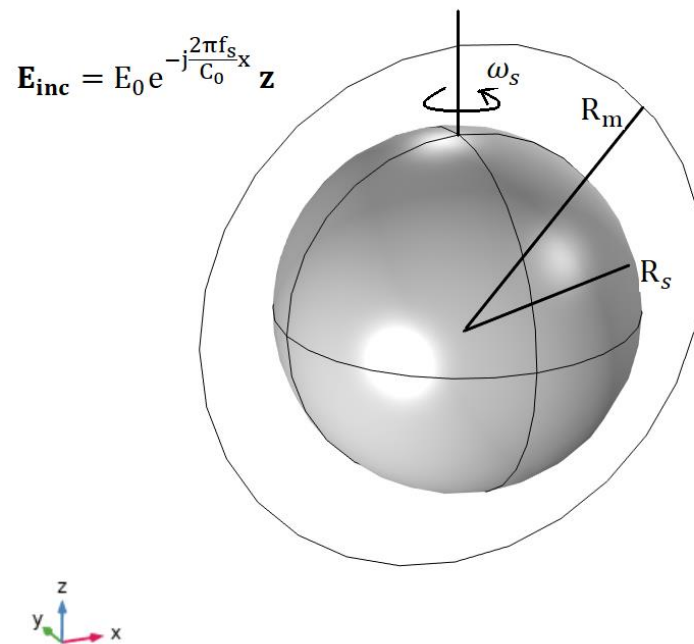


Figure 6.1. The geometry of the case involves a homogeneous spherical scatterer of radius R_s rotating the z-axis with angular velocity ω_s . The electric field incident is an electromagnetic plane wave with frequency f_s propagated along the x-axis and polarized along the z-axis. The measurement points are posted around the sphere on a circle of radius R_m .

6.3.1 Comparison of the two-step procedure with the general algorithm

We are now considering a simple configuration of a homogeneous sphere rotating at a uniform angular velocity. A first-order semi-analytic solution is available in the literature for such a problem [127]. The performance of the general algorithm and the two-step procedure for reconstructing the unknown parameters are analyzed.

A sphere of radius $R_s = 1$ m is considered, rotating around the z-axis, at angular velocity ω_s rad/s. It is illuminated by a single plane wave ($S=1$) incident propagated along the x-axis with a frequency of $f_s = 50$ MHz. The incident electric field is polarized along the z-axis. The geometry is show in Figure 6.1. The rotation speed is normalized with $\beta = \omega_s R_s / C_0$, where C_0 is the speed of light in vacuum. The results are tested for $\epsilon_r = 8$ and $\beta \in \{8 \times 10^{-5}, 8 \times 10^{-4}, 8 \times 10^{-3}\}$ and are calculated at $M=200$ points uniformly distributed on a circle on xz plane of radius $R_m = 1.5$ m from the center of the scatterer. The electric and magnetic fields thus obtained are corrupted with Gaussian noise of specific signal-to-noise ratio (SNR). It is considered SNR in dB levels $\{20,30,40,50,60\}$ which we added to each component of the electric and magnetic fields.

The inversion is carried out with the DE algorithm with a population size of $N_p = 10$. The parameters related to the termination of the algorithm are set as $N_{lim} = 100$, $f_{conv} = 0.01$ and $N_{conv} = 10$. The range over which the solution is searched for $\epsilon_r \in [1,20]$ and $\beta \in [-1,1]$. In Table 6.1 summarizes the results for the cases SNR = 40 dB for the three values of β indicated above. The general algorithm tries to find both the unknowns together using the DE algorithm with the cost function in (56) and with $u = (\epsilon_r, \beta)$. As described in the previous section, the two-step procedure first tries to find the solution for $u_1 = \epsilon_r$ by minimizing the cost function indicated in equation (57) by ignoring any media rotation. The approximate solution thus found in the first step is then used in the second step to solve for the value of $u_2 = \beta$ by minimizing the cost function indicated in equation (58).

Rotation speed	Algorithm	Mean relative error ϵ_r	Mean relative error β	Mean minimum cost	Mean time of simulation [s]
$\beta = 8 \times 10^{-5}$	General Algorithm	3.05×10^{-2}	1.49×10^{-2}	1.00×10^{-1}	3419.5
$\beta = 8 \times 10^{-5}$	Two-step procedure	1.75×10^{-2}	3.43×10^{-1}	3.16×10^{-4}	1607.0
$\beta = 8 \times 10^{-4}$	General Algorithm	1.79×10^{-4}	1.34×10^{-1}	3.16×10^{-4}	6462.8
$\beta = 8 \times 10^{-4}$	Two-step procedure	3.74×10^{-5}	2.54×10^{-2}	3.98×10^{-4}	1332.0
$\beta = 8 \times 10^{-3}$	General Algorithm	1.39×10^{-4}	4.67×10^{-3}	3.14×10^{-4}	7398.0
$\beta = 8 \times 10^{-3}$	Two-step procedure	1.12×10^{-4}	2.66×10^{-3}	9.62×10^{-3}	1511.1

Table 6.1. Comparison of the results obtained by the general algorithm and those of the two-step procedure for the reconstruction of the unknown parameters ϵ_r and β , of a rotating sphere. The data is for a SNR level of 40 dB in each component of the measured data. The sphere is of radius $R_s = 1$ m, the illuminating field has a frequency of $f_s = 50$ MHz and a direction of propagation perpendicular to the sphere's axis of rotation. The actual value of $\epsilon_r = 8$.

The results presented an averaged over four test runs for each configuration. As can be seen from the table, for SNR = 40 dB, both the algorithms give good response when $\beta = 8 \times 10^{-3}$. The relative errors in ϵ_r are 0.0139% and 0.0112% for the general algorithm and the two-step procedure, respectively. The corresponding relative errors of β are 0.467% and 0.266%. However, the two-step procedure can find the solution in 1h 15m whereas the general algorithm takes 2h 3m to find the solution. The performance of the two-step procedure improves relative to the general procedure when the rotating speeds are lower. For $\beta = 8 \times 10^{-4}$, the two-step procedure obtains the solutions for ϵ_r and β with relative errors of 0.00374% and 2.54% respectively. The relative errors from the general algorithm are 0.0179% and 13.4%. Finally, when $\beta = 8 \times 10^{-5}$, the general algorithm gives

completely inaccurate result for β while the two-step procedure gives a value with 34.3% relative error.

The two-step procedure provides more accuracy solutions than the general algorithm when the rotating speed is lower. The time of simulation is less for the two-step procedure than the general algorithm. The solutions are reliable for lower values of speed as long as the noise level is not too high. It can be noted that the two-step procedure is proposed assuming that the speeds are not too high, the numerical results show that it is applicable even for the highest of the velocity values that can be of practical relevance.

To get an indication of how larger values of rotating speed can affect the accuracy of the two-step algorithm, the error values from both the algorithms are provided in Figure 6.2 for $\beta = \{4 \times 10^{-3}, 8 \times 10^{-3}, 16 \times 10^{-3}, 32 \times 10^{-3}, 64 \times 10^{-3}, 128 \times 10^{-3}\}$. The results are applied for homogeneous medium of $\epsilon_r = 8$, the two-step algorithm performs better than the general algorithm for values of $\beta < 2.75 \times 10^{-2}$. Although the exact values can change with the dielectric medium, the results verify that the two-step algorithm provides accurate results for all speeds that can be of practical interest.

In order to understand the effect of noise for the two-step procedure in the diffuse field data, we give the effect of SNR values on the error in the reconstructed speed is obtained using the two-step procedure. Figure 6.3 show the mean relative error in the recovery value of β is plotted the SNR levels in dB. Are plotted for $\beta \in \{8 \times 10^{-5}, 8 \times 10^{-4}, 8 \times 10^{-3}\}$. For $\beta = 8 \times 10^{-3}$, the relative error is 0.032% when SNR=60 dB and increases to 8.2% when SNR=20 dB. For $\beta = 8 \times 10^{-4}$, the mean relative error the values are 0.35% for SNR=60 dB and 27% for SNR=20 dB. Finally, for $\beta = 8 \times 10^{-5}$, the relative means of the errors are 4.47% for SNR= 60 dB and 493.6% for SNR=20dB. Is noted that for small values of β the effects of movement on the electromagnetic field are small and the noise affect the field more than motion. In these cases, an accurate field measurement is required.

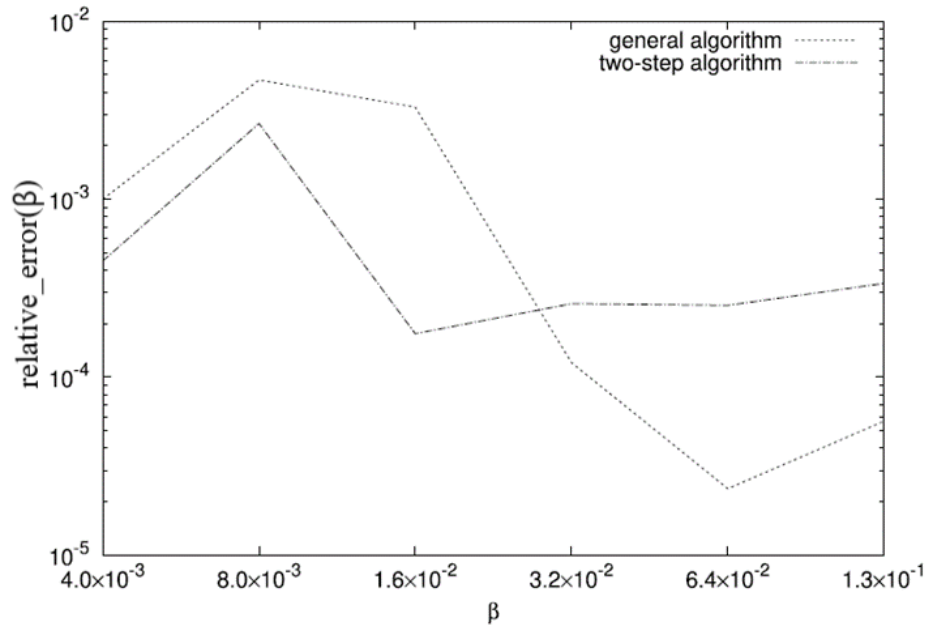


Figure 6.2. The mean relative error in the reconstructed value of β vs β for the rotating sphere. The result obtained from the two-step algorithm is compared with that obtained using the general algorithm. The measured fields are corrupted with SNR level of 40 dB.

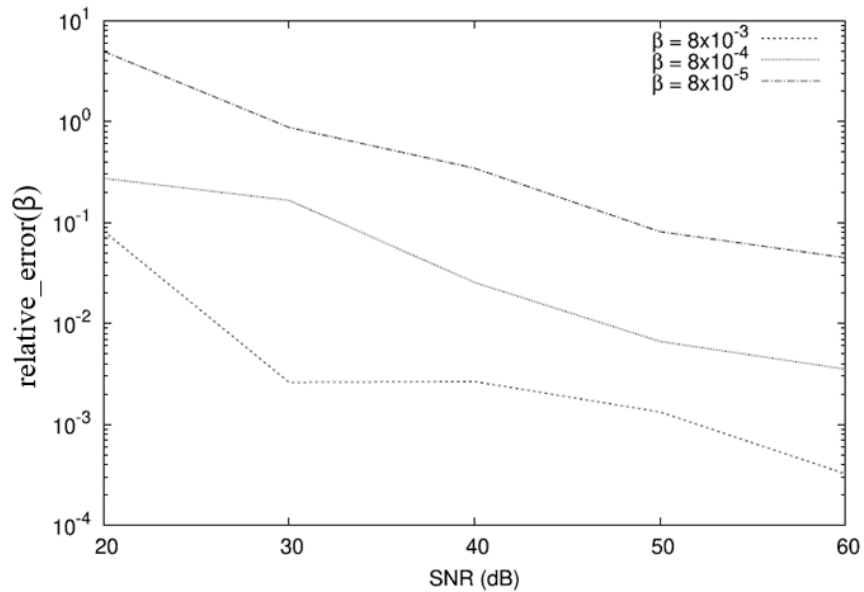


Figure 6.3. The relative error of recovery value of β vs SNR levels in dB for the rotating sphere.

6.3.2 Efficiency of two-step procedure

The previous subsection examined the efficacy of the reconstruction algorithm when the measurement of the complex fields is available on the full circle outside the scatterer.

Now, we are going to examine the performance of the two-step algorithm under certain limitations introduced by the sensors. First, is studied the effect of limiting the measurement points to only a small portion along the backscattering direction. After that, is studied the effect of having only the amplitude data for the electromagnetic fields which can allow us to use much simpler sensors. The results obtained by considering only the measurement points along the backscattered direction are provided in Figure 6.2. For this, we used the portion of measurement data that belongs to an arc limited of 90 degrees along the backscattering direction. So, we considered 50 measurement points on an arc on xz plane of radius 1.5 m from the center of the scatterer. It is observed that the reconstruction algorithm still works well with such a restriction. For $\beta = 8 \times 10^{-4}$ and $\text{SNR} = 60$ dB, the relative error in the reconstructed value of β is 0.55% as compared to 0.35% obtained previously using the data on the full circle. For $\beta = 8 \times 10^{-4}$ and $\text{SNR} = 40$ dB, the corresponding values are 3.4% and 2.5%. For $\beta = 8 \times 10^{-4}$ and $\text{SNR} = 20$ dB, the errors become 108.1% using the data along backscattered direction as opposed to 27.3% with the data on the full circle.

Now we are going to examine the effect when is measured only the amplitude of the electromagnetic fields using sensors. For this case, is changed the cost functions involved so that only differences in the magnitudes of each component of the fields are considered. The measurement points used for the reconstruction are the same as those in the previous step involving only backscattered fields. In this case, it is impossible to distinguish between the clockwise and anticlockwise rotations; therefore, we have to consider only the absolute value of the reconstructed. The results are shown in Figure 6.3. The accuracy is not comparable with obtained using amplitude and phase information. For $\beta = 8 \times 10^{-4}$ and $\text{SNR} = 40$ dB, the error in the reconstructed speed is 64.1%, as contrary to 3.4% obtained using both amplitude and phase data. However, with less noisy data the accuracy is acceptable as in the case with $\beta = 8 \times 10^{-4}$ and with $\text{SNR} = 60$ dB, where we get an error in the reconstructed speed of 1.28%. Similar comparisons can be made for the case of $\beta = 8 \times 10^{-3}$ and $\beta = 8 \times 10^{-5}$ shown in the figures and the results are good when the speed is not very small, and the SNR is good enough.

A good solution for the rotating speeds is still obtained when the measurement is restricted to the backscattering direction. The results are degraded when only amplitude data are

available, but the errors are still small provided that the noise does not overwhelm the effects of motion.

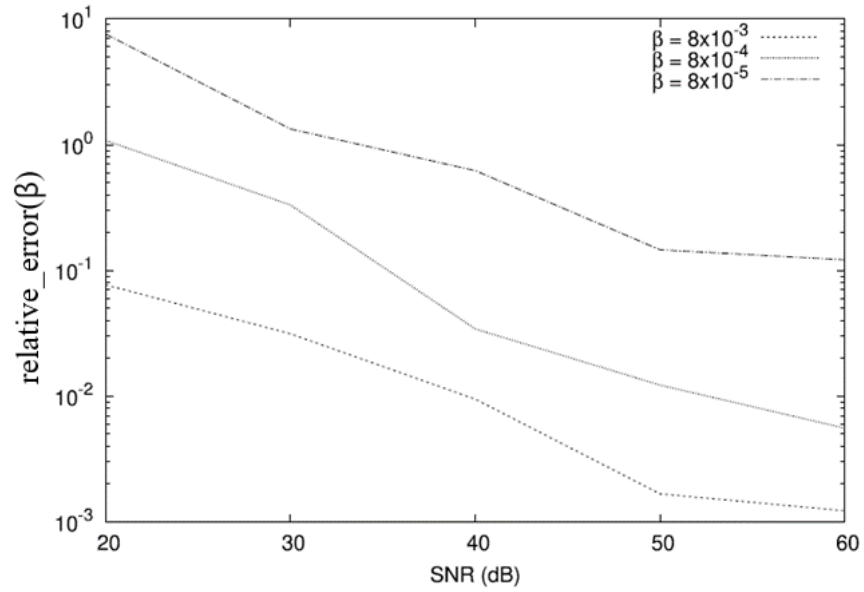


Figure 6.4 The relative error of recovery value of β vs SNR levels in dB for the rotating sphere using backscattered data.

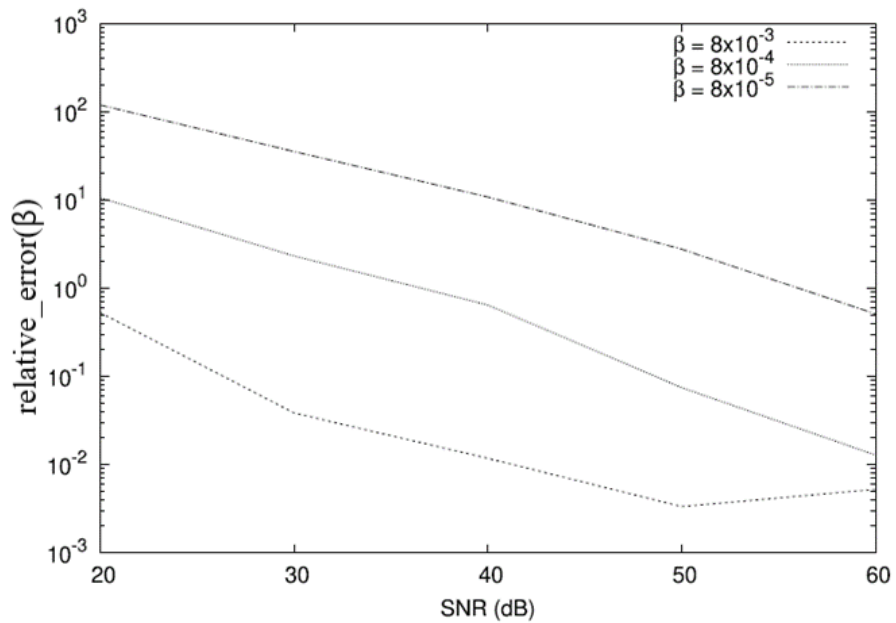


Figure 6.5 The relative error of recovery value of β vs SNR levels in dB for the rotating sphere using only amplitude data.

6.3.3 Reconstruction of velocity of rotation

So far, we concentrated on the performance of the reconstruction algorithm using the total field data in the near-field region.

Now, we are going to analyze the performance of the algorithm with the scattered electromagnetic field in the far-field region. For this, we consider the measurement arc on xz plane in the backscattered direction of radius 1.5×10^3 m from the center of the scatterer. The results are plotted in Figure 6.4. The algorithm performs well for $\beta = 8 \times 10^{-3}$ and the error for SNR values greater than or equal to 30 dB is less than 2.2% and is 13.1% for SNR of 20 dB. For $\beta = 8 \times 10^{-4}$, the error in the reconstructed value of β is 3.7% for SNR of 60 dB and is around 9% for 40 dB and rises to 23% for 30 dB of SNR. Finally, for $\beta = 8 \times 10^{-5}$, the reconstruction algorithm performs very weakly for the considered values of SNR. The error for 60 dB SNR in the data is 4% while for 50 dB the error is 19.3% and rises to unacceptable levels as the noise increases.

It is now examined the effect of error in the knowledge of the axis of rotation of the scatterer. For this, we may generate the measurement data using the forward model on an arc whose plane is rotated by an angle from the xz plane while still using the old set of points for the reconstruction algorithm. For $\beta = 8 \times 10^{-3}$, the algorithm is able to find the value of the rotating speed with an error of less than 1.6% for SNR values greater than or equal to 30 dB. The error for $\beta = 8 \times 10^{-4}$ is 1.3% for SNR=60 dB, 15.1% for SNR=40 dB and 22.8% for SNR=30 dB. Finally, for $\beta = 8 \times 10^{-5}$, the results for the considered values of SNR are unreliable with a 36% error even for SNR=60 dB, which rises to a 102% error for SNR=40 dB.

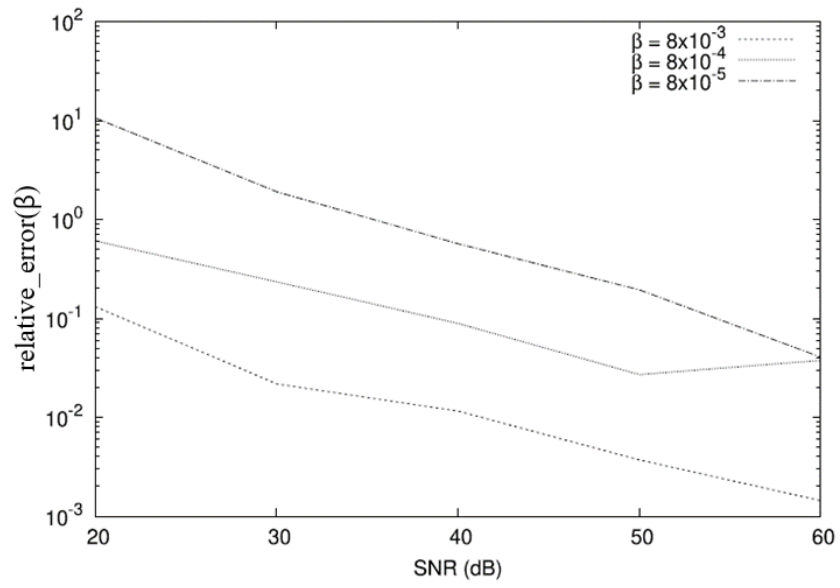


Figure 6.6. The relative error of recovery value of β vs SNR levels in dB for the rotating sphere using far-field data.

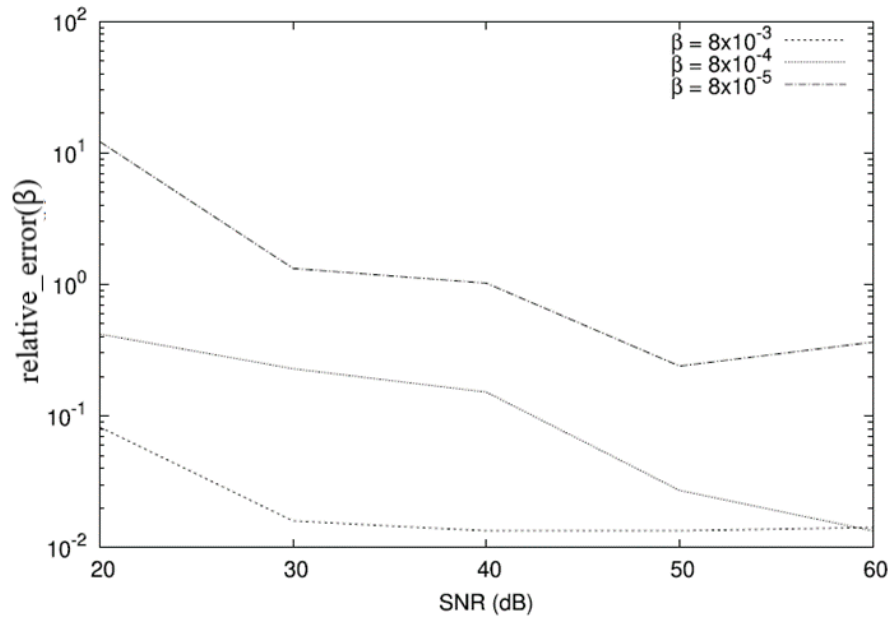


Figure 6.7. The relative error of recovery value of β vs SNR levels in dB for the rotating sphere using far-field data for inclination angle 10 degree.

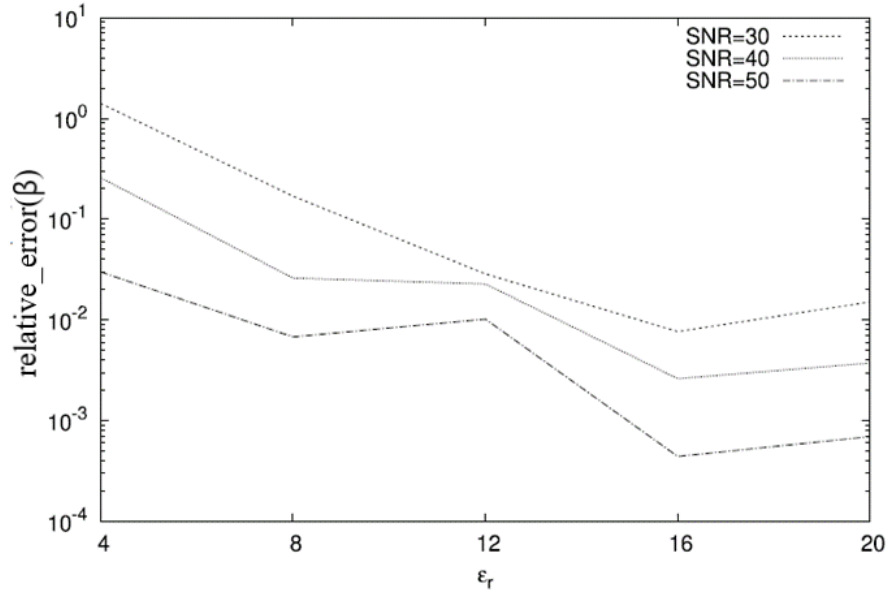


Figure 6.8. The relative error of recovery value of β vs ϵ_r for the rotating sphere with $\beta = 8 \times 10^{-4}$ and different SNR values.

6.3.4. Effect of dielectric media

Now we examined the effect of the relative dielectric parameter, ϵ_r on the accuracy of the reconstructed speed. The result for a rotating speed $\beta = 8 \times 10^{-4}$ is presented in Figure 6.8. The measurements are considered at $M = 200$ points on a circle of radius $R_m = 1.5$ m. The permittivity values considered are $\epsilon_r \in \{4, 8, 12, 16, 20\}$, and the results are shown for three noise levels, $\text{SNR} \in \{30; 40; 50\}$ [dB]. The reconstruction becomes more complicated if the scattering is weak; therefore, we can generally expect a larger error for smaller values of ϵ_r . This trend can be confirmed from the obtained results. For instance, with $\text{SNR} = 40$ dB, the relative error is 25.7%. For $\epsilon_r = 4$ while it reduces to 0.37% for $\epsilon_r = 20$. Similarly, the error goes from 140% to 1.5% for $\text{SNR} = 30$ dB and from 2.99% to 0.069% for $\text{SNR} = 50$ dB, as ϵ_r increases from 4 to 20.

6.3.5 Recovery of rotating speed for torus model

The algorithm is applied for axisymmetric rotating homogeneous torus for which analytic solutions are unavailable, a numerical forward solver must be exploited instead. The direct solution for the fields is obtained using COMSOL Multiphysics [8], [14][133]. The axis of symmetry of the torus is the z-axis about which the torus rotates with an angular velocity

ω_s . The torus' major and the minor radius are defined by $(R_{\text{tor}}, r_{\text{tor}})$, they are taken the values of 0.75m and 0.25m, respectively. The geometry of the test case is shown in Figure 6.9. It is expressed the normalized rotation speed with the equation $\beta = \omega_s(R_{\text{tor}} + r_{\text{tor}})/C_0$. The scattering medium at rest is characterized by $\epsilon_r = 8$. It is illuminated by a plane wave incident propagated along the x-axis polarized along z-axis with $f_s = 150$ MHz. The domain is fixed with ratio $R_d = 4$ m and the measurement data are taken at $M = 200$ points distributed on a circle in xz plane of radius $R_m = 1.5$ m. The algebraic solver used is GMRES with 10^{-4} of tolerance and a geometric multigrid preconditioner. The reconstruction algorithm searches the optimal value of β in the range $[0, 10^{-2}]$. The parameters of the DE optimizer as the same as before. The measured data is corrupted with similar noise levels used before. The results are shown in figure for values of $\beta \in \{8 \times 10^{-5}, 8 \times 10^{-4}, 8 \times 10^{-3}\}$. When $\beta = 8 \times 10^{-3}$ the relative error is less than 1.6% with SNR are greater than or equal to 30 dB. For $\beta = 8 \times 10^{-4}$, the relative error is 2.14% for SNR=50 dB, 13.9% for SNR=40 dB and 21.6% for SNR=30dB. For $\beta = 8 \times 10^{-5}$, the relative error is higher 16.7% for SNR=60 dB, 29.9% for SNR=50 dB and more than 100% in other cases. The additional noise in the numerical solver is a reason for test the performance of the reconstruction algorithm compared to the case with semi analytic forward solver. For small values of rotating speed, is necessary non only to perform an accurate measurement for the fields, but also reduce numerical errors for obtain reliable results.

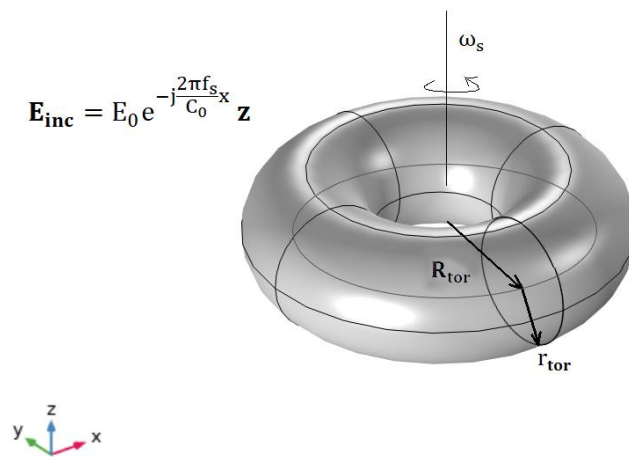


Figure 6.9. The geometry of the case involves a homogeneous toroidal scatterer with major radius R_{tor} and minor radius r_{tor} rotating the z-axis with angular velocity ω_s . The electric field incident is an electromagnetic plane wave with frequency f_s propagated along the x-axis and polarized along the z-axis.

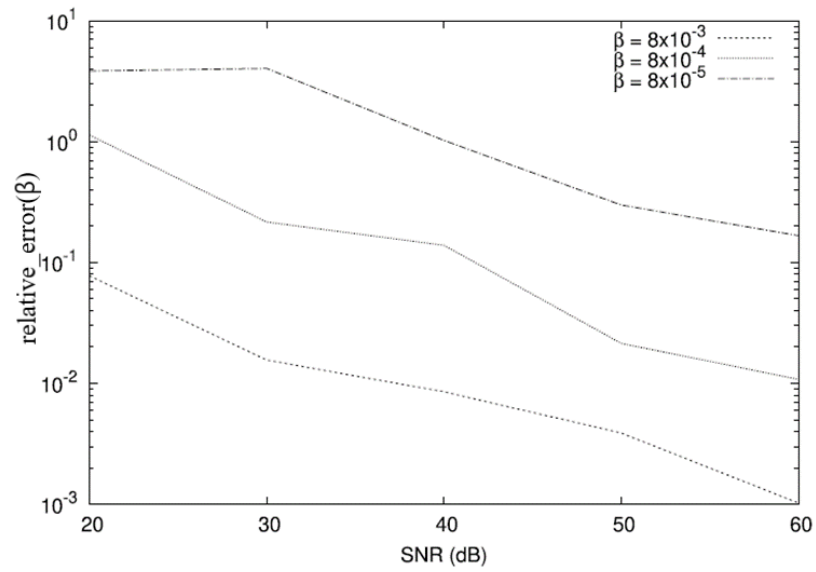


Figure 6.10. The relative error of recovery value of β vs SNR levels in dB for the rotating torus.

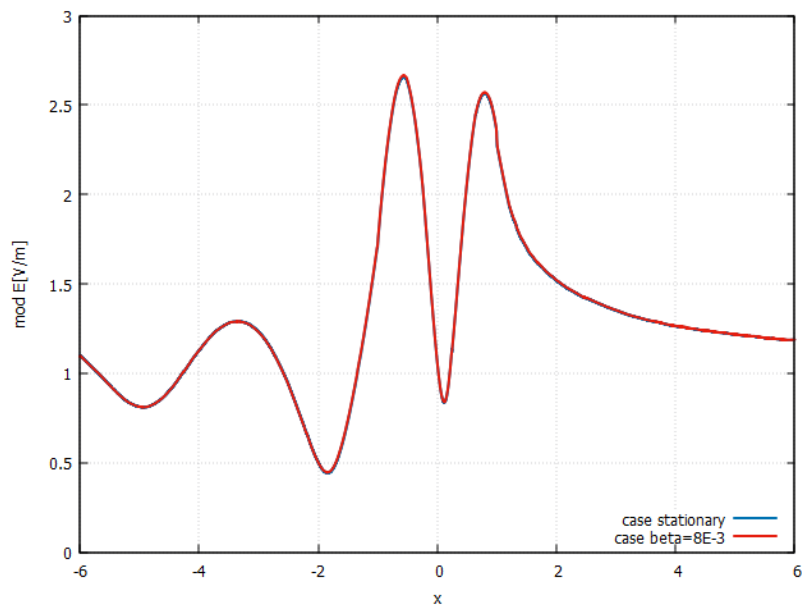


Figure 6.11. module of electric field along the x-axis passing through the gravity center of the sphere. The models are compared when it is rotating with $\beta = 8 \times 10^{-3}$ and it is stationary.

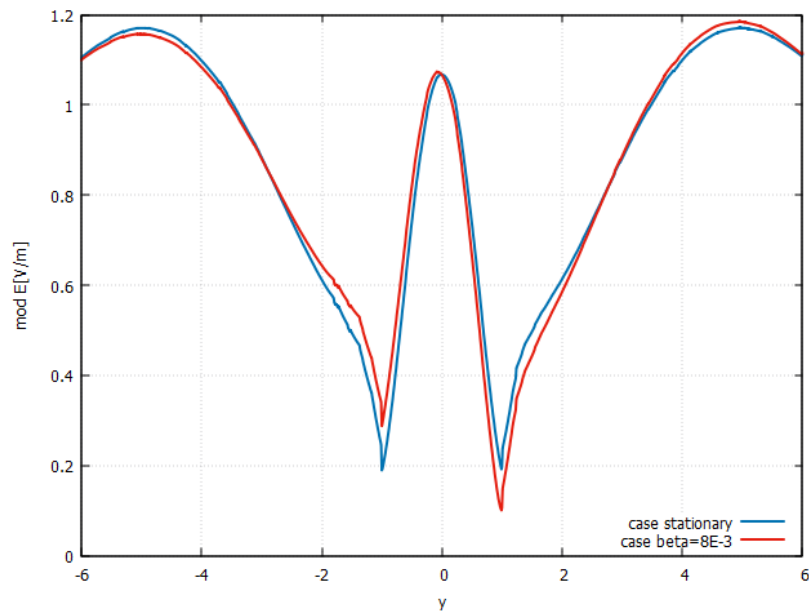


Figure 6.12. module of electric field along the y-axis passing through the gravity center of the sphere. The models are compared when it is rotating with $\beta = 8 \times 10^{-3}$ and it is stationary.

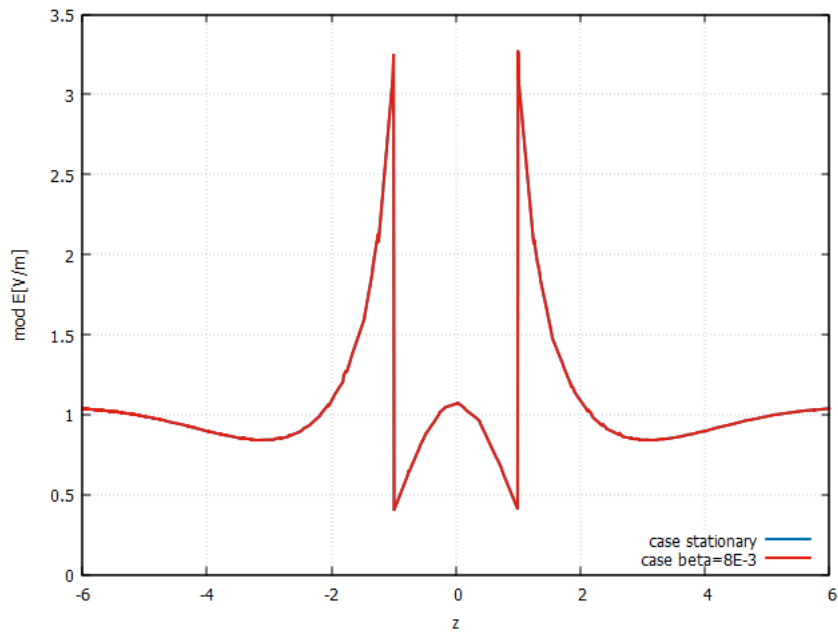


Figure 6.13. module of electric field along the z-axis passing through the gravity center of the sphere. The models are compared when it is rotating with $\beta = 8 \times 10^{-3}$ and it is stationary.

Figures 6.11 to 6.13 is compared the module of electric field in x, y and z axis passing through the gravity center of the sphere when is stationary and is rotating with $\beta = 8 \times 10^{-3}$.

Figures 6.14 and 6.15 is compared the component z of electric field for sphere and torus models when it is stationary and it is rotating with $\beta = 8 \times 10^{-3}$ and 2×10^{-3} , respectively.

The different planes xy , yz and xz passing through center of gravity of sphere and torus models are plotted.

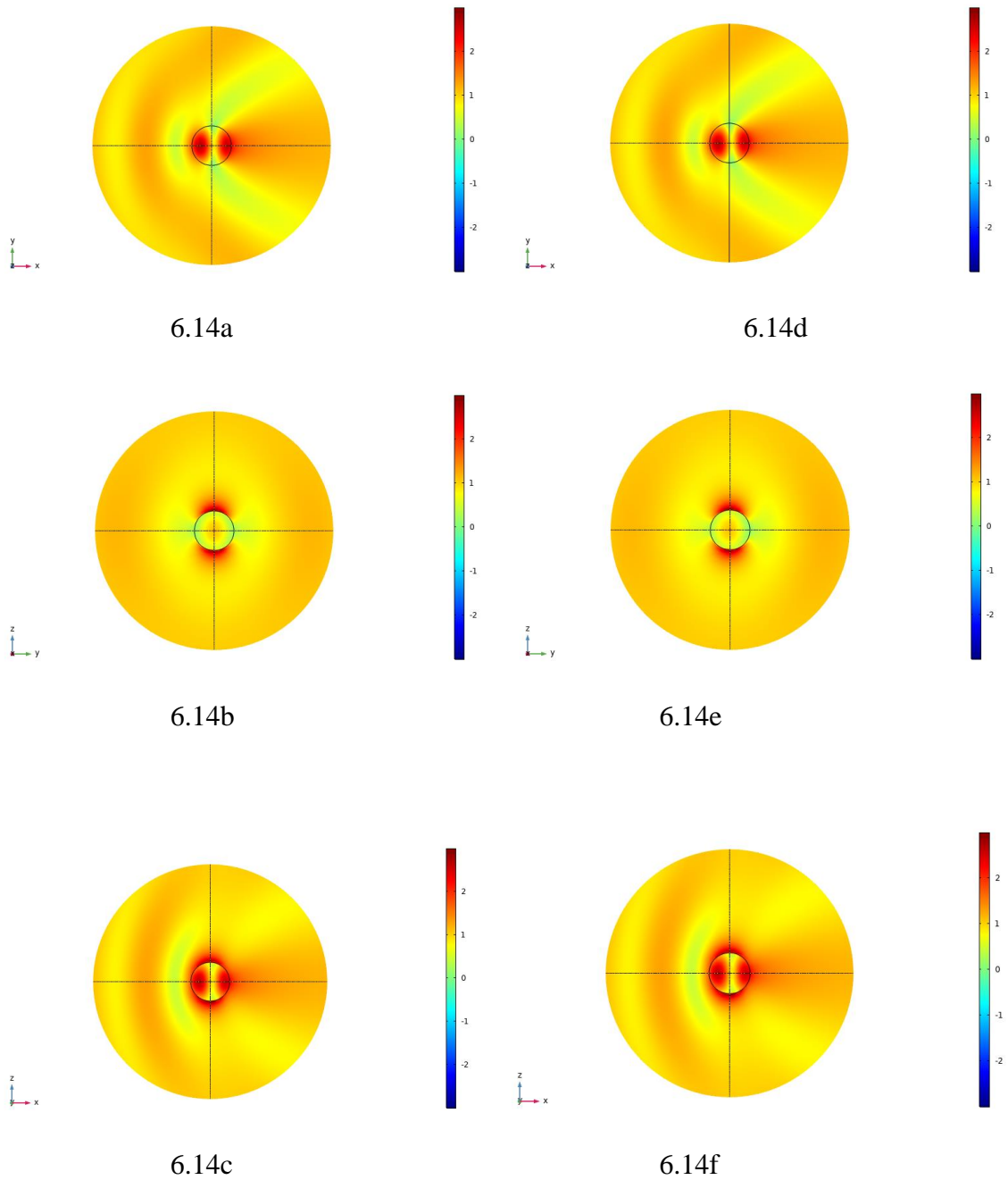


Figure 6.14. Component z of electric field when the sphere is stationary and is rotating along z -axis with $\beta = 8 \times 10^{-3}$ for different planes xy , yz and xz .

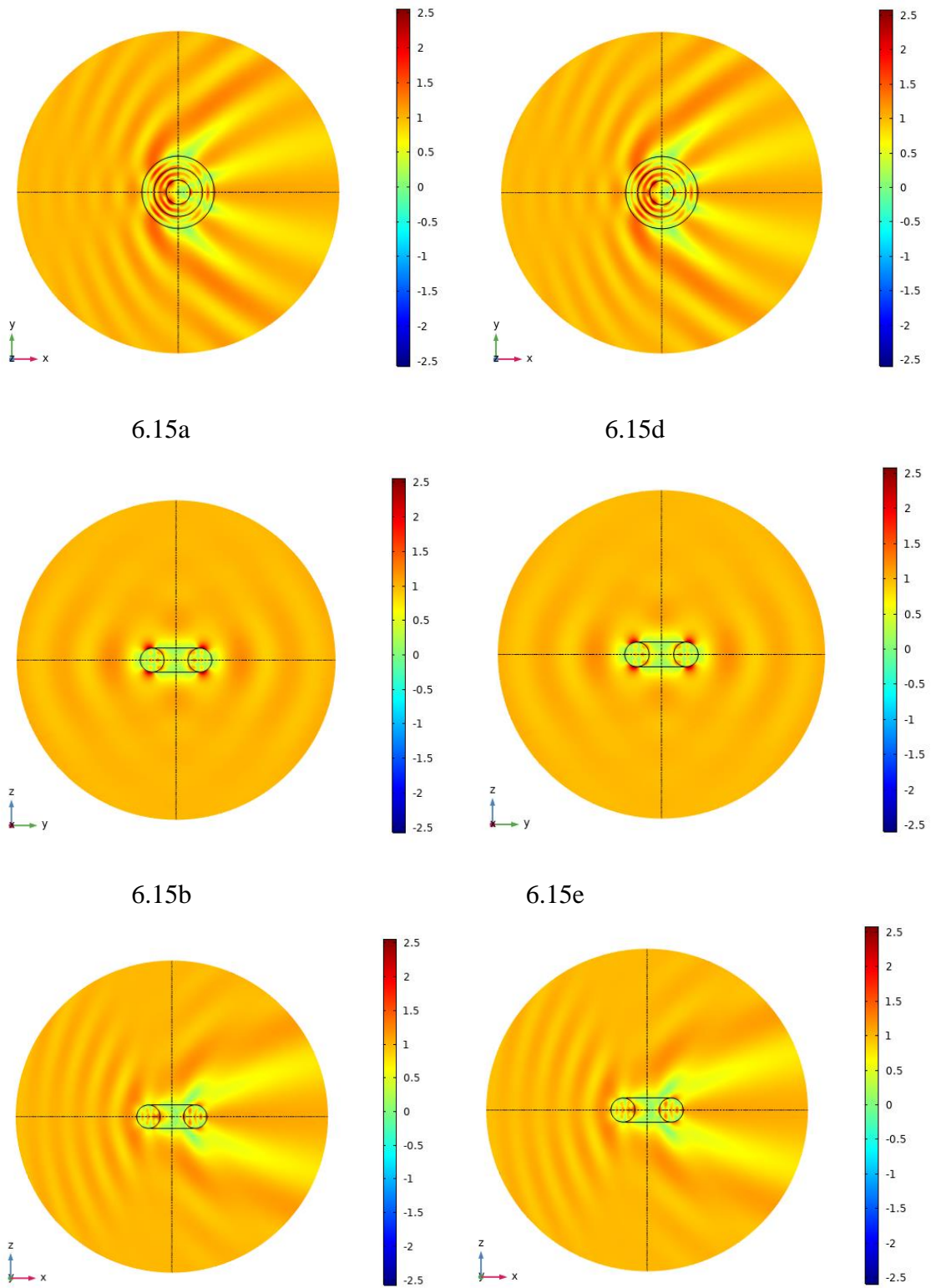


Figure 6.15. Component z of electric field when torus is stationary and is rotating with $\beta = 2 \times 10^{-3}$ along z -axis, for different planes xy , yz and xz .

The electromagnetic inverse problem involving rotating axisymmetric objects is studied in this work. It investigates the reconstruction of the rotating speeds of axisymmetric objects from the scattered field data. A two-step algorithm was proposed for the inversion when the speeds are lower. In the first step, a forward solver is employed assuming zero rotating speed, and the geometric and dielectric data are reconstructed by minimizing the cost function indicated in equation (56). The values from the first step are used to determine the rotating speed in the second step minimizing the cost function indicated in equation (58). By defining a test case involving a rotating homogeneous sphere, the two-step procedure is compared with the straightforward inversion procedure, which solves all the unknowns together.

We can conclude that the two-step procedure is much faster and more accurate if the rotating speeds assume values of practical interest. The performance of the algorithm was tested with different types of noisy data for near-field data, far-field data and amplitude-only data. The results show that for relatively low-speed values, the two-step procedure can reliably recover the velocity of rotation, provided that the noise does not overwhelm the effects of the rotation on the field. The algorithm was applied to a rotating torus to demonstrate the generality of the results. This work studied the test cases with homogeneous velocity profiles to give the first results on the efficiency and accuracy of the two-step procedure. However, the proposed algorithm is general and can be applied to more complex velocity profiles.

CONCLUSIONS

This thesis has highlighted the importance of the absorption of the electromagnetic field in the visible or NIR bands for Low Level Laser Therapies. An approach is proposed for a better understanding the interaction mechanism between laser irradiation and biological organelles. This therapy is a non-invasive therapeutic procedure that stimulates cellular metabolism with laser irradiation in band 600 to 1100 nm at low power; the most important organelle in this mechanism is the mitochondrion. The method consists of proposing the first approximation of the electromagnetic field in the system considering a multilayer structure, which is solved analytically to obtain the first results. The algorithm calculates the electromagnetic field in every medium without mitochondria. The next step is to propose three-dimensional models, referring to a well-defined experimental setup, allowing the evaluation of the electromagnetic field inside the mitochondria. The set of models examined is sufficiently rich to take account of the different possible configurations (isolated, layered, or clustered) that mitochondria can assume in practice. Several values of their dimensions and constitutive parameters were considered for the differences among mitochondria and the uncertainty of the quantities of interest in electromagnetic models. Finally, different wavelengths and polarizations were used. The effects of the changes in all parameters of our models are presented. Most of the discussion that followed was focused on the average properties of the electromagnetic field inside mitochondria. These results give quantitative estimates of the dosage that the mitochondria are exposed to during PBM experiments and hence can help clear up the inconsistencies in the literature related to those experiments. The results can be important for understanding the mechanism of interaction when the PBM present positive results. However, any such consideration with the multiprotein complexes present inside mitochondria is out of the scope of the present study.

Nevertheless, since it provides reliable calculations of the electromagnetic field inside the mitochondria, we consider it a first step to deepening our understanding of the interaction mechanism of interest. The system is implemented in an environment controlled with laser in continuous wave, incubation chamber made of glass, solution PBS and sample of mitochondria. The system “in vitro” is irradiated for different cases of power and irradiation time. It is necessary to continue researching this topic, to better understand the

mechanism of interaction between light and the biological organelles responsible for cell regeneration.

The energy and power density are computed for an average value of mitochondria for different models, internal structure, polarizations, configurations, and wavelength. It is necessary to carry out more research of this topic, because there exists a lack of information about geometric dimension, internal structure, optical parameters and number of organelles which are present when the PBM experiments in vitro present positive response. Also, it is necessary to know number and position of chromophores presents inside of mitochondria. The first results confirmed that oxygen production is present when a specific power irradiation is applied, triggering the enhanced of oxygen through the ATP production found in photomolecules called chromophores. The results are being processed and will be presented in a future scientific contribution.

It is important to continue with this research topic from an engineering point of view, to delve deep into the electromagnetic models of mitochondria and to carry out more controlled in vitro experiments with mitochondrial samples to increase the knowledge between the dependence of the energy provided by the laser and the energy produced when it increases the production of oxygen by the mitochondria.

In my research activity I focus on computational electromagnetics problems, working mainly on the LLLT topic, these computational electromagnetic techniques are exploited to in other research topic involving moving objects, in this context, electromagnetic model is implemented to study the effect of rotating objects irradiated with an electromagnetic plane wave. The electromagnetic inverse problem involving rotating axisymmetric objects was studied for the first time. We investigated the reconstruction of the rotating speeds of axisymmetric objects from the scattered field data. A two-step algorithm was proposed for the inversion when the speeds are known to be a computational efficiency and manageable size. In the first step, a forward solver is employed, assuming zero rotating speed, and the geometric and dielectric data are reconstructed by minimizing the cost function. The values from the first step are used to determine the rotating speed in the second step. By defining a test case involving a rotating homogeneous sphere, the two-step procedure is compared with the straightforward inversion procedure, which solves all the unknowns together. It was established that the two-step procedure is much faster and more accurate if the rotating

speeds assume low values. The algorithm's performance was tested with different types of noisy data: near-field data, far-field data, and amplitude-only data were used as inputs to the two-step procedure to obtain the rotating speeds. The results show that for relatively small speed values, the two-step procedure can reliably recover the rotation velocity, provided that the noise does not overwhelm the effects of the rotation on the field. The algorithm was applied to a rotating torus to demonstrate the generality of the results. This work studied only the test cases with homogeneous velocity profiles to give the first results on the efficiency and accuracy of the two-step procedure. However, the proposed algorithm is general and can be applied to more complex velocity profiles with symmetry.

References

- [1] W. Posten, D. A. Wrone, J. S. Dover, K. A. Arndt, S. Silapunt, and M. Alam, “Low-Level Laser Therapy for Wound Healing: Mechanism and Efficacy,” *Dermatologic Surgery*, vol. 31, no. 3, pp. 334–340, Mar. 2006, doi: 10.1111/j.1524-4725.2005.31086.
- [2] H. Chung, T. Dai, S. K. Sharma, Y.-Y. Huang, J. D. Carroll, and M. R. Hamblin, “The Nuts and Bolts of Low-level Laser (Light) Therapy,” *Ann Biomed Eng*, vol. 40, no. 2, pp. 516–533, Feb. 2012, doi: 10.1007/s10439-011-0454-7.
- [3] R. Zein, W. Selting, and M. R. Hamblin, “Review of light parameters and photobiomodulation efficacy: dive into complexity,” *J. Biomed. Opt.*, vol. 23, no. 12, p. 1, Dec. 2018, doi: 10.1117/1.JBO.23.12.120901.
- [4] E. Mester, B. Szende, and P. Gärtner, “The effect of laser beams on the growth of hair in mice,” *Radiobiol Radiother (Berl)*, vol. 9, no. 5, pp. 621–626, 1968.
- [5] P. E. McGuff, R. A. Deterling, and L. S. Gottlieb, “Tumoricidal Effect of Laser Energy on Experimental and Human Malignant Tumors,” *N Engl J Med*, vol. 273, no. 9, pp. 490–492, Aug. 1965, doi: 10.1056/NEJM196508262730906.
- [6] I. B. Kovls, E. Mester, and P. Görög, “Stimulation of wound healing with laser beam in the rat,” *Experientia*, vol. 30, no. 11, pp. 1275–1276, Nov. 1974, doi: 10.1007/BF01945182.
- [7] D. P. Kuffler, “Photobiomodulation in promoting wound healing: a review,” *Regenerative Medicine*, vol. 11, no. 1, pp. 107–122, Jan. 2016, doi: 10.2217/rme.15.82.
- [8] P. V. Peplow, T.-Y. Chung, and G. D. Baxter, “Laser Photobiomodulation of Wound Healing: A Review of Experimental Studies in Mouse and Rat Animal Models,” *Photomedicine and Laser Surgery*, vol. 28, no. 3, pp. 291–325, Jun. 2010, doi: 10.1089/pho.2008.2446.
- [9] Y.-Y. Huang, S. K. Sharma, J. Carroll, and M. R. Hamblin, “Biphasic Dose Response in Low Level Light Therapy – an Update,” *Dose-Response*, vol. 9, no. 4, p. dose-response.1, Oct. 2011, doi: 10.2203/dose-response.11-009.Hamblin.

- [10] S.-R. Tsai and M. R. Hamblin, “Biological effects and medical applications of infrared radiation,” *Journal of Photochemistry and Photobiology B: Biology*, vol. 170, pp. 197–207, May 2017, doi: 10.1016/j.jphotobiol.2017.04.014.
- [11] M. R. Hamblin, “Mechanisms and Mitochondrial Redox Signaling in Photobiomodulation,” *Photochem Photobiol*, vol. 94, no. 2, pp. 199–212, Mar. 2018, doi: 10.1111/php.12864.
- [12] A. Amaroli, S. Ferrando, and S. Benedicenti, “Photobiomodulation Affects Key Cellular Pathways of all Life-Forms: Considerations on Old and New Laser Light Targets and the Calcium Issue,” *Photochem Photobiol*, vol. 95, no. 1, pp. 455–459, Jan. 2019, doi: 10.1111/php.13032.
- [13] A. Amaroli, S. Ravera, F. Baldini, S. Benedicenti, I. Panfoli, and L. Vergani, “Photobiomodulation with 808-nm diode laser light promotes wound healing of human endothelial cells through increased reactive oxygen species production stimulating mitochondrial oxidative phosphorylation,” *Lasers Med Sci*, vol. 34, no. 3, pp. 495–504, Apr. 2019, doi: 10.1007/s10103-018-2623-5.
- [14] S. Ravera *et al.*, “Mitochondrial Bioenergetic, Photobiomodulation and Trigeminal Branches Nerve Damage, What’s the Connection? A Review,” *IJMS*, vol. 22, no. 9, p. 4347, Apr. 2021, doi: 10.3390/ijms22094347.
- [15] S. A. Mohamad, M. R. Milward, M. A. Hadis, S. A. Kuehne, and P. R. Cooper, “Photobiomodulation of mineralisation in mesenchymal stem cells,” *Photochem Photobiol Sci*, vol. 20, no. 5, pp. 699–714, May 2021, doi: 10.1007/s43630-021-00047-5.
- [16] A. P. Sommer, “Mitochondrial cytochrome c oxidase is not the primary acceptor for near infrared light—it is mitochondrial bound water: the principles of low-level light therapy,” *Ann. Transl. Med*, vol. 7, no. S1, pp. S13–S13, Mar. 2019, doi: 10.21037/atm.2019.01.43.
- [17] A. P. Sommer, “Revisiting the Photon/Cell Interaction Mechanism in Low-Level Light Therapy,” *Photobiomodulation, Photomedicine, and Laser Surgery*, vol. 37, no. 6, pp. 336–341, Jun. 2019, doi: 10.1089/photob.2018.4606.
- [18] P. L. V. Lima *et al.*, “Photobiomodulation enhancement of cell proliferation at 660 nm does not require cytochrome c oxidase,” *Journal of Photochemistry and*

- Photobiology B: Biology*, vol. 194, pp. 71–75, May 2019, doi: 10.1016/j.jphotobiol.2019.03.015.
- [19] D. W. Barrett and F. Gonzalez-Lima, “Transcranial infrared laser stimulation produces beneficial cognitive and emotional effects in humans,” *Neuroscience*, vol. 230, pp. 13–23, Jan. 2013, doi: 10.1016/j.neuroscience.2012.11.016.
- [20] F. Salehpour and S. H. Rasta, “The potential of transcranial photobiomodulation therapy for treatment of major depressive disorder,” *Reviews in the Neurosciences*, vol. 28, no. 4, pp. 441–453, May 2017, doi: 10.1515/revneuro-2016-0087.
- [21] F. Salehpour, N. Ahmadian, S. H. Rasta, M. Farhoudi, P. Karimi, and S. Sadigh-Eteghad, “Transcranial low-level laser therapy improves brain mitochondrial function and cognitive impairment in D-galactose-induced aging mice,” *Neurobiology of Aging*, vol. 58, pp. 140–150, Oct. 2017, doi: 10.1016/j.neurobiolaging.2017.06.025.
- [22] M. A. Naeser, A. Saltmarche, M. H. Kregel, M. R. Hamblin, and J. A. Knight, “Improved Cognitive Function After Transcranial, Light-Emitting Diode Treatments in Chronic, Traumatic Brain Injury: Two Case Reports,” *Photomedicine and Laser Surgery*, vol. 29, no. 5, pp. 351–358, May 2011, doi: 10.1089/pho.2010.2814.
- [23] A. S. Fonseca *et al.*, “Effect of laser therapy on DNA damage: LASER THERAPY AND DNA DAMAGE,” *Lasers Surg. Med.*, vol. 42, no. 6, pp. 481–488, Aug. 2010, doi: 10.1002/lsm.20921.
- [24] D. Hawkins, “Low Level Laser Therapy (LLLT) as an Effective Therapeutic Modality for Delayed Wound Healing,” *Annals of the New York Academy of Sciences*, vol. 1056, no. 1, pp. 486–493, Nov. 2005, doi: 10.1196/annals.1352.040.
- [25] S. R. Ferreira de Meneses, D. J. Hunter, E. Young Docko, and A. Pasqual Marques, “Effect of low-level laser therapy (904 nm) and static stretching in patients with knee osteoarthritis: a protocol of randomised controlled trial,” *BMC Musculoskelet Disord*, vol. 16, no. 1, p. 252, Dec. 2015, doi: 10.1186/s12891-015-0709-9.
- [26] M. Bayat *et al.*, “An evaluation of the effect of pulsed wave low-level laser therapy on the biomechanical properties of the vertebral body in two experimental osteoporosis rat models,” *Lasers Med Sci*, vol. 31, no. 2, pp. 305–314, Feb. 2016, doi: 10.1007/s10103-015-1842-2.

- [27] F. Ahrari, A. S. Madani, Z. S. Ghafouri, and J. Tunér, “The efficacy of low-level laser therapy for the treatment of myogenous temporomandibular joint disorder,” *Lasers Med Sci*, vol. 29, no. 2, pp. 551–557, Mar. 2014, doi: 10.1007/s10103-012-1253-6.
- [28] S. Bouvet-Gerbetaz, E. Merigo, J.-P. Rocca, G. F. Carle, and N. Rochet, “Effects of low-level laser therapy on proliferation and differentiation of murine bone marrow cells into osteoblasts and osteoclasts: EFFECTS OF LLLT ON MURINE BONE MARROW CELLS,” *Lasers Surg. Med.*, vol. 41, no. 4, pp. 291–297, Apr. 2009, doi: 10.1002/lsm.20759.
- [29] K. P. S. Fernandes *et al.*, “Photobiomodulation with 660-nm and 780-nm laser on activated J774 macrophage-like cells: Effect on M1 inflammatory markers,” *Journal of Photochemistry and Photobiology B: Biology*, vol. 153, pp. 344–351, Dec. 2015, doi: 10.1016/j.jphotobiol.2015.10.015.
- [30] Y.-Y. Huang, K. Nagata, C. E. Tedford, T. McCarthy, and M. R. Hamblin, “Low-level laser therapy (LLLT) reduces oxidative stress in primary cortical neurons in vitro,” *J. Biophoton.*, p. n/a-n/a, Dec. 2012, doi: 10.1002/jbio.201200157.
- [31] Y.-Y. Huang, K. Nagata, C. E. Tedford, and M. R. Hamblin, “Low-level laser therapy (810 nm) protects primary cortical neurons against excitotoxicity in vitro: LLLT protects cortical neurons against excitotoxicity,” *J. Biophoton.*, vol. 7, no. 8, pp. 656–664, Aug. 2014, doi: 10.1002/jbio.201300125.
- [32] S. K. Sharma *et al.*, “Dose response effects of 810 nm laser light on mouse primary cortical neurons,” *Lasers Surg. Med.*, vol. 43, no. 8, pp. 851–859, Sep. 2011, doi: 10.1002/lsm.21100.
- [33] U. Oron, S. Ilic, L. De Taboada, and J. Streeter, “Ga-As (808 nm) Laser Irradiation Enhances ATP Production in Human Neuronal Cells in Culture,” *Photomedicine and Laser Surgery*, vol. 25, no. 3, pp. 180–182, Jun. 2007, doi: 10.1089/pho.2007.2064.
- [34] N. H. C. Souza, R. A. M. Ferrari, D. F. T. Silva, F. D. Nunes, S. K. Bussadori, and K. P. S. Fernandes, “Effect of low-level laser therapy on the modulation of the mitochondrial activity of macrophages,” *Braz. J. Phys. Ther.*, vol. 18, no. 4, pp. 308–314, Aug. 2014, doi: 10.1590/bjpt-rbf.2014.0046.
- [35] C.-H. Chen *et al.*, “Effects of Low-Level Laser Therapy on M1-Related Cytokine Expression in Monocytes via Histone Modification,” *Mediators of Inflammation*, vol. 2014, pp. 1–13, 2014, doi: 10.1155/2014/625048.

- [36] C. Ferraresi *et al.*, “Low-level Laser (Light) Therapy Increases Mitochondrial Membrane Potential and ATP Synthesis in C2C12 Myotubes with a Peak Response at 3-6 h,” *Photochem Photobiol*, vol. 91, no. 2, pp. 411–416, Mar. 2015, doi: 10.1111/php.12397.
- [37] A. Amaroli *et al.*, “Photobiomodulation by Infrared Diode Laser: Effects on Intracellular Calcium Concentration and Nitric Oxide Production of *Paramecium*,” *Photochem Photobiol*, vol. 92, no. 6, pp. 854–862, Nov. 2016, doi: 10.1111/php.12644.
- [38] Y. Wang, Y.-Y. Huang, Y. Wang, P. Lyu, and M. R. Hamblin, “Photobiomodulation (blue and green light) encourages osteoblastic-differentiation of human adipose-derived stem cells: role of intracellular calcium and light-gated ion channels,” *Sci Rep*, vol. 6, no. 1, p. 33719, Dec. 2016, doi: 10.1038/srep33719.
- [39] S. Song, Y. Zhang, C.-C. Fong, C.-H. Tsang, Z. Yang, and M. Yang, “cDNA Microarray Analysis of Gene Expression Profiles in Human Fibroblast Cells Irradiated with Red Light,” *Journal of Investigative Dermatology*, vol. 120, no. 5, pp. 849–857, May 2003, doi: 10.1046/j.1523-1747.2003.12133.x.
- [40] Y. Xu, Y. Lin, S. Gao, and J. Shen, “Study on mechanism of release oxygen by photo-excited hemoglobin in low-level laser therapy,” *Lasers Med Sci*, vol. 33, no. 1, pp. 135–139, Jan. 2018, doi: 10.1007/s10103-017-2363-y.
- [41] M. Tschon, S. Incerti-Parenti, S. Cepollaro, L. Checchi, and M. Fini, “Photobiomodulation with low-level diode laser promotes osteoblast migration in an *in vitro* micro wound model,” *J. Biomed. Opt*, vol. 20, no. 7, p. 078002, Jul. 2015, doi: 10.1117/1.JBO.20.7.078002.
- [42] M. Migliario, P. Pittarella, M. Fanuli, M. Rizzi, and F. Renò, “Laser-induced osteoblast proliferation is mediated by ROS production,” *Lasers Med Sci*, vol. 29, no. 4, pp. 1463–1467, Jul. 2014, doi: 10.1007/s10103-014-1556-x.
- [43] S.-J. Pyo *et al.*, “Low-level laser therapy induces the expressions of BMP-2, osteocalcin, and TGF- β 1 in hypoxic-cultured human osteoblasts,” *Lasers Med Sci*, vol. 28, no. 2, pp. 543–550, Feb. 2013, doi: 10.1007/s10103-012-1109-0.
- [44] M. D. Skopin and S. C. Molitor, “Effects of near-infrared laser exposure in a cellular model of wound healing,” *Photodermatology, Photoimmunology & Photomedicine*, vol. 25, no. 2, pp. 75–80, Apr. 2009, doi: 10.1111/j.1600-0781.2009.00406.x.

- [45] S. B. Bozkurt, E. E. Hakki, S. A. Kayis, N. Dundar, and S. S. Hakki, “Biostimulation with diode laser positively regulates cementoblast functions, in vitro,” *Lasers Med Sci*, vol. 32, no. 4, pp. 911–919, May 2017, doi: 10.1007/s10103-017-2192-z.
- [46] Y. Wang, Y.-Y. Huang, Y. Wang, P. Lyu, and M. R. Hamblin, “Red (660 nm) or near-infrared (810 nm) photobiomodulation stimulates, while blue (415 nm), green (540 nm) light inhibits proliferation in human adipose-derived stem cells,” *Sci Rep*, vol. 7, no. 1, p. 7781, Dec. 2017, doi: 10.1038/s41598-017-07525-w.
- [47] Y. Wang, Y.-Y. Huang, Y. Wang, P. Lyu, and M. R. Hamblin, “Photobiomodulation of human adipose-derived stem cells using 810 nm and 980 nm lasers operates via different mechanisms of action,” *Biochimica et Biophysica Acta (BBA) - General Subjects*, vol. 1861, no. 2, pp. 441–449, Feb. 2017, doi: 10.1016/j.bbagen.2016.10.008.
- [48] A. C. Alves *et al.*, “Effect of low-level laser therapy on the expression of inflammatory mediators and on neutrophils and macrophages in acute joint inflammation,” *Arthritis Res Ther*, vol. 15, no. 5, p. R116, 2013, doi: 10.1186/ar4296.
- [49] U. Oron *et al.*, “Attenuation of infarct size in rats and dogs after myocardial infarction by low-energy laser irradiation,” *Lasers Surg. Med.*, vol. 28, no. 3, pp. 204–211, 2001, doi: 10.1002/lsm.1039.
- [50] U. Oron *et al.*, “Low-Energy Laser Irradiation Reduces Formation of Scar Tissue After Myocardial Infarction in Rats and Dogs,” *Circulation*, vol. 103, no. 2, pp. 296–301, Jan. 2001, doi: 10.1161/01.CIR.103.2.296.
- [51] A. P. Castano *et al.*, “Low-level laser therapy for zymosan-induced arthritis in rats: Importance of illumination time,” *Lasers Surg. Med.*, vol. 39, no. 6, pp. 543–550, Jul. 2007, doi: 10.1002/lsm.20516.
- [52] Q. Wu *et al.*, “Low-Level Laser Therapy for Closed-Head Traumatic Brain Injury in Mice: Effect of Different Wavelengths: TRANSCRANIAL LLLT FOR TBI IN MICE,” *Lasers Surg. Med.*, vol. 44, no. 3, pp. 218–226, Mar. 2012, doi: 10.1002/lsm.22003.
- [53] N. J. Blanco, W. T. Maddox, and F. Gonzalez-Lima, “Improving executive function using transcranial infrared laser stimulation,” *J Neuropsychol*, vol. 11, no. 1, pp. 14–25, Mar. 2017, doi: 10.1111/jnp.12074.

- [54] S. G. Disner, C. G. Beevers, and F. Gonzalez-Lima, “Transcranial Laser Stimulation as Neuroenhancement for Attention Bias Modification in Adults with Elevated Depression Symptoms,” *Brain Stimulation*, vol. 9, no. 5, pp. 780–787, Sep. 2016, doi: 10.1016/j.brs.2016.05.009.
- [55] T. Ando *et al.*, “Comparison of Therapeutic Effects between Pulsed and Continuous Wave 810-nm Wavelength Laser Irradiation for Traumatic Brain Injury in Mice,” *PLoS ONE*, vol. 6, no. 10, p. e26212, Oct. 2011, doi: 10.1371/journal.pone.0026212.
- [56] Q. Zhang, C. Zhou, M. R. Hamblin, and M. X. Wu, “Low-Level Laser Therapy Effectively Prevents Secondary Brain Injury Induced by Immediate Early Responsive Gene X-1 Deficiency,” *J Cereb Blood Flow Metab*, vol. 34, no. 8, pp. 1391–1401, Aug. 2014, doi: 10.1038/jcbfm.2014.95.
- [57] B. M. Baroni, E. C. P. Leal Junior, J. M. Geremia, F. Diefenthaler, and M. A. Vaz, “Effect of Light-Emitting Diodes Therapy (LEDT) on Knee Extensor Muscle Fatigue,” *Photomedicine and Laser Surgery*, vol. 28, no. 5, pp. 653–658, Oct. 2010, doi: 10.1089/pho.2009.2688.
- [58] H. Zhang, J. Hou, Y. Shen, W. Wang, Y. Wei, and S. Hu, “Low level laser irradiation precondition to create friendly milieu of infarcted myocardium and enhance early survival of transplanted bone marrow cells,” *Journal of Cellular and Molecular Medicine*, vol. 14, no. 7, pp. 1975–1987, Jul. 2010, doi: 10.1111/j.1582-4934.2009.00886.x.
- [59] R. Á. B. Lopes-Martins *et al.*, “Effect of low-level laser (Ga-Al-As 655 nm) on skeletal muscle fatigue induced by electrical stimulation in rats,” *Journal of Applied Physiology*, vol. 101, no. 1, pp. 283–288, Jul. 2006, doi: 10.1152/jappphysiol.01318.2005.
- [60] T. M. Vera Mendez, A. L. Barbosa Pinheiro, M. Tadeu Tavares Pacheco, L. M. Pedreira Ramalho, and P. M. do Nascimento, “Assessment of the influence of the dose and wavelength of LLLT on the repair of cutaneous wounds,” presented at the Biomedical Optics 2003, San Jose, CA, Jun. 2003, p. 137. doi: 10.1117/12.476431.
- [61] R. J. Lanzafame *et al.*, “Reciprocity of exposure time and irradiance on energy density during photoradiation on wound healing in a murine pressure ulcer model,” *Lasers Surg. Med.*, vol. 39, no. 6, pp. 534–542, Jul. 2007, doi: 10.1002/lsm.20519.

- [62] V. Prabhu, S. B. S. Rao, N. B. Rao, K. B. Aithal, P. Kumar, and K. K. Mahato, “Development and Evaluation of Fiber Optic Probe-based Helium-Neon Low-level Laser Therapy System for Tissue Regeneration-An In Vivo Experimental Study,” *Photochemistry and Photobiology*, vol. 86, no. 6, pp. 1364–1372, Nov. 2010, doi: 10.1111/j.1751-1097.2010.00791.x.
- [63] P. Gál *et al.*, “Effect of equal daily doses achieved by different power densities of low-level laser therapy at 635 nm on open skin wound healing in normal and corticosteroid-treated rats,” *Lasers Med Sci*, vol. 24, no. 4, pp. 539–547, Jul. 2009, doi: 10.1007/s10103-008-0604-9.
- [64] F. A. H. Al-Watban and G. D. Delgado, “Burn Healing with a Diode Laser: 670 nm at Different Doses as Compared to a Placebo Group,” *Photomedicine and Laser Surgery*, vol. 23, no. 3, pp. 245–250, Jun. 2005, doi: 10.1089/pho.2005.23.245.
- [65] D. Barbosa, R. A. de Souza, M. Xavier, F. F. da Silva, E. Â. L. Arisawa, and A. G. J. B. Villaverde, “Effects of low-level laser therapy (LLLT) on bone repair in rats: optical densitometry analysis,” *Lasers Med Sci*, vol. 28, no. 2, pp. 651–656, Feb. 2013, doi: 10.1007/s10103-012-1125-0.
- [66] C. Wang, S. Tsai, M. Yu, Y. Lin, C. Chen, and P. Chang, “Light-Emitting Diode Irradiation Promotes Donor Site Wound Healing of the Free Gingival Graft,” *Journal of Periodontology*, vol. 86, no. 5, pp. 674–681, May 2015, doi: 10.1902/jop.2015.140580.
- [67] I.-S. Park, A. Mondal, P.-S. Chung, and J. C. Ahn, “Vascular regeneration effect of adipose-derived stem cells with light-emitting diode phototherapy in ischemic tissue,” *Lasers Med Sci*, vol. 30, no. 2, pp. 533–541, Feb. 2015, doi: 10.1007/s10103-014-1699-9.
- [68] F. Salehpour, N. Ahmadian, S. H. Rasta, M. Farhoudi, P. Karimi, and S. Sadigh-Eteghad, “Transcranial low-level laser therapy improves brain mitochondrial function and cognitive impairment in D-galactose-induced aging mice,” *Neurobiology of Aging*, vol. 58, pp. 140–150, Oct. 2017, doi: 10.1016/j.neurobiolaging.2017.06.025.
- [69] R. Kilík *et al.*, “Effect of Equal Daily Doses Achieved by Different Power Densities of Low-Level Laser Therapy at 635 nm on Open Skin Wound Healing in Normal and Diabetic Rats,” *BioMed Research International*, vol. 2014, pp. 1–9, 2014, doi: 10.1155/2014/269253.

- [70] F. Di Marco *et al.*, “Combining Neuroprotectants in a Model of Retinal Degeneration: No Additive Benefit,” *PLoS ONE*, vol. 9, no. 6, p. e100389, Jun. 2014, doi: 10.1371/journal.pone.0100389.
- [71] J. G. Barreto and C. G. Salgado, “Clinic-epidemiological evaluation of ulcers in patients with leprosy sequelae and the effect of low level laser therapy on wound healing: a randomized clinical trial,” *BMC Infect Dis*, vol. 10, no. 1, p. 237, Dec. 2010, doi: 10.1186/1471-2334-10-237.
- [72] S. S. Goodman, R. A. Bentler, A. Dittberner, and I. B. Mertes, “The Effect of Low-Level Laser Therapy on Hearing,” *ISRN Otolaryngology*, vol. 2013, pp. 1–9, Apr. 2013, doi: 10.1155/2013/916370.
- [73] J. E. Choi, M. Y. Lee, P.-S. Chung, and J. Y. Jung, “A preliminary study on the efficacy and safety of low level light therapy in the management of cochlear tinnitus: A single blind randomized clinical trial,” *The International Tinnitus Journal*, vol. 23, no. 1, 2019, doi: 10.5935/0946-5448.20190010.
- [74] C. Pasquale, A. Utyuzh, M. V. Mikhailova, E. Colombo, and A. Amaroli, “Recovery from Idiopathic Facial Paralysis (Bell’s Palsy) Using Photobiomodulation in Patients Non-Responsive to Standard Treatment: A Case Series Study,” *Photonics*, vol. 8, no. 8, p. 341, Aug. 2021, doi: 10.3390/photonics8080341.
- [75] Y. Shao, A. T. Maximov, I. G. Ourdev, U. Rozmus, and C. E. Capjack, “Spectral method simulations of light scattering by biological cells,” *IEEE J. Quantum Electron.*, vol. 37, no. 5, pp. 617–625, May 2001, doi: 10.1109/3.918573.
- [76] M. Gou, M.-L. Yang, and X.-Q. Sheng, “Fast computation of radiation pressure force exerted by multiple laser beams on red blood cell-like particles,” presented at the International Symposium on Optoelectronic Technology and Application 2016, Beijing, China, Oct. 2016, p. 1015309. doi: 10.1117/12.2244128.
- [77] P. Goktas, I. O. Sukharevsky, and A. Altintas, “Electromagnetic Scattering by Several 2-D Single Biological Cell Models,” *United States National Committee of URSI National Radio Science Meeting*, Jan. 2018.
- [78] A. Molalei, M. Saviz, and R. Faraji-Dana, “Detailed modeling and numerical analysis of photoreceptor cells exposed to electromagnetic fields,” *2011 19th Iranian Conference on Electrical Engineering*, Jul. 2011.

- [79] Lingyao Yu, Yunlong Sheng, and Arthur Chiou, “Three-dimensional light-scattering and deformation of individual biconcave human blood cells in optical tweezers,” *OPTICS EXPRESS*, vol. 21, no. 10, pp. 12174–12184, May 2013, doi: 10.1364/OE.21.012174.
- [80] A. Dunn, R. Richards-Kortum, “Three-dimensional computation of light scattering from cells,” *IEEE Journal of Selected Topics in Quantum Electronics*, vol. 2, no. 4, pp. 898–905, Dec. 1996, doi: 10.1109/2944.577313.
- [81] A. Karlsson, Jiangping He, J. Swartling, S. Andersson-Engels, “Numerical simulations of light scattering by red blood cells,” *IEEE Transactions on Biomedical Engineering*, vol. 52, no. 1, pp. 13–18, doi: 10.1109/TBME.2004.839634.
- [82] X. Lin, N. Wan, H. Zhu, and L. Weng, “Cell light scattering characteristic numerical simulation research based on FDTD algorithm,” presented at the International Conference on Innovative Optical Health Science, Shanghai Everbright International Hotel, China, Jan. 2017, p. 102450F. doi: 10.1117/12.2267489.
- [83] S. Tanev, V. V. Tuchin, and P. Paddon, “Light scattering effects of gold nanoparticles in cells: FDTD modeling,” *Laser Phys. Lett.*, vol. 3, no. 12, pp. 594–598, Dec. 2006, doi: 10.1002/lapl.200610052.
- [84] X. Lin, N. Wan, L. Weng, and Y. Zhou, “Light scattering from normal and cervical cancer cells,” *Appl. Opt.*, vol. 56, no. 12, p. 3608, Apr. 2017, doi: 10.1364/AO.56.003608.
- [85] S. Tanev, “Simulation technique enhances cellular nanobioimaging,” *SPIE Newsroom*, 2008, doi: 10.1117/2.1200808.1224.
- [86] T. I. Karu, “Mitochondrial Signaling in Mammalian Cells Activated by Red and Near-IR Radiation,” *Photochemistry and Photobiology*, vol. 84, no. 5, pp. 1091–1099, Sep. 2008, doi: 10.1111/j.1751-1097.2008.00394.x.
- [87] S. Passarella and T. Karu, “Absorption of monochromatic and narrow band radiation in the visible and near IR by both mitochondrial and non-mitochondrial photoacceptors results in photobiomodulation,” *Journal of Photochemistry and Photobiology B: Biology*, vol. 140, pp. 344–358, Nov. 2014, doi: 10.1016/j.jphotobiol.2014.07.021.

- [88] T. Karu, “Primary and secondary mechanisms of action of visible to near-IR radiation on cells,” *Journal of Photochemistry and Photobiology B: Biology*, vol. 49, no. 1, pp. 1–17, Mar. 1999, doi: 10.1016/S1011-1344(98)00219-X.
- [89] M. R. Hamblin, M. V. P. de Sousa, and T. Agrawal, *Handbook of low-level laser therapy*. Singapore: Pan Stanford publishing, 2017.
- [90] M. L. Denton *et al.*, “Photon absorption in the mitochondria: Potential immediate and early events associated with photobiomodulation,” in *Mechanisms of Photobiomodulation Therapy XIV*, San Francisco, United States, Mar. 2019, p. 5. doi: 10.1117/12.2508518.
- [91] L. F. de Freitas and M. R. Hamblin, “Proposed Mechanisms of Photobiomodulation or Low-Level Light Therapy,” *IEEE J. Select. Topics Quantum Electron.*, vol. 22, no. 3, pp. 348–364, May 2016, doi: 10.1109/JSTQE.2016.2561201.
- [92] A. R. D. Stebbing, “Hormesis — The stimulation of growth by low levels of inhibitors,” *Science of The Total Environment*, vol. 22, no. 3, pp. 213–234, Feb. 1982, doi: 10.1016/0048-9697(82)90066-3.
- [93] M. A. Hadis *et al.*, “The dark art of light measurement: accurate radiometry for low-level light therapy,” *Lasers Med Sci*, vol. 31, no. 4, pp. 789–809, May 2016, doi: 10.1007/s10103-016-1914-y.
- [94] V. Heiskanen and M. R. Hamblin, “Photobiomodulation: lasers vs. light emitting diodes?,” *Photochem. Photobiol. Sci.*, vol. 17, no. 8, pp. 1003–1017, 2018, doi: 10.1039/C8PP00176F.
- [95] N. Tripodi *et al.*, “Good, better, best? The effects of polarization on photobiomodulation therapy,” *Journal of Biophotonics*, vol. 13, no. 5, May 2020, doi: 10.1002/jbio.201960230.
- [96] A. Amaroli *et al.*, “Electromagnetic Dosimetry for Isolated Mitochondria Exposed to Near-Infrared Continuous-Wave Illumination in Photobiomodulation Experiments,” *Bioelectromagnetics*, vol. 42, no. 5, pp. 384–397, Jul. 2021, doi: 10.1002/bem.22342.
- [97] R. Thar and M. Köhl, “Propagation of electromagnetic radiation in mitochondria?,” *Journal of Theoretical Biology*, vol. 230, no. 2, pp. 261–270, Sep. 2004, doi: 10.1016/j.jtbi.2004.05.021.
- [98] R. F. Harrington, *Time-harmonic electromagnetic fields*. New York: IEEE Press : Wiley-Interscience, 2001.

- [99] J. A. Stratton, *Electromagnetic theory*. Hoboken, New Jersey: John Wiley & Sons, Inc, 2007.
- [100] S. L. Jacques, “Corrigendum: Optical properties of biological tissues: a review,” *Phys. Med. Biol.*, vol. 58, no. 14, pp. 5007–5008, Jul. 2013, doi: 10.1088/0031-9155/58/14/5007.
- [101] I. E. Scheffler, *Mitochondria*, 2nd ed. Hoboken, N.J: Wiley-Liss, 2008.
- [102] B. Beauvoit, T. Kitai, and B. Chance, “Contribution of the mitochondrial compartment to the optical properties of the rat liver: a theoretical and practical approach,” *Biophysical Journal*, vol. 67, no. 6, pp. 2501–2510, Dec. 1994, doi: 10.1016/S0006-3495(94)80740-4.
- [103] H. Ullah *et al.*, “Femtosecond light distribution at skin and liver of rats: analysis for use in optical diagnostics,” *Laser Phys. Lett.*, vol. 7, no. 12, pp. 889–898, Dec. 2010, doi: 10.1002/lapl.201010079.
- [104] K. F. Palmer and D. Williams, “Optical properties of water in the near infrared*,” *J. Opt. Soc. Am.*, vol. 64, no. 8, p. 1107, Aug. 1974, doi: 10.1364/JOSA.64.001107.
- [105] C. C. Wang, J. Y. Tan, and L. H. Liu, “Wavelength and concentration-dependent optical constants of NaCl, KCl, MgCl₂, CaCl₂, and Na₂SO₄ multi-component mixed-salt solutions,” *Appl. Opt.*, vol. 56, no. 27, p. 7662, Sep. 2017, doi: 10.1364/AO.56.007662.
- [106] H. Bach and N. Neuroth, Eds., *The Properties of Optical Glass*. Berlin, Heidelberg: Springer Berlin Heidelberg, 1998. doi: 10.1007/978-3-642-57769-7.
- [107] P. Monk, *Finite element methods for Maxwell’s equations*. Oxford: New York: Clarendon Press ; Oxford University Press, 2003.
- [108] D. J. Hoppe and Y. Rahmat-Samii, *Impedance boundary conditions in electromagnetics*. Washington, DC: Taylor & Francis, 1995.
- [109] G. Conciauro, *Introduzione alle onde elettromagnetiche*. Milano, etc.: McGraw-Hill Libri Italia srl, 1993.
- [110] P. Fernandes and M. Raffetto, “Existence, uniqueness and finite element approximation of the solution of time-harmonic electromagnetic boundary value problems involving metamaterials,” *COMPEL*, vol. 24, no. 4, pp. 1450–1469, Dec. 2005, doi: 10.1108/03321640510615724.

- [111] P. Fernandes and M. Raffetto, “WELL-POSEDNESS AND FINITE ELEMENT APPROXIMABILITY OF TIME-HARMONIC ELECTROMAGNETIC BOUNDARY VALUE PROBLEMS INVOLVING BIANISOTROPIC MATERIALS AND METAMATERIALS,” *Math. Models Methods Appl. Sci.*, vol. 19, no. 12, pp. 2299–2335, Dec. 2009, doi: 10.1142/S0218202509004121.
- [112] P. Kalarickel Ramakrishnan and M. Raffetto, “Three-Dimensional Time-Harmonic Electromagnetic Scattering Problems from Bianisotropic Materials and Metamaterials: Reference Solutions Provided by Converging Finite Element Approximations,” *Electronics*, vol. 9, no. 7, p. 1065, Jun. 2020, doi: 10.3390/electronics9071065.
- [113] T. Itoh, Ed., *Numerical techniques for microwave and millimeter-wave passive structures*. New York: Wiley, 1989.
- [114] S. J. Orfanidis, *Electromagnetic Waves and Antennas*. 2016. [Online]. Available: www.ece.rutgers.edu/~orfanidi/ewa
- [115] S. E. Siegmund *et al.*, “Three-Dimensional Analysis of Mitochondrial Crista Ultrastructure in a Patient with Leigh Syndrome by In Situ Cryoelectron Tomography,” *iScience*, vol. 6, pp. 83–91, Aug. 2018, doi: 10.1016/j.isci.2018.07.014.
- [116] T. G. Frey, C. W. Renken, and G. A. Perkins, “Insight into mitochondrial structure and function from electron tomography,” *Biochimica et Biophysica Acta (BBA) - Bioenergetics*, vol. 1555, no. 1–3, pp. 196–203, Sep. 2002, doi: 10.1016/S0005-2728(02)00278-5.
- [117] G. Perkins, C. Renken, M. E. Martone, S. J. Young, M. Ellisman, and T. Frey, “Electron Tomography of Neuronal Mitochondria: Three-Dimensional Structure and Organization of Cristae and Membrane Contacts,” *Journal of Structural Biology*, vol. 119, no. 3, pp. 260–272, Aug. 1997, doi: 10.1006/jsbi.1997.3885.
- [118] C. A. Mannella, W. J. Lederer, and M. S. Jafri, “The connection between inner membrane topology and mitochondrial function,” *Journal of Molecular and Cellular Cardiology*, vol. 62, pp. 51–57, Sep. 2013, doi: 10.1016/j.yjmcc.2013.05.001.
- [119] G. C. Garcia *et al.*, “Mitochondrial morphology provides a mechanism for energy buffering at synapses,” *Sci Rep*, vol. 9, no. 1, p. 18306, Dec. 2019, doi: 10.1038/s41598-019-54159-1.

- [120] R. Thar and M. Kühl, “Propagation of electromagnetic radiation in mitochondria?,” *Journal of Theoretical Biology*, vol. 230, no. 2, pp. 261–270, Sep. 2004, doi: 10.1016/j.jtbi.2004.05.021.
- [121] A. Einstein, “Zur Elektrodynamik bewegter Körper,” *Ann. Phys.*, vol. 322, no. 10, pp. 891–921, 1905, doi: 10.1002/andp.19053221004.
- [122] J. van Bladel, *Electromagnetic fields*, 2nd ed. Hoboken, N.J: IEEE/Wiley-Interscience, 2007.
- [123] D. K. Cheng and Jin-Au Kong, “Covariant descriptions of bianisotropic media,” *Proc. IEEE*, vol. 56, no. 3, pp. 248–251, 1968, doi: 10.1109/PROC.1968.6268.
- [124] J. A. Kong, *Theory of electromagnetic waves*. New York: Wiley, 1975.
- [125] A. Sommerfeld, *Electrodynamics: lectures on theoretical physics vol. III*. New York: Academic Press, 1952.
- [126] J. Van Bladel, *Electromagnetic fields*, 2. ed. Piscataway, NJ: IEEE Press, 2007.
- [127] D. De Zutter, “Scattering by a rotating dielectric sphere,” *IEEE Trans. Antennas Propagat.*, vol. 28, no. 5, pp. 643–651, Sep. 1980, doi: 10.1109/TAP.1980.1142392.
- [128] P. Kalarickel Ramakrishnan and M. Raffetto, “Well Posedness and Finite Element Approximability of Three-Dimensional Time-Harmonic Electromagnetic Problems Involving Rotating Axisymmetric Objects,” *Symmetry*, vol. 12, no. 2, p. 218, Feb. 2020, doi: 10.3390/sym12020218.
- [129] M. Pastorino, M. Raffetto, and A. Randazzo, “Electromagnetic Inverse Scattering of Axially Moving Cylindrical Targets,” *IEEE Trans. Geosci. Remote Sensing*, vol. 53, no. 3, pp. 1452–1462, Mar. 2015, doi: 10.1109/TGRS.2014.2342933.
- [130] M. Brignone, G. L. Gragnani, M. Pastorino, M. Raffetto, and A. Randazzo, “Noise Limitations on the Recovery of Average Values of Velocity Profiles in Pipelines by Simple Imaging Systems,” *IEEE Geosci. Remote Sensing Lett.*, vol. 13, no. 9, pp. 1340–1344, Sep. 2016, doi: 10.1109/LGRS.2016.2584703.
- [131] R. Storn and K. Price, “*Differential Evolution – A Simple and Efficient Heuristic for global Optimization over Continuous Spaces*”, vol. 11, no. 4, pp. 341–359, 1997, doi: 10.1023/A:1008202821328.
- [132] M. Pastorino, *Microwave imaging*. Hoboken, N.J: John Wiley, 2010.

- [133] P. K. Ramakrishnan, M. R. Clemente Vargas, and M. Raffetto, “Electromagnetic Inverse Scattering of Rotating Axisymmetric Objects,” *IEEE Access*, vol. 9, pp. 168185–168192, 2021, doi: 10.1109/ACCESS.2021.3136356.
- [134] L. Baratto *et al.*, “Ultra-low-level laser therapy,” *Lasers Med Sci*, vol. 26, no. 1, pp. 103–112, Jan. 2011, doi: 10.1007/s10103-010-0837-2.
- [135] A. P. Sommer, A. L. B. Pinheiro, A. R. Mester, R.-P. Franke, and H. T. Whelan, “Biostimulatory Windows in Low-Intensity Laser Activation: Lasers, Scanners, and NASA’s Light-Emitting Diode Array System,” *Journal of Clinical Laser Medicine & Surgery*, vol. 19, no. 1, pp. 29–33, Feb. 2001, doi: 10.1089/104454701750066910.
- [136] Y.-Y. Huang, A. C.-H. Chen, J. D. Carroll, and M. R. Hamblin, “Biphasic Dose Response in Low Level Light Therapy,” *Dose-Response*, vol. 7, no. 4, p. dose-response.0, Oct. 2009, doi: 10.2203/dose-response.09-027.Hamblin.